REPORT DOCUMENTATION PAGE

Form Approved
OMB No. 0704-0188

1. AGENCY USE ONLY (Leave blank)	2. REPORT DATE 11/27/95	3. REPORT TYPE AND DATES COVERED Final Technical 9/1/92–8/31/95

4. TITLE AND SUBTITLE

(U)   Reaction Zone Models for Vortex Simulation of Turbulent Combustion

5. FUNDING NUMBERS

PE – 61102F
PR – 2308
SA – BS
G – F49620-92-J-0445

6. AUTHOR(S)

Ahmed F. Ghoniem

7. PERFORMING ORGANIZATION NAME(S) AND ADDRESS(ES)

Massachusetts Institute of Technology
77 Massachusetts Avenue
Cambridge, MA   02139

8. PERFORMING ORGANIZATION REPORT NUMBER

AFOSR-TR-
96-0032

9. SPONSORING/MONITORING AGENCY NAME(S) AND ADDRESS(ES)

AFOSR/NA
110 Duncan Avenue, Suite B115
Bolling AFB   DC   20332-0001
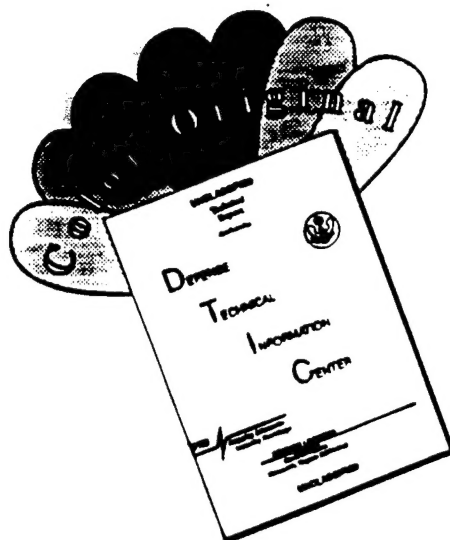
10. SPONSORING/MONITORING AGENCY REPORT NUMBER

19960201 109

11. SUPPLEMENTARY NOTES

12a. DISTRIBUTION/AVAILABILITY STATEMENT

Approved for public release; distribution is
unlimited

12b. DISTRIBUTION

13. ABSTRACT (Maximum 200 words)

The objectives of this work were to develop, implement and validate a reaction zone model for vorticity based turbulent combustion simulation at high Reynolds and Damkohler numbers. Direct Simulation results using the transport element method were used to examine the structure of the reaction zone and to develop a reasonable set of approximations that could be used to simplify the governing equations. The resulting model, adopting a singular expansion philosophy of the flow equations; the elemental flame model consists of (1) a conserved scalar approximation of the outer non-reacting flow to determine the location of the reaction surface; (2) an unsteady, uniformly strained flame structure model for the inner reacting flow imbedded within the reaction surface, to compute the local burning rate and flame structure profiles; and, (3) a set of kinematically based approximations used to monitor the generation, interaction and elimination of flame surface area as it spins around and reaches the tip of the spiral within large vortical structures. Comparisons between these "large structure simulations" and direct numerical simulation showed that the model could accurately capture the physics of reacting flows and predict flame surface evolution and rate of burning. Future work should be concerned with (a) extending this model by incorporating another approximation at areas of low strains, i.e., inside the large structure where the reaction zones resemble those of stratified reactors, and (b) extending the application of the developed model to three-dimensional flows.

14. SUBJECT TERMS

reaction zone model, vortex simulation, direct numerical
simulation

15. NUMBER OF PAGES
99

16. PRICE CODE

17. SECURITY CLASSIFICATION OF REPORT	18. SECURITY CLASSIFICATION OF THIS PAGE	19. SECURITY CLASSIFICATION OF ABSTRACT	20. LIMITATION OF ABSTRACT
Unclassified	Unclassified	Unclassified	UL

Standard Form 298 (890104 Draft)
Prescribed by ANSI Std. 239-18
239-01

DTIC QUALITY INSPECTED 1

DISCLAIMER NOTICE

THIS DOCUMENT IS BEST QUALITY AVAILABLE. THE COPY FURNISHED TO DTIC CONTAINED A SIGNIFICANT NUMBER OF COLOR PAGES WHICH DO NOT REPRODUCE LEGIBLY ON BLACK AND WHITE MICROFICHE.

FINAL TECHNICAL REPORT
ON

REACTION ZONE MODELS FOR VORTEX SIMULATION
OF TURBULENT COMBUSTION

(AFOSR Grant # F49620-92-J-0445DEF)

Principal Investigator: Ahmed F. Ghoniem

Department of Mechanical Engineering
Massachusetts Institute of Technology
Cambridge, MA 02139

ABSTRACT

The objectives of this work were to develop, implement and validate a reaction zone model for vorticity based turbulent combustion simulation at high Reynolds and Damkohler numbers. Direct Simulation results using the transport element method were used to examine the structure of the reaction zone and to develop a reasonable set of approximations that could be used to simplify the governing equations. The resulting model, adopting a singular expansion philosophy of the flow equations; the elemental flame model consists of (1) a conserved scalar approximation of the outer non-reacting flow to determine the location of the reaction surface; (2) an unsteady, uniformly strained flame structure model for the inner reacting flow imbedded within the reaction surface, to compute the local burning rate and flame structure profiles; and, (3) a set of kinematically based approximations used to monitor the generation, interaction and elimination of flame surface area as it spins around and reaches the tip of the spiral within large vortical structures. Comparisons between these "large structure simulations" and direct numerical simulation showed that the model could accurately capture the physics of reacting flows and predict flame surface evolution and rate of burning. Future work should be concerned with (a) extending this model by incorporating another approximation at areas of low strains, i.e., inside the large structure where the reaction zones resemble those of stratified reactors, and (b) extending the application of the developed model to three-dimensional flows.

I TECHNICAL REPORT

I.1. Objectives

The objectives of this project were to develop, implement and validate comprehensive reaction zone models, incorporating chemical kinetics and transport processes at a level of detail sufficient for the prediction of nonequilibrium combustion phenomena, which are fully compatible with Lagrangian vortex simulation approaches, i.e., kinematically based flow computations. The developed models would be comprehensive enough to enable the computation of in-flame formation of minor species as well as post flame destruction/formation of these species. The reaction zone models would be developed for the high Reynolds number, high Damkohler number conditions, i.e., in the so-called flamelet regime, or what we call the elemental flame regime, and would be compatible with large eddy simulation, or preferable large structure simulations of turbulent reacting flow. The models would be guided by the results of direct numerical simulation results obtained via detailed solutions of the governing equations utilizing the transport element method, and would be designed to converge to the direct simulation results as the numerical or modeling resolution was refined.

I.2. Overview

We have accomplished the above objectives by achieving substantial progress in three related projects summarized next.

(1) *Direct Numerical Simulation of Turbulent combustion at High Reynolds Number and Damkohler Number Using the Transport Element Method.*

In this project, we showed that our direct simulation method can be extended to accommodate finite rate reaction mechanisms by using the concept of product elements and by refining the diffusion-mixing-reaction algorithm (Appendices I and IV and Pubs. 3 and 4). Next we used the results of the direct simulations to; (a) show that at high Damkohler number, results of the infinite reaction rate model using Shvab-Zeldovich (conserved scalar) formulation agree well with those obtained using a finite reaction rate model in terms

2

of the flow dynamics, the mixing rates and the product formation rate, (b) gain valuable insight into the physics of turbulent reacting flows to guide the formulation of the reaction zone models, and (c) validate the results obtained using the reaction zone models which are described next.

(2) *Reaction Zone Models in Lagrangian Simulations Using the Concept of Elemental Flames at Infinite and Finite Reaction Rates.*

In this project, and recognizing that direct simulation using finite rate multispecies mechanisms is extremely expensive when detailed transport processes and chemical kinetics are included in the calculations, we embarked on an effort to use what we learned from the detailed simulation results to construct physically accurate reaction zone models which are compatible with the vortex simulation approach of solving the Navier-Stokes equation and are applicable at high Reynolds and Damkohler numbers. To this end:

(a) At the fast chemistry model, i.e. to model mixing without reaction, we formulated, implemented and validated a version of our transport element method which takes advantage of the observation that as soon as the mixing layer experiences folding to the point where the distance between neighboring elements is smaller than the diffusion thickness, the layers cannot be distinguished from one another and they should be merged. Moreover, as soon as the elements reach the tip of the rollup spiral inside the large eddies, they join what can be considered a well mixed zone, or a macro element (it is actually a radially stratified zone but with small gradients). While the strain and elongation of the transport elements increase their number as they move around the spiral centers, their number is limited by elimination at the spiral tip.

(b) At finite rate reactions, instead of using a transport element which simulates the mixing process locally, we developed a new concept: an elemental flame. This is a reacting element (molecule) which simulate combustion locally. Elemental flames are distributed along the spiraling interface to capture the reaction zone normal to the interface. Contrary to a transport element, whose field is obtained analytically as the

3

Green function of the differential equation governing convective-diffusive transport, the field of the elemental flame is obtained numerically by integrating a reduced set of the original convection-diffusion-reaction governing equations obtained by enforcing a constant value of the strain field throughout the flame structure (while these equations represent the first term in a series expansion in the strain, the effective strain used in the solution, to improve accuracy, is selected to be that at reaction-diffusion zone, as described in detail in Appendices II and III). For elemental flames, as for transport elements, they are born at the zones of maximum strain (outside the large eddies) while they die where the strain reaches zero (at the centers of the eddies).

(c) Consistent with the concept of elemental flames which produce macro combustion elements at the centers of the eddies, we modified the vortex simulation scheme to take advantage of the natural tendency of vorticity to accumulate inside the large eddies by replacing a collection of small vortices by a growing large element. This "large structure simulation" scheme has been shown to agree very well with the results of the detailed simulation but at a fraction of the cost.

(3) *Unsteady Uniformly Strained Flame Structure Model with Detailed Chemistry and Transport for Computing the Elemental Flame Structure.*

As mentioned before the elemental flame model of the reaction zone structure assumes that locally, a thin flat flame exists. Thus, one must start the computation by dividing the material interface, of flame into a large number of flat segments, and solve a large number of flame structure problems to reconstruct the reacting flow field. To do this economically, we simplified the set of equations governing the unsteady strained flame structure by assuming that the strain is uniform throughout the flame structure and thus transforming the governing equations into a simpler set of reaction- diffusion equations. By properly selecting the equivalent uniform strain corresponding to the given actual strain using a formula which we have derived for both diffusion and premixed flames, one can use this model, which is more robust numerically and faster computationally, to recover the

4

flame structure accurately. The model was also tested and validated using reduced chemical kinetics schemes.

In the rest of the report, more detail summarizing the effort leading to the formulation of the elemental flame reaction zone models are presented. The Appendices describe more extended versions of different parts of the projects.

I.3. Direct Simulations Approach and Results

Direct simulation of the vorticity dynamics, scalar mixing and combustion in high Reynolds number, high Damkohler number flows using the transport element method, a Lagrangian approach to the simulation of the Navier-Stokes, species and energy conservation equations, has several advantages, including the reduction of the computational effort by concentrating the computational elements at zones of high vorticity, the direct evaluation of the correct (non diffuse) material interface across which reaction occurs, and the natural temporal and spatial adaptivity. Results of a large number of simulations which we have conducted over the past few years have shown that:

(1) Mixing and combustion in a shear layer depends strongly on the inlet conditions since a small shift in the relative initial location of the shear (vorticity) layer with respect to the mixing (material interface) layer can lead to substantial changes in the striation and whorling of the reaction surface, as shown in figure 1. This leads to substantial changes in the amount of mixed fluid and rate of product formation in the layer, as shown in figure 2. The results indicate while one may be able to control the mixing rate by adjusting judiciously the boundary conditions, accurate predictions require ensemble averaging, even under ergodic conditions, and not temporal or spatial averaging (see Pubs. [7,9]).

(2) The impact of the boundary conditions on the mixing, and hence, reaction rates extend to the case when heat release is substantial. This is because when the reaction surface is located further away from the vorticity layer, the impact of heat release on the latter is much more moderate than in the case when the two layers are aligned. This issue

5

is discussed in detail in the paper in Appendix I where we investigated means by which the negative impact of heat release on the mixing rate can be mitigated by (a) adding a wake component to the initial shear layer profile (boundary layer tripping) or (b) displacing the two layers with respect to each other.

(3) Even at relatively low Reynolds numbers, the flame zone is much thinner than the large scale vorticity structure (characterized by ΔU and λ, the shear and initial instability wave length, respectively, and thinner than the small scale foldings inside these structures (described by the striation $\sigma = \Delta U/\varepsilon$ where ε is the prevailing strain).

The two-way cascade (formation of large scale due to rollup and pairing, and small scales due to stretching and spiraling) leads to the formation of vortex worms, while the flame surface continues to fold inside and around these structures.

(4) The flame structure within these folds is strongly affected by the competition between convection (stretch) and diffusion normal to the flame surface. Locally, the structure resembles that of a one-dimensional stretched flame, except when local flame surface curvature is much higher than the flame thickness, a condition encountered rarely. In cases when the initial material interface does not coincide with the vorticity layer, when a strong wake component is present in the shear layer profile, or when the heat release rate is rather high, the flame surface may exist outside the large vortices.

(5) The reaction zone embedded within the flame structure is much thinner than the convection-diffusion zone (the ratio of the two is the Zeldovich number). Resolving the reaction zone is rather demanding, especially at strains closer to the extinction strain. The difference between the two thicknesses accounts for the large number of computational element required and the enormous reduction of the time step needed during finite rate reaction simulations.

(6) While along most of the flame surface, the flame acts as a free standing flame, i.e., located between two free streams existing far away of the reaction zone, within the

6

folds and near the spiral tip opposite flames may interact in such a way that their local structures differ from that of a free flame.

I.4. Implications and the Elemental flame Model

The implications of the above observations, supported by the experimental observation on the winding of material interfaces in shear flows shown in figures 3 and 4, include:

(1) Chemical kinetics, at a reduced level, is necessary in modeling the chemical structure (reaction-diffusion zone) of the flame, and especially for highly strained elemental flames.

(2) Beyond their birth (introduction at the zone where the original interface stretches the most), elemental strained flames continue to burn as they move along the spiral. Their structure changes via the action of the unsteady strain and more significantly due to the changes in the boundary conditions (within folds and near the spiral trip).

(3) At the spiral epicenter, elemental flames die as the strain vanishes and one reactant gets fully consumed. What remains inside the main structure at the eddy center is a mixture of products and one of original reactants (depending on the original concentrations of reactants in the free streams and the stoichiometry) which is not capable of communicating with the free streams. (This can be considered as the initial state of formation/destruction of minor or secondary species.)

This new insight led us to the formulation of the elemental flame concept as a physically acceptable and direct-simulation supported model of reaction zone structure in turbulent combustion at high Damkohler number. The concept is illustrated graphically in figures 5 and 6 where both zero order (zero thickness flame) and first order models of premixed and diffusion flames are shown. In this model, elemental flames are introduced continuously where the stain rate is non-zero. As the elemental flames move closer to the large vortical structure, and as their structures are strained, their thickness reach an asymptotic limit of $\sqrt{v/\varepsilon}$. The spiraling of the flames around the structure and the

concomitant stretch of its structure helps maintain its vigor by removing the products and bringing in reactants closer to the reaction zone. Finally the elemental flame joins the central region of the eddy where it contributes to the accumulation of products in the macroelement whose radius is close to λ. Only secondary species chemistry can be sustained within this macroelement element. The results of the implementation of this model are shown in figures 7 and 8 where a comparison between a direct simulation (top), an elemental flame model at high resolution (middle), and elemental flame model at low resolution (bottom) is shown. Clearly, the concept is capable of reproducing the results of the direct simulation faithfully.

I.5. Large Structure Simulations

Based on direct simulations of shear layers using vortex methods, and extending the concepts developed to treat mixing and reaction in elemental flames, we have formulated a new algorithm to improve the efficiency of vortex simulations of reacting flows, without sacrificing any of its inherent advantages. In this algorithm, computational vortex elements represent elemental vortices introduced at zones of strong vorticity, i.e., non-zero shear, whose scales are representatives of the local vorticity thickness. Elemental vortices are then strained and elongated via the prevailing strain field forming vorticity microelements as they spin around the spiral centers. Scales normal to the vorticity are determined by striation due to folding. Finally these micro elements are combined at the spiral center to form vorticity macro elements. These macro structures continue to grow by absorbing micro element as they approach their centers, by diffusion, break up through filamentation, and stretch in the vorticity direction. Equilibrium is soon followed by irrelevance (death) as the vortical structures diffuse. By construction, as the resolution is refined, this algorithm converges to the original vortex method. The implementation of this concept which we dubbed as large structure simulation is illustrated in figures 9 and 10 where the top part of each figure shows results of direct simulations, the middle part shows large structure simulation with high resolution and the bottom part depicts large structure

8

simulation at low resolution. The figures show that the recovered vorticity field in all three cases is nearly the same while the number of elements used has been reduced by a factor of two, reducing the computational effort by a factor of four.

I.6. Elemental Flames As Reaction Zone Models at Infinite Reaction Rates

The implementation of the elemental flame model in this large structure simulation of the vorticity field to the case of infinite chemical kinetics is essentially the same as described before, i.e., introduction of elemental flames at the interface between the reacting species, the straining and elongation of these elemental flames as they spiral around the center of the macro vortex elements leading to their multiplication, the death of the elemental flames as they reach the tip of the spirals at or near the centers of the vortex macro element forming combustion macro element. The accumulation of burnt mixture at the spiral center leads to the formation of a mixing macro element which resembles a radially stratified reactor whose limit of perfect homogeneity is a well stirred reactor. We note that using a Shvab-Zeldovich formulation of the combustion problem is a natural choice here since the location of the elemental flames can always be found at a fixed, e.g., zero value of the conserved scalar concentration. This is shown schematically in figure 12.

I.7. Elemental Flames as Reaction Zoner Models at Finite Rate Reactions

To extend the above concepts to the case of finite rate kinetics, we combine the elemental flame concept with the solution of the unsteady strained flame described in detail in Appendix II and Appendix III. In both papers we describe a model in which the flame structure is computed under the assumption that the stretch rate within the flame is uniform thus by reducing the complexity of the problem enormously. In this case, the structure of elemental flame, in terms of the species and temperature profiles, under the action of the strain exerted by the layer, shown in figure 11, is computed independently and used in the immediate vicinity of that particular elemental flame in the physical domain to reconstruct the overall reaction field. The union of these elemental flames in the physical domain

9

constitutes the reaction zone structure in the turbulent field. The implementation of this concept in the shear layer is shown in figure 13.

Results shown in figures 13 and 14 represent the first implementation of the concept of finite rate kinetics elemental flames in a turbulent combustion simulations. As mentioned above, to perform these simulations, elemental flames are introduced wherever an interface between reacting species exists in the domain (birth of an elemental flame). These elemental flames are strained and elongated by the underlying shear thus by multiplying and forming an ever increasing set of unsteady strained elemental flames (USEF) around the spiraling areas of the vortex macroelements. The internal structure of the elemental flames are computed by integrating the uniformly strained flame structure equations as in Appendices II and III using a single step, a reduced multistep or a detailed kinetic mechanism. The structure calculations are then mapped back over to the physical domain to construct the reacting field there. Straining can lead to local quenching.

At the tip of the spiral inside the macro structure, the elemental flames are starved of one of the primary reactants, thus by extinguished (death). Meanwhile, elemental flame are spiraling inwards towards the center, they communicate with neighboring elements via the boundary conditions, a situation which could lead to strong changes in their structure. Figure 14 shows the reacting field, represented by the product distribution, of a shear layer as computed using this concept (top) and using direct simulations (bottom). Results show that the model reproduces the direct simulation results very well.

1.8. Uniform Strain Flame Structure Model for the Reaction Zone

The uniform strain flame model, described in detail in Appendices II and III, is based on the assumption that there exists a value of the strain, which we call the effective strain which, assumed to act uniformly throughout the flame structure, will enable us to predict, accurately, the species and temperature profiles, and burning rate, without having to solve the momentum equation. We have found that using this approximation, one can transform the original equations into a set of reaction-diffusion equations, i.e., remove the

10

troublesome convective derivatives, and thus simplify the numerical integration enormously. The equivalent effective strain has been shown to be the external applied strain adjusted to correspond to the reaction diffusion zone, i.e., to the zone where the temperature is close to the flame temperature. Using this model, we have shown that results obtained using this model agree very well with the solution of the exact equations, over a wide range of strain and for both premixed and diffusion flames. We have also implemented a four step reduced chemical kinetic scheme for methane in the computation and showed that it works well for both the premixed and diffusion flame cases.

I.9. Conclusions and future Work

The work summarized in this report describes the formulation and implementation of an efficient and accurate reaction zone model of combustion in turbulent flows at high Reynolds and Damkohler numbers. The model has been developed to mimic the observed structure of reaction zones in turbulent flows obtained by Lagrangian direct simulations under the same conditions. In particular, the reaction zone is considered locally as an unsteady strained flat flame whose structure is obtained by integrating the stretched flame equations assuming that the strain rate remains constant throughout its thickness. The flame is affected locally by the folding and spiraling induced by the vorticity structures since the boundary conditions used in integrating its equations are adjusted to reflect the proximity of the "free" streams to the reaction-diffusion zone. Moreover, the constant strain is taken to be the effective strain acting at the same zone, to improve the accuracy of the approximating. Properties of folding and spiraling material elements are exploited in removing elemental flames as they move very close to each other, or when they reach the tip of the spirals at the center of the large vortical structure. Solutions obtained using this model compare favorably with direct simulations.

Several important fundamental issues remain to be addressed. The reaction zone model developed in this work applies accurately at the high Reynolds number and Damkohler number limit. As we have seen from the results of the direct numerical

11

simulation results, even at this limit, local areas of nearly homogeneous, or radially stratified reactors, could exist within the cores of the large vortical structures due to the rapid accumulation of combustion products and the reduction of the strain rate there. The role of this these reactors is most essential in determining the post flame formation/destruction of minor species, such as CO and Nox. Work on modeling the dynamics of these reactors using, e.g., well or partially stirred reactors, would generalize the application of the current model to a wider range of governing parameters.

Another significant issue the behavior of the elemental flames in a three dimension space. The two most significant problems in three dimensions are; (1) Developing an efficient approach to compute the evolution of a material interface at scales comparable with the diffusive scales. This problem here is complicated by the extreme convolution experienced by material elements in three dimensions. (2) The possibility of encountering interacting, non parallel elemental flames. In this case, it is not obvious when one can consider neighboring elemental flames as being independent and when transport fluxes along the flames are negligible. To maintain computational efficiency, one must carefully eliminate elemental flames as they "collide" forming locally mixed reacting zones, and develop reaction zone models for these zones. (We note here that in two dimensions, the probability of formation of such zones is much lower since flames can not collide, they can only meet "face-to-face" as described earlier in the report.)

II PUBLICATIONS

1. Knio, O.M. and Ghoniem, A.F., "Stability of a differentially heated asymmetric vorticity layer," NATO Advanced Research Workshop on Vortex Flows and Related Numerical Methods, June 15-19, 1992, Grenoble, France, by J.T.Beale et al., Kluwer Academic Publishers, 1993, pp. 341-372.

2. Knio, O.M. Shi, X. and Ghoniem, A.F., "Lagrangian Simulation of Flamelet Combustion," the *AIAA 31st Aerospace Sciences Meeting*, Jan 11-14, 1993, Reno, NV, AIAA-93-0247, to appear in *Combustion and Flame.*

3. Soteriou, M.C. and Ghoniem, A.F., "Dynamics of Reacting Shear Flows, Effects of Exothermicity and Forcing," presented at the *32nd Aerospace Sciences Meeting*, Reno, NV, January 1994.

4. Soteriou, M.C. and Ghoniem, A.F., "Vorticity Dynamics of an Exothermic Spatially Developing, Forced, Reacting Shear Layer," Proceedings of the *25th Symposium (International) on Combustion*, The Combustion Institute, pp. 1265-1272, 1995.

5. Petrov, C.A. and Ghoniem, A.F., "An Unsteady Strained Flame Model for Turbulent Combustion Simulation," *32nd Aerospace Sciences Meeting*, January 1994, Reno, NV, AIAA-94-0776, 1995.

6. Luu, V.C. and Ghoniem, A.F., "Simulation of the Reacting Field in an Axisymmetric Bluff-Body Combustor Using the Vortex-Scalar Element Method—An Isothermal Fast-Chemistry Model, *33rd Aerospace Sciences Meeting*, Reno, NV, 1995, AIAA 95-0808.

7. Soteriou, M.C. and Ghoniem, A.F., "The Effect of the Inlet Boundary Condition on the Mixing and Burning in an Exothermic Shear Flow," *33rd Aerospace Sciences Meeting*, Reno, NV, 1995, AIAA-95-0807.

8. Petrov, C. and Ghoniem, A.F., "An Unsteady Strained Flame Model with Reduced Reaction Mechanism for Turbulent Combustion Simulation, *33rd Aerospace Sciences Meeting*, Reno, NV 1995, AIAA-95-0380.

9. Soteriou, M.C. and Ghoniem, A.F., Numerical Simulation of Unsteady Combustion Using the Transport Element Method," *Proceedings of the 2nd Int. Workshop on Vortex Flows and Related Numerical Methods,* Montreal, Canada, August 1995.

10. Soteriou, M. and Ghoniem, A.F., "Effects of the Free-Stream Density Ratio on Free and Forced Spatially-Developing Shear Layers, *Phys. Fluids, (B),* 2036-2050, August 1995.

11. Petrov, Constantin A. and Ghoniem, Ahmed, "The Transient Response of Strained Laminar-Premixed Flames," *Comb. and Flame*, 102: 401-417, August 1995.

12. Soteriou, M.C. and Ghoniem, A.F., "On the Application of the Infinite Reaction Rate Model in the Simulation of the Dynamics of Exothermic Mixing Layers," *Combust. Sci. and Tech.*, Vol. 105, pp. 377-397, 1995.

III SEMINARS AND LECTURES

1. 1992, National Institute of Standards and Technology, Gaithersburg, MD.

2. 1992, University of Massachusetts, Amherst, MA.

3. 1993, Princeton University, Princeton, NJ.

4. 1993, Ford Motor Company, Dearborn, MI.

5. 1993, AIAA Professional Course on Combustion Modeling in Gas Turbine, Ramjet and Scramjet, Monterey, CA.

6. 1994, Johns Hopkins University, Baltimore, MD.

7. 1995, Sandia National Laboratories, Albuquerque, NM.

8. 1995, United Technologies, East Hartford, CT.

IV PERSONNEL

During the funding period, 1992-1995, the following students were supported to perfrom the research descibed here:

1. Marios Soteriou, finished his Ph.D. and stayed on as a postdoctor.

2. Van Luu, Ph.D. student, expected to finish June 1996.

3. Constantine Petrov, finished his M.Sc. and stayed on as a Ph.D. student,

4. Jean-Claude Saghbini, M.Sc. student.

V OUTSIDE INTERACTIONS

1. General Electric, with Sanjay Correa and Hokam Mongia.

2. Altex Technologies, with Mehdi Namazian and John Kelly

3. Sandia National Laboratory, Livermore, with Robert Schaffer.

3. Ford Motor Company, with Chris Kent and Gary Stromolo.

4. Aerodyne Research, with James Stickler.

5. Sandian National Laborator, with Lou Gritzo and James Strickland.

6. United Technology Research Center, with Lou Chiapatta and William Proscia.

TIME=10.00   STEP=46   ELEMENTS= 2473

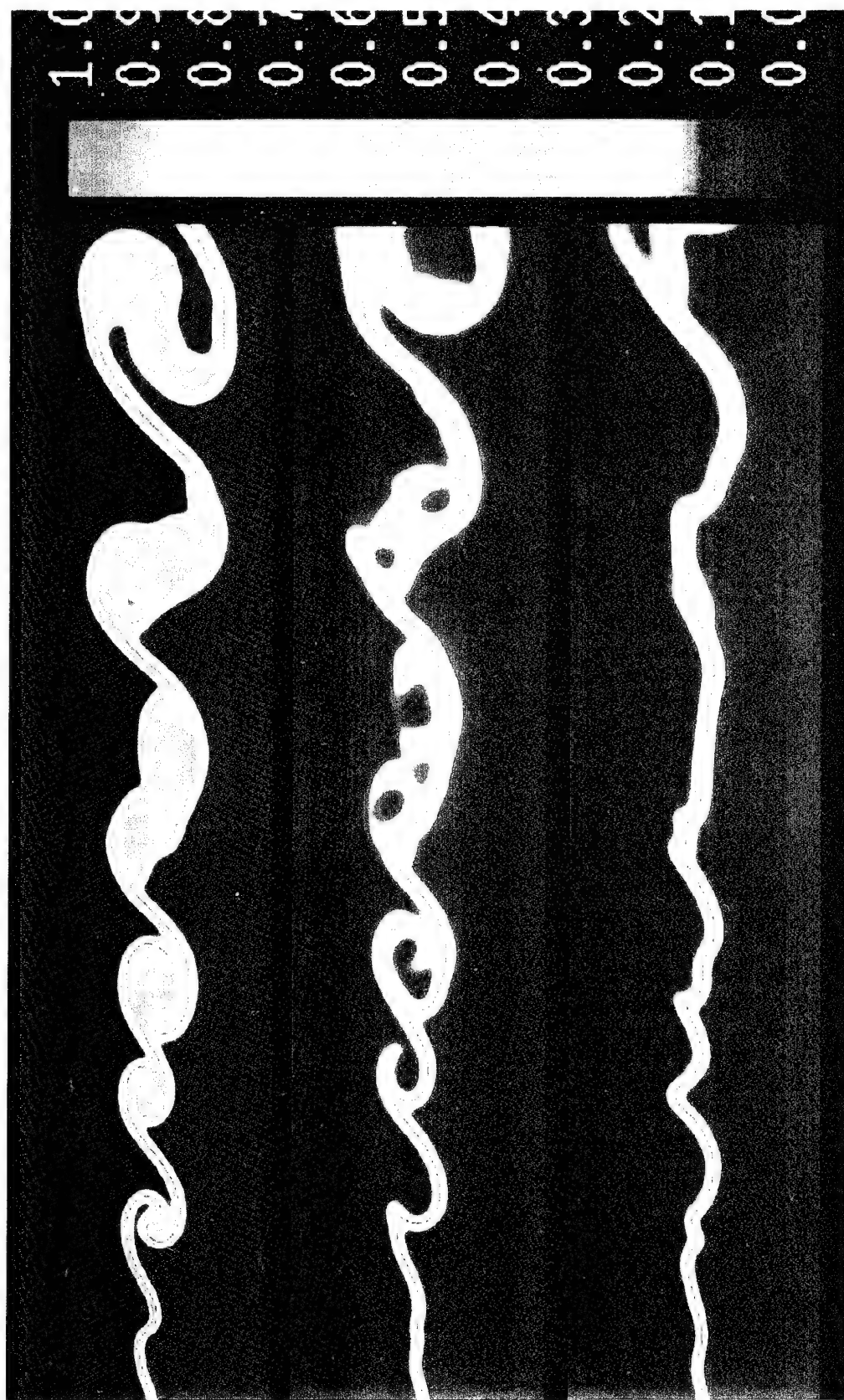TIME=10.00   STEP=400   ELEMENTS= 2810

TIME=10.00   STEP=400   ELEMENTS= 1439

The spatial evolution of the material line originating at the point of maximum scalar gradient as the misalignment of the latter with the point of maximum vorticity increases from 0, top, to d, middle, to 2d, bottom (d=0.0585).

Figure 1.

The effect of the initial misalignment of the points of maximum vorticity and maximum scalar-gradient on the evolution of the downstream product mass-fraction field. The misalignment increases from top to bottom as 0d, 1d, 2d, where d=0.0585.
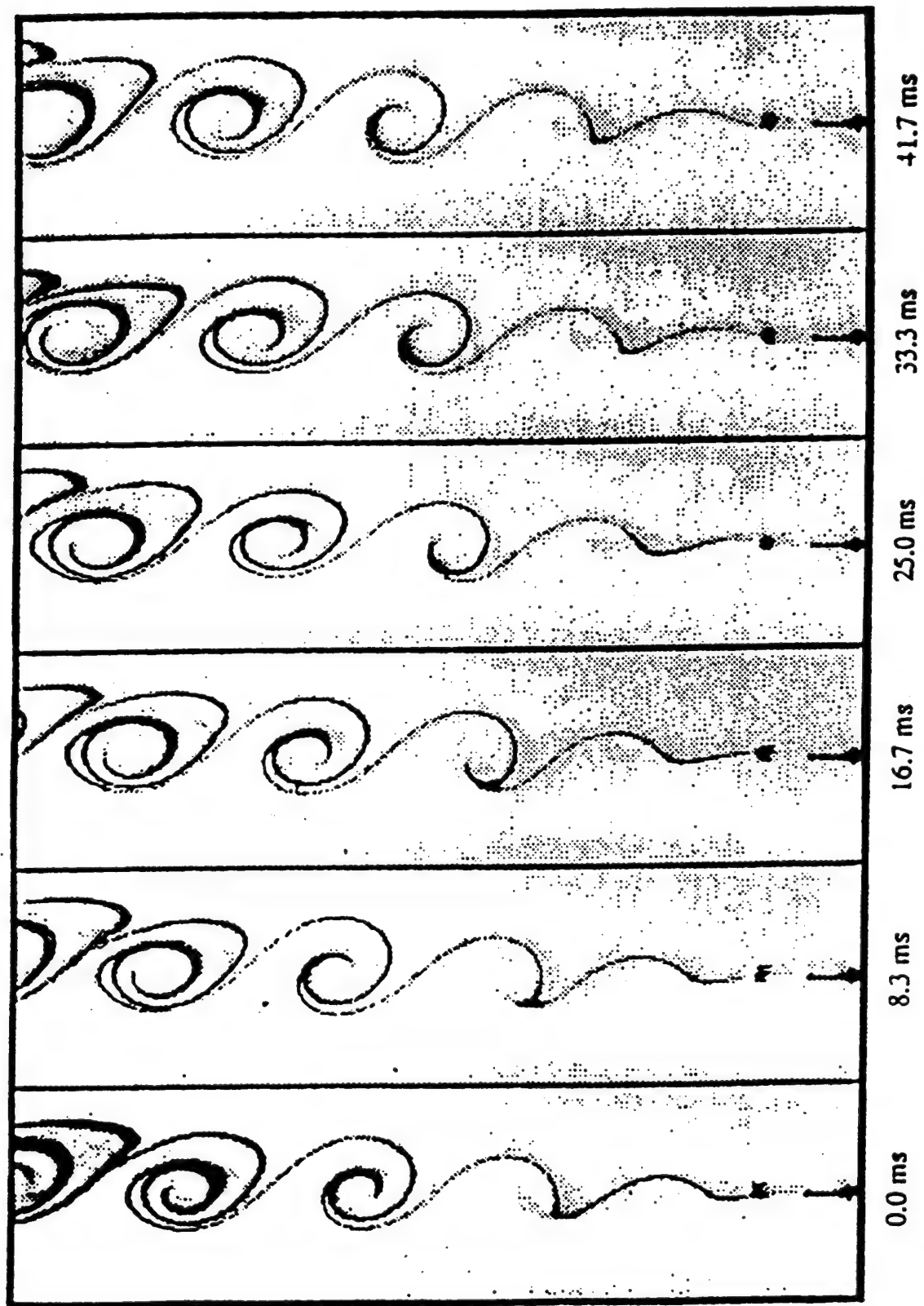
Figure 2.

Figure 3.   Phase locked images of a two-dimensional, shear layer driven at 20 Hz.*

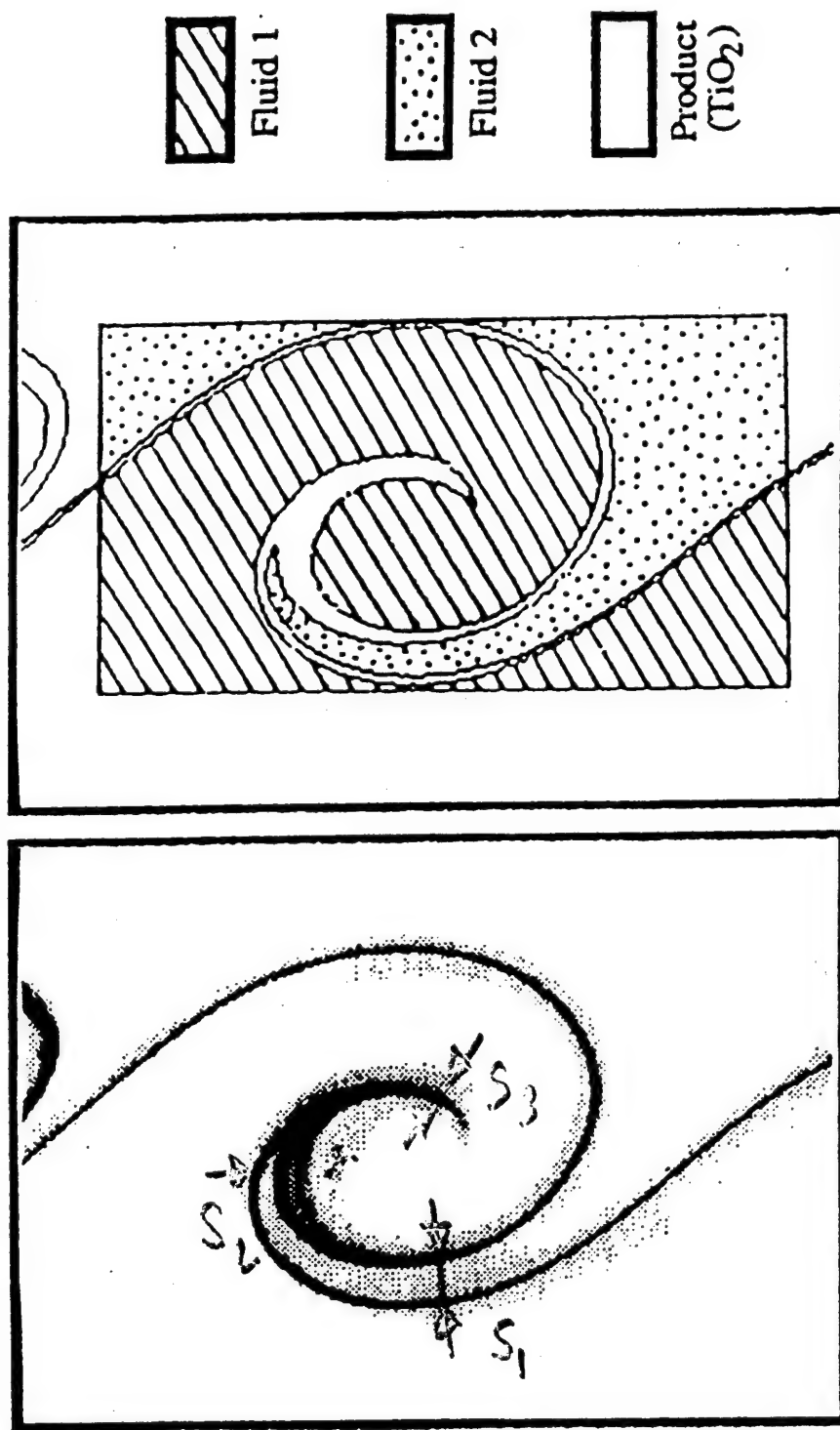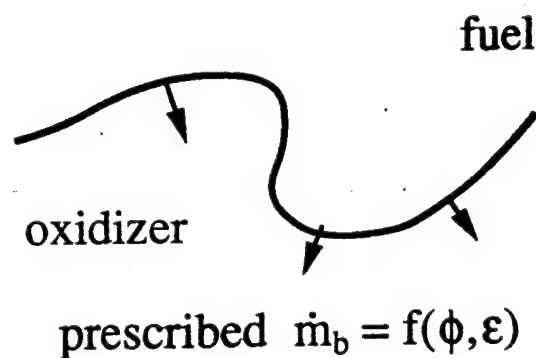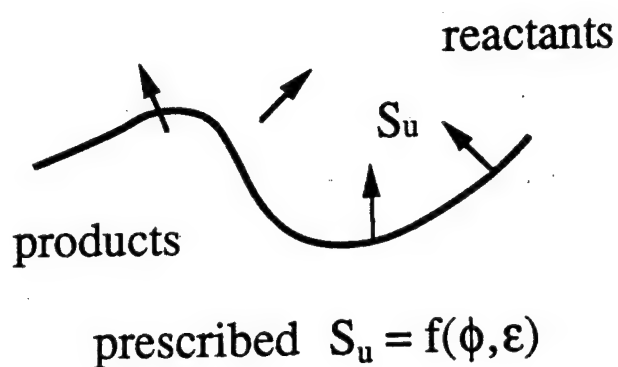*T.H. Chen and R.D. Hancock, AIAA J, 33, 5, pp 949-952, May 1995.

Fluid 1

Fluid 2

Product (TiO$_2$)

2(a) Digital Image

2(b) Intensity Contour Lines

Figure 4. Definition of interfaces and areas from contour analysis.

REACTION ZONE MODELS FOR TURBULENT COMBUSTION

PREMIXED   **_DIFFUSION_**

(1) Zero-order interaction: flame interface

reactants

fuel

S_u

products

oxidizer

prescribed $S_u = f(\phi, \varepsilon)$

prescribed $\dot{m}_b = f(\phi, \varepsilon)$

(2) First-order interaction: Flame elements

reactants

fuel

products

oxidizer

reactants $y \to +\infty$

$y \to +\infty$ fuel

Reaction zone

T

T

x

x

$$\varepsilon = \frac{\partial u}{\partial x}$$

products $y \to -\infty$

$y \to -\infty$ oxidizer
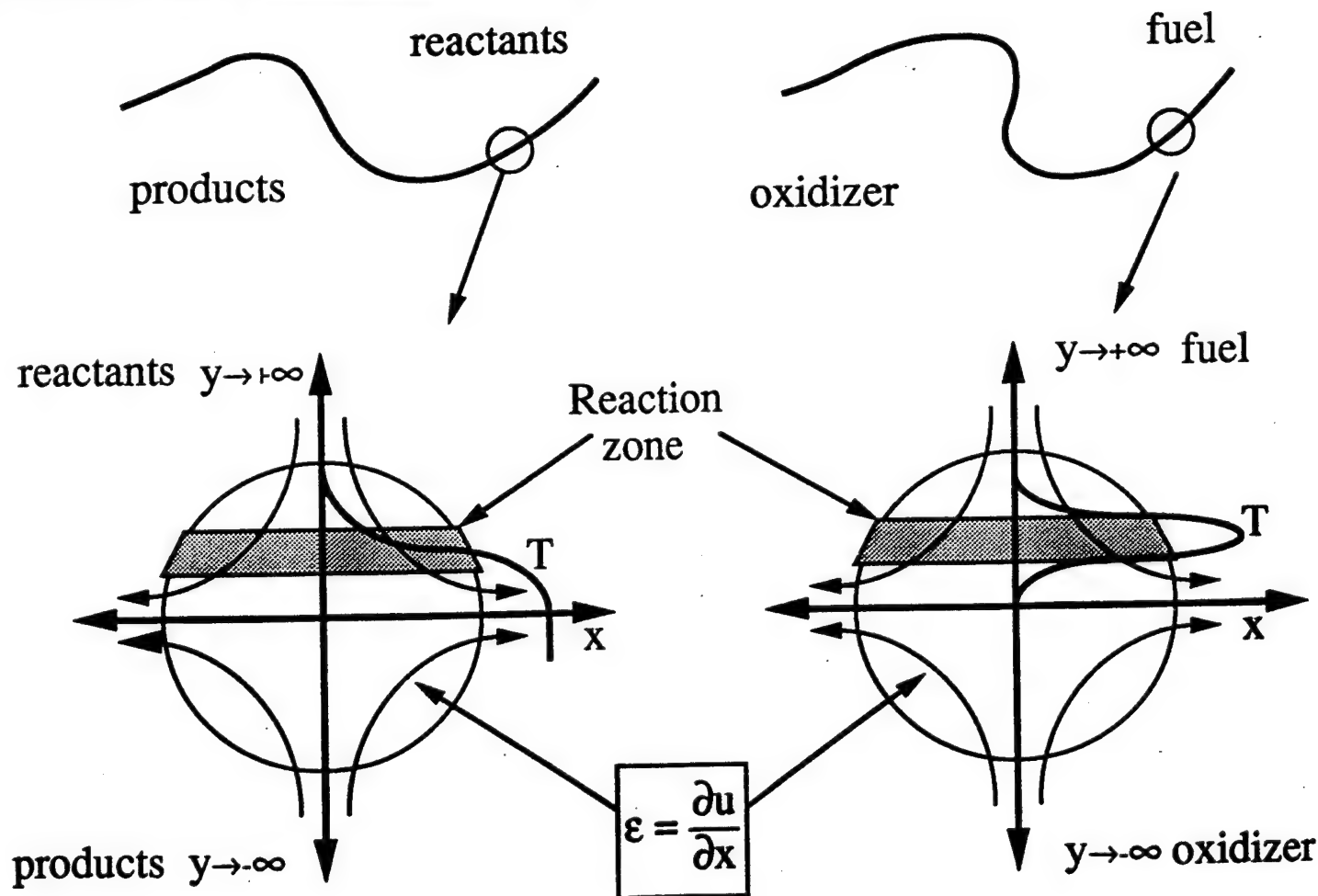
Figure 5.

THE FLAME ELEMENT MODEL

$$\varepsilon(t) = \frac{1}{\delta}\frac{d\delta}{dt} = \frac{du}{dx}$$

Physical domain

flame front

$\delta(t)$

Flame locally
flat, strained in
its own plane.

$$\varepsilon(t) = \frac{\partial u}{\partial x}$$

Solution domain

Seek solutions along stagnation
line x=0 (u=0), and for small y
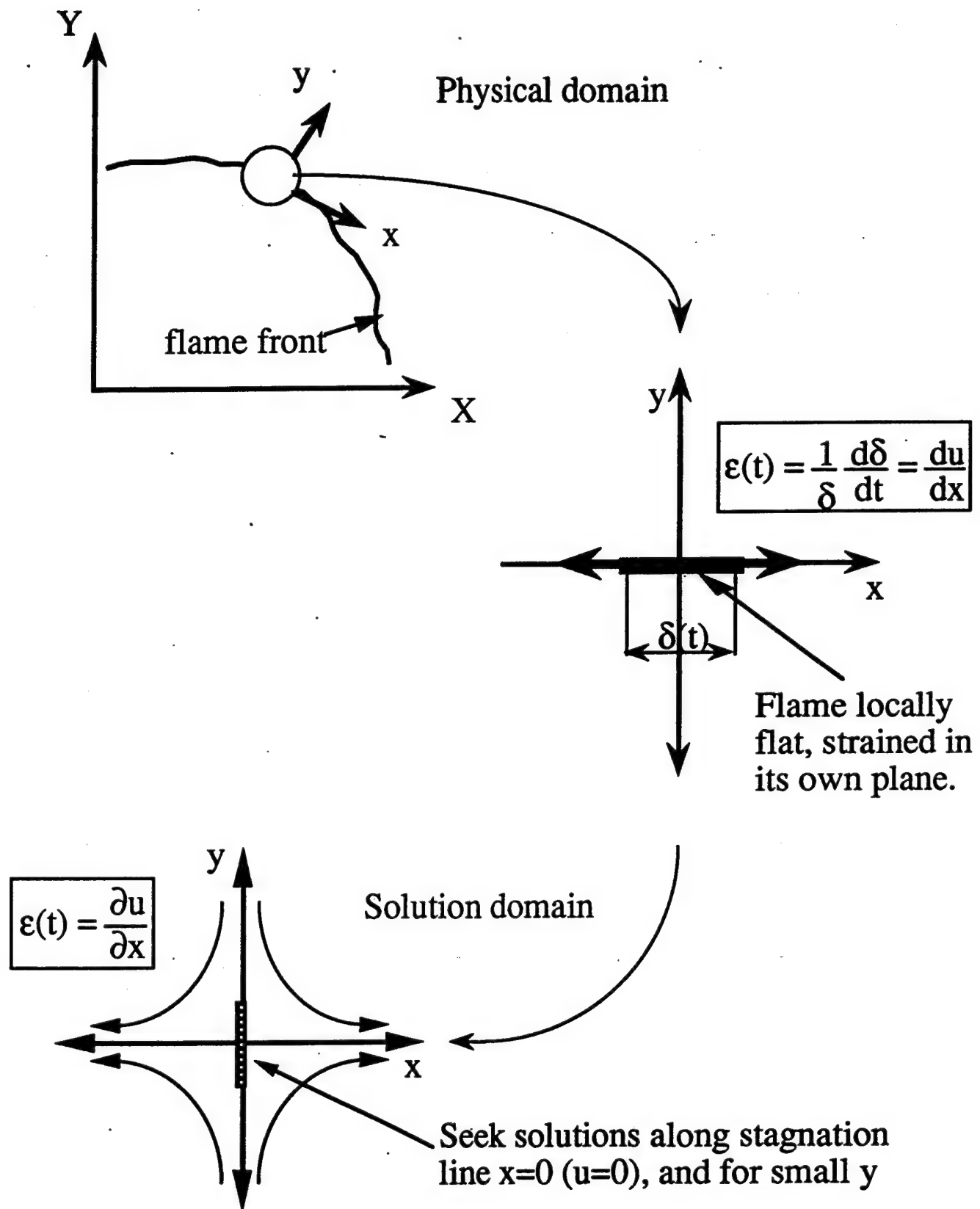
Figure 6.

TIME = 10.00   STEP = 4   ELEMENTS = 2810

TIME = 10.00   STEP = 400   ELEMENTS = 1887

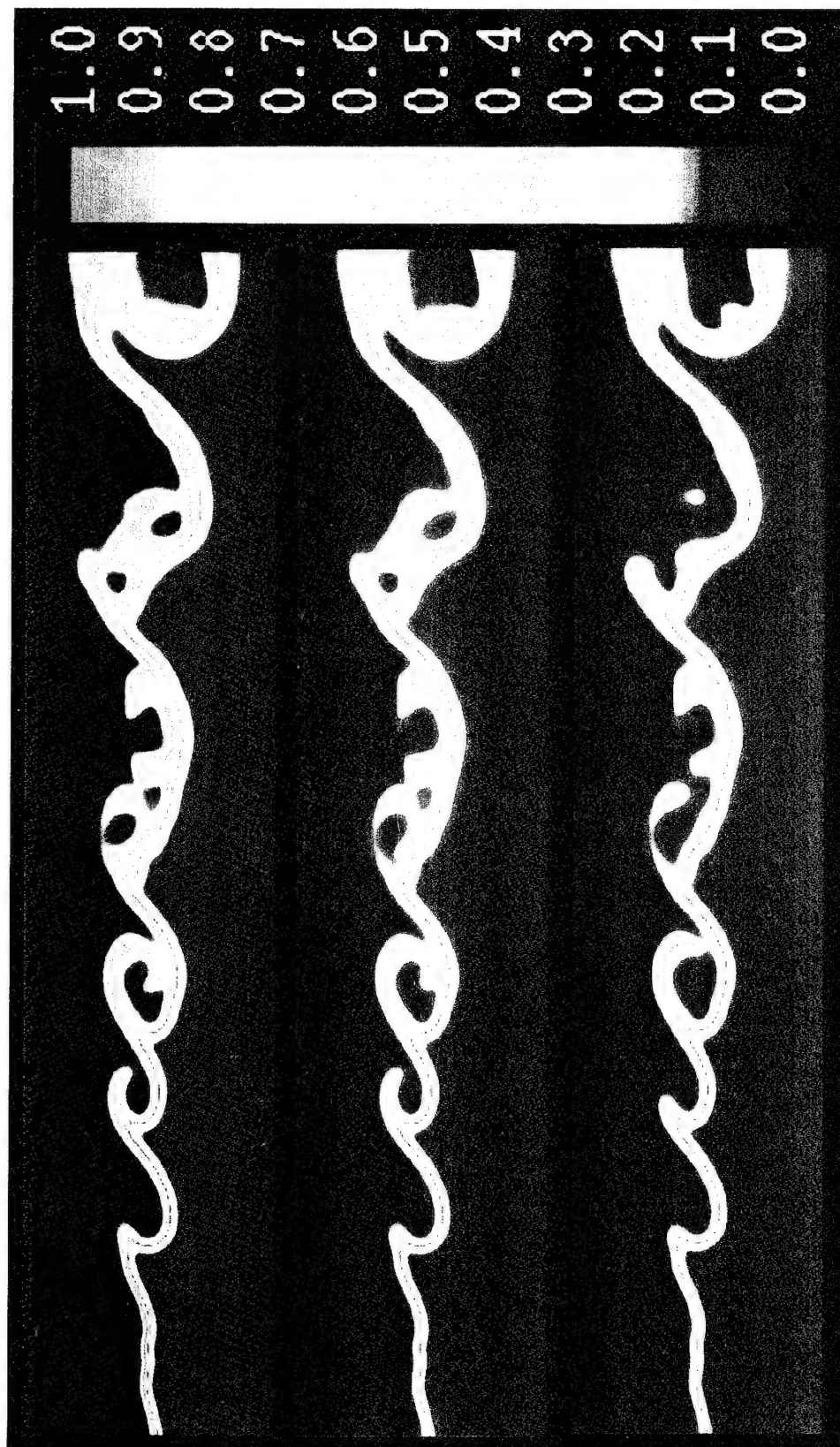TIME = 10.00   STEP = 400   ELEMENTS = 1224

The spatial evolution of the material line originating at the point of maximum scalar gradient using the transport element method (top) and that incorporating the concept of combustion macrolements for two values of the maximum tip angle a=23 (middle) and a=47 (bottom).

Figure 7.

The product mass fraction obtained using the transport element method (top), and that incorporating the concept of combustion macroelements for two values of the maximum tip angle a=23 (middle) and a=47 (bottom).

Figure 8.
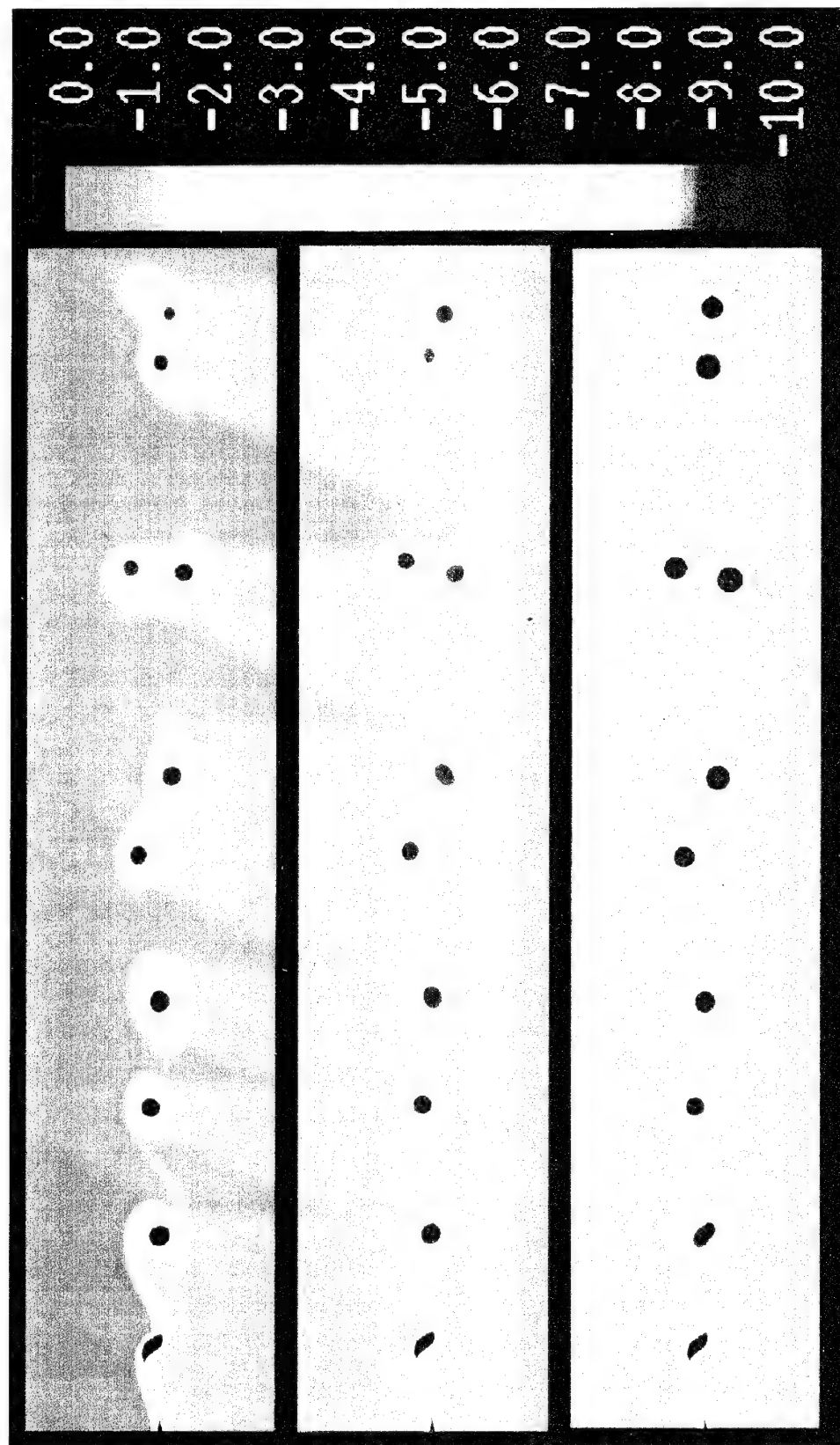
The spatial evolution of the vortex elements using the vortex element method (top) and that incorporating the concept of vorticity macrolements for two values of the growth parameter $c=1$ (middle) and $c=2$ (bottom). The velocity vector (with respect to the mean flow) at the center of the elements is indicated.
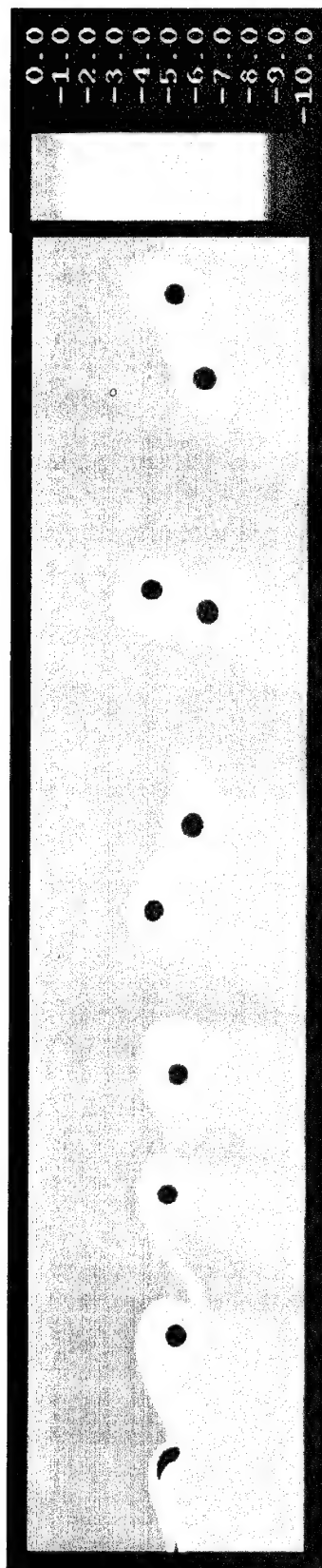
Figure 9.

The vorticity obtained using the vortex element method (top), and that incorporating the concept of vorticity macroelements for two values of the growth parameter c=1 (middle) and c=2 (bottom).

Figure 10.
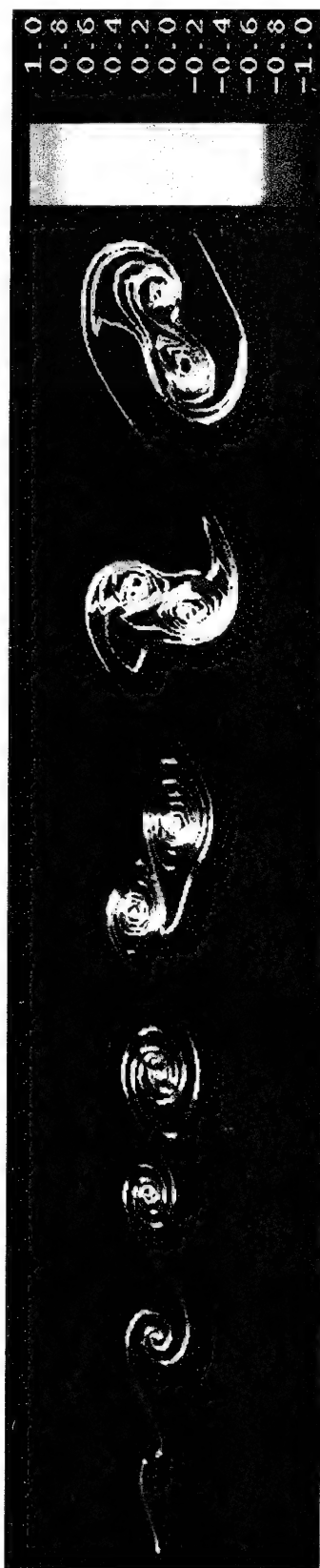
The strain-rate along a material line which originates at the point of maximum vorticity.

The vorticity field which leads to the formation of the material line shown above

Figure 11.

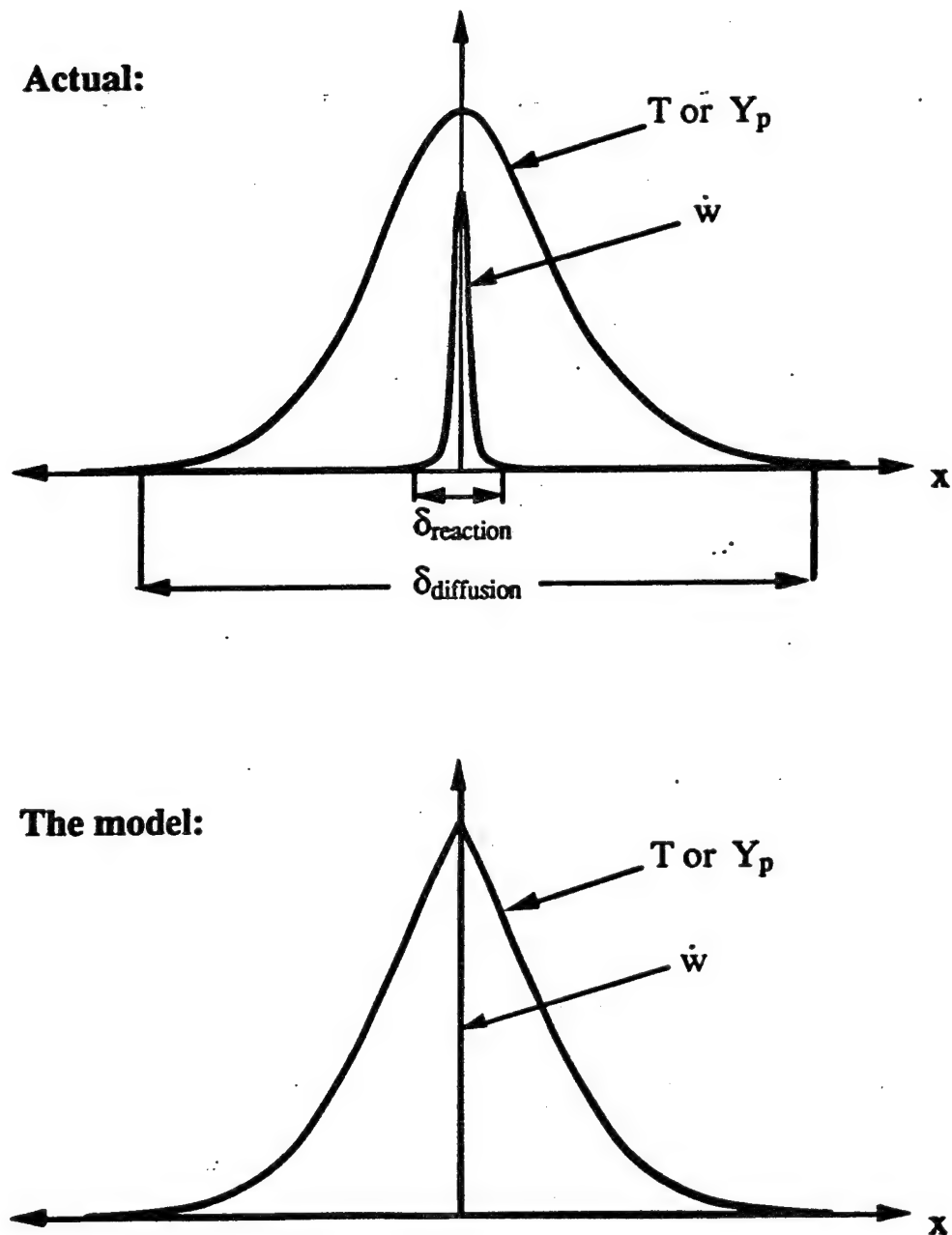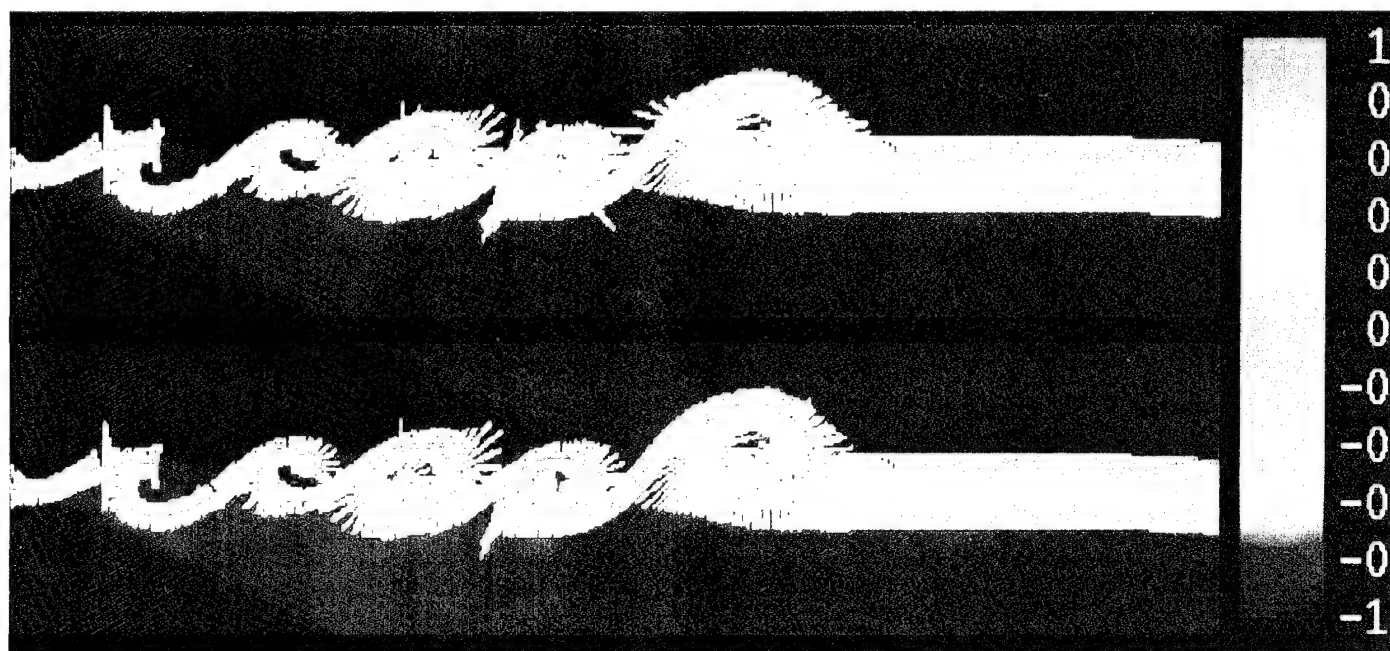# The infinite reaction rate approximation of the diffusion flame:

Figure 12.

Product mass-fraction obtained from the flamelet solutions for non-intyeracting flamelets (top) and interacting flamelets (bottom).

Figure 13.
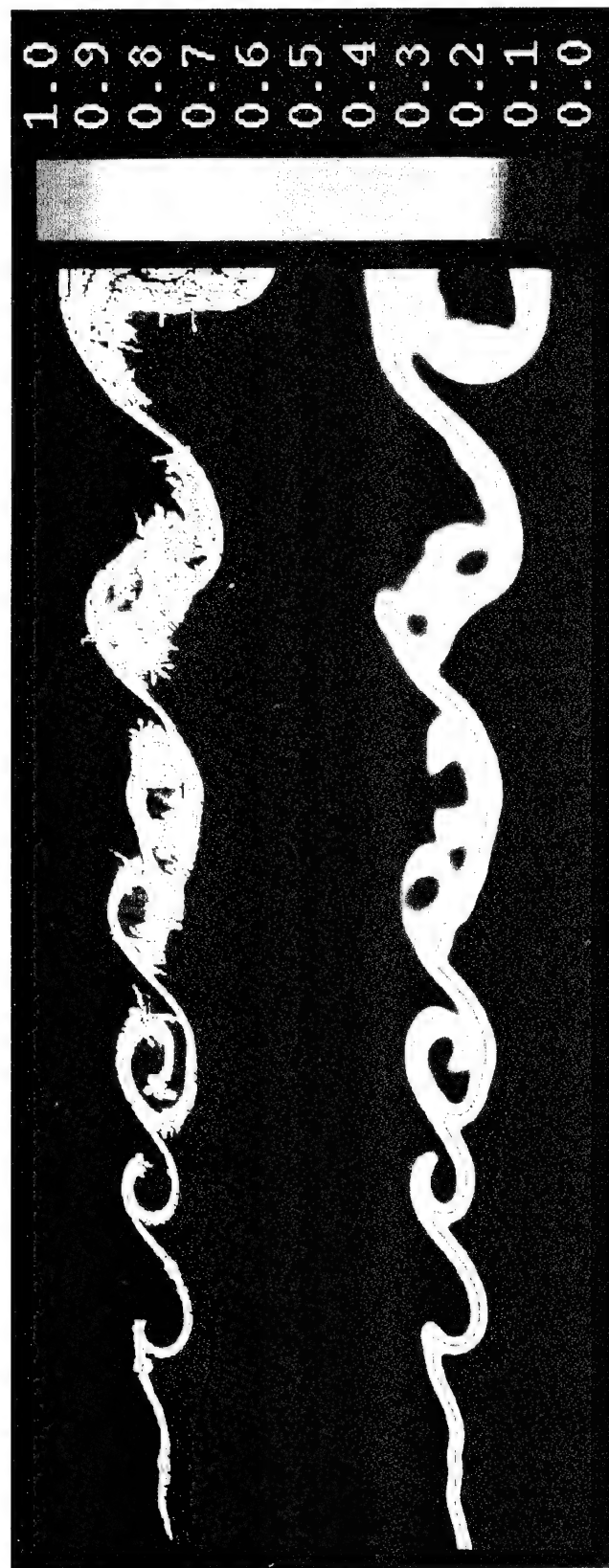
Product mass-fraction distribution obtained using the elemental flames (top), versus that of the transport element method at infinite reaction rate (bottom).

Figure 14.

APPENDIX I

AIAA-95-0807

The Effect of the Inlet Boundary Condition on the Mixing and Burning in an Exothermic Shear Flow

M.C. Soteriou and A.F. Ghoniem
Massachusetts Institute of Technology
Cambridge, MA 02139

**33rd Aerospace Sciences
Meeting & Exhibit
January 9-12, 1995 / Reno, NV**

THE EFFECT OF THE INLET BOUNDARY CONDITION ON THE MIXING AND BURNING IN AN EXOTHERMIC SHEAR FLOW

Marios C. Soteriou[1] and Ahmed F. Ghoniem[2]
Massachusetts Institute of Technology
Cambridge, MA 02139

ABSTRACT

The effects of the presence of a wake component in the inlet velocity profile, on the dynamics of a non-premixed exothermic shear layer are investigated numerically. The Lagrangian transport element method is used to obtain two-dimensional simulations of the flow. Combustion is modeled using an infinite reaction rate model based on the Shvab-Zeldovich formulation. Simulations with and without combustion exothermicity are obtained for two different inlet conditions: One with an errorfunction inlet velocity profile, and one in which this profile includes a Gaussian wake deficit. Results indicate that the presence of the wake component in the inlet velocity profile alters the downstream flow and its interaction with the exothermic reacting field due to two main reasons: (i) The wake-modified profile is much more unstable than the errorfunction. As a result it yields higher downstream rates of mixing and burning. (ii) The relative location of the reaction interface with respect to the vorticity field differs between the errorfunction and the wake-modified cases. As a result, even though combustion exothermicity decreases the burning in both cases as compared to their corresponding non-exothermic flow, it does so via different mechanisms. In the errorfunction flow the reaction interface is located at the center of the single sign vorticity layer which characterizes the vorticity field. The reduction in the burning in this case is a result of the decay of the vorticity field due to volumetric expansion which delays the rollup and results in weakened downstream vortical structures. In the wake-modified case the reaction interface is located between two vorticity layers of opposite signs. The layer with the same sign as that of the errorfunction case dominates the dynamics. In this case, however, the reaction interface is initially located outside it and gets wrapped around it as the this layer gets destabilized.

[1] Post-doctoral Research Associate, member AIAA.
[2] Professor, Associate Fellow AIAA.

The reduction in the burning in the exothermic case comes about via a delay in this interaction of the vorticity layer and the reaction interface as volumetric expansion pushes the two away from one another. The same mechanism is also responsible for a delay in the interaction of the two vorticity layers of the wake-modified flow with the consequence that the wake region survives further downstream.

I. INTRODUCTION

Numerical simulations of turbulent reacting shear layers in which the governing equations are integrated directly without averaging and/or resorting to turbulence closure modeling have been commonly used to elucidate the mechanisms of interaction between turbulence and combustion in shear flows [e.g. 1-6]. These flows are dominated by large scale vortical structures [7, 8] whose presence and impact on the mixing and combustion cannot be directly captured using turbulence closure and existing turbulence-combustion interaction models, respectively, and hence must be directly computed.

Recently, these simulations have enabled the systematic and detailed investigation of the effect of combustion exothermicity on the flow physics [4-6]. In this regard, it has been shown that the mixing enhancement by the enlargement of the flame surface area due to the action of the large scales plays a key role in burning augmentation. Moreover, it has also been concluded that exothermic energy impacts the dynamics in such a way that the overall growth rate of the mixing zone is reduced with respect to that observed in the non-exothermic flow. This reduction, which takes place despite the increase in volume due to the deposition of exothermic energy, is, for the most part, a result of the decay of the vorticity field due to volumetric expansion. It has also been established that the structure and interactions of the vortices are altered in the exothermic flow due to the redistribution of vorticity by the baroclinic mechanism.

The validity of these conclusions, however, is restricted by the limiting assumptions used to obtain the corresponding results. One common source of contention

is the simplification of the inlet conditions. This is particularly troublesome when one considers the well known sensitivity of the flow to these conditions [8,9]. In the studies noted above, the inlet velocity profile, which due to the presence of the upstream splitter plate separating the two streams includes a wake component, is smoothened into a monotonically varying one, usually an errorfunction or a hyperbolic tangent. The origin of this assumption, which is motivated by numerical considerations, lies in the study of the non-reacting flow. Early experimental studies indicated that in a non-reacting flow the wake component of the mean velocity profile is quickly annihilated downstream of the splitter plate [7, 9].

Linear stability analysis of the flow also points in the same direction. In a number of studies it has been shown that in contrast to a single mode of instability of the monotonically varying profile, a velocity profile with a wake component exhibits two modes of instability, namely the 'sinus' or 'shear layer' and the 'varicose' or 'wake' modes [10-13]. In the vast majority of conditions, however, the sinus mode, which is similar to that of the monotonic profile, albeit with a different growth rate and phase speed, was found to dominate. As a result, one may hope to capture the essential features of the flow, at least in a qualitative sense, by using the monotonic profile.

Numerical simulations of non-reacting shear layers using a monotonically varying inlet profile were successful in reproducing the flow instantaneous and mean dynamics [e.g 14, 15]. We believe, however, that the effectiveness of this type of inlet condition in the non-reacting flow does not necessarily imply its applicability to the exothermic reacting flow. A number of important issues suggest that such an extension may be unjustified. First, in the reacting case a variable density field is present. The studies of the linear stability of the flow mentioned earlier clearly indicate that the flow destabilization is modified in the presence of a variable density field. The probability of exciting the varicose mode may increase, particularly when the thickness of the density profile is much smaller than that of the velocity profile. More important, however, is the issue of volumetric expansion. The flow arrangement at the inlet implies that deposition of exothermic energy, and hence volumetric expansion, will take place inside the wake region. The possibility that this may have substantial effects on the downstream dynamics cannot be disregarded.

In this paper, we investigate the impact of the wake component of the inlet velocity profile on the exothermic flow, by comparing results of numerical simulations in which such an inlet profile is used, with those of corresponding simulations with a monotonically varying inlet profile. The transport element method is used to provide high resolution two-dimensional simulations of the flow. The reacting field is modeled using an infinite reaction rate model based on Shvab-Zeldovich conserved scalars. In earlier work we have shown this model to be effective in enabling the prediction of the effects of combustion exothermicity on the reacting field, as long as the reaction is fast compared

to the flow time scale [16]. Thus, the results shown herein apply in this limit.

II. FORMULATION AND NUMERICAL SCHEME

The details of the formulation and numerical scheme used in the simulation of infinite reaction rate exothermic shear flow are given in Refs.[16, 17]. Herein only a summary of the main features is provided.

Formulation

A two-dimensional high Reynolds number, non-premixed, exothermic reacting shear flow is considered. Compressibility effects are allowed only in the low Mach number limit, the effects of gravity are neglected, all species are assumed to behave as perfect gases with equal molar masses and constant and equal diffusivities and specific heats, and combustion to occur according to a single step, irreversible, mole preserving, infinite rate reaction.

Under the infinite reaction rate model reactants burn completely upon contact. As a result, the reaction zone collapses onto an interface which separates the two reactants. The solution of such a reacting field which experiences discontinuities in the gradients of the primitive scalar variables, is facilitated by the introduction of Shvab-Zeldovich (SZ) conserved scalars which are piecewise continuous in the whole domain.

The resulting governing equations are transformed into a vorticity—scalar-gradient form. This is accomplished by decomposing the velocity field into expansion, potential and vortical, components using the Helmholtz decomposition and representing the first two by the appropriate form of the continuity equation and the third by the streamfunction equation. The latter necessitates the solution of the vorticity equation which is established by taking the curl of the momentum equation. For the scalar field the transport equations of the gradients of the SZ variables are established, i.e. in non-dimesionalized form,

$$u = \nabla \Phi_e + \nabla \Phi_p + \nabla x(\ \Psi \hat{k}) \ ; \qquad (1)$$

$$\nabla^2 \Phi_e = -\frac{1}{\rho}\frac{d\rho}{dt}, \quad \nabla^2 \Phi_p = 0, \quad \text{and} \quad \nabla^2 \Psi = -\omega \ ; \quad (2a,b,c)$$

$$\frac{d\omega \hat{k}}{dt} = -(\nabla \cdot u)\ \omega \hat{k} + \frac{\nabla \rho x \nabla p}{\rho^2} + \frac{1}{Re}\nabla^2 \omega \hat{k} \ ; \qquad (3)$$

$$\rho T = 1 \ ; \qquad (4)$$

$$\phi^* \eta_1 + \eta_2 \rightarrow (1+\phi^*)\eta_p \ ; \qquad (5)$$

$$Y_1 + Y_2 + Y_p = 1 \quad ; \qquad (6)$$

2

$$\lambda = Y_1 - \phi Y_2 \qquad \text{and} \qquad \gamma = T - \frac{Q_o\phi}{1+\phi} Y_p \; ; \qquad \text{(7a,b)}$$

$$\frac{dg}{dt} = -g\cdot\nabla u - g x(\,\widehat{\omega k}) + \frac{1}{Pe}\nabla^2 g \;, \qquad \text{(8)}$$

where $\quad g = \nabla\lambda$ or $\nabla\gamma$.

In the above, $u = (u,v)$ is the velocity vector in an $x = (x,y)$ right-handed Cartesian coordinate system, t is time, $\nabla = \left(\frac{\partial}{\partial x}, \frac{\partial}{\partial y}\right)$ and $\frac{d}{dt} = \frac{\partial}{\partial t} + u\cdot\nabla$. Φ_e is the expansion velocity potential, Φ_p is the velocity potential related to the boundary conditions, Ψ is the streamfunction, $\widehat{\omega k} = \nabla x u$ is the vorticity, where $\widehat{k}$ is the unit vector normal to the plane of motion, p is the pressure, ρ is the density and T is the temperature. Re and Pe are the Reynolds and Peclet numbers, respectively, -non-dimensionalizing scales are given in Section III. Y_i is the mass-fraction of species η_i, $i = 1, 2$ for the reacting species, $i = p$ for the product, ϕ^* and ϕ are the molar and mass stoichiometric ratios, respectively, and Q_o is the normalized enthalpy of reaction.

Finally, it is clarified that the reconstruction of the reacting scalar field from the SZ solutions is accomplished using equations (6) and (7) and the knowledge that reactants cannot coexist:

$$\lambda \geq 0 \quad Y_1 = \lambda, \quad Y_2 = 0, \quad Y_p = 1 - \lambda,$$

$$\text{and} \qquad T = \gamma + \frac{Q_o\phi}{1+\phi}(1-\lambda) \qquad \text{(9a)}$$

$$\lambda \leq 0 \quad Y_1 = 0, \quad Y_2 = -\frac{\lambda}{\phi}, \quad Y_p = 1 + \frac{\lambda}{\phi},$$

$$\text{and} \qquad T = \gamma + \frac{Q_o\phi}{1+\phi}(1 + \frac{\lambda}{\phi}) \qquad \text{(9b)}$$

It is noted that the above equations define $\lambda = 0$ as the locus of the reaction interface.

Numerical Scheme

The governing equations are solved using the transport element method. In this Lagrangian, grid-free numerical scheme the vorticity, divergence and SZ gradient fields are discretized over a number of elements of finite area, strength and overlapping Gaussian cores.

Evolution of the flow and scalar fields is achieved by advecting the elements with the local velocity vector while at the same time updating their properties by numerically integrating the governing transport equations.

This is accomplished in two fractional steps. In the first step, which includes all processes other than diffusion, the elements are transported and their strength is adjusted as a result of the numerical integration of the non-diffusive transport equations. For the vorticity, the use of the circulation equation, with the material acceleration substituting the pressure gradient in the baroclinic term, is preferred due to its simplicity. For the SZ gradients, the governing equation is substantially simplified using flow kinematics to relate the gradient evolution to that of the material line stretch. The latter is readily available due to the Lagrangian nature of the scheme.

In the second fractional integration step, diffusion effects are simulated using the core expansion scheme. In the current implementation of this scheme every step of core expansion is followed by a rediscretization step which returns the cores to their original size while modifying the element strength. This avoids problems associated with the transport of large cores.

The severe distortion of the flow-computation map due to the Lagrangian transport may lead to deterioration of the accuracy of the solution due to insufficient core overlap. This is prevented by continuously inserting/removing elements in regions of high tensile/compressive strains, as assessed by the distance between neighboring elements. This insertion/removal is carried out according to local conservation laws.

The velocity field at any given time is established by obtaining the vortical and expansion components via convolutions over the fields of the vortex and expansion elements, respectively, and the potential component using a Schwartz–Christoffel conformal mapping. The aforementioned convolutions result from the integral solutions of the corresponding Poisson equations, Eqs.(2a,2c), in an unbounded domain. Bounded domains are simulated using the concept of images. For the scalar field a similar convolution is utilized by realizing that the scalar and its gradient may also be related by a Poisson equation (i..e. $\nabla^2 s = \nabla\cdot g$).
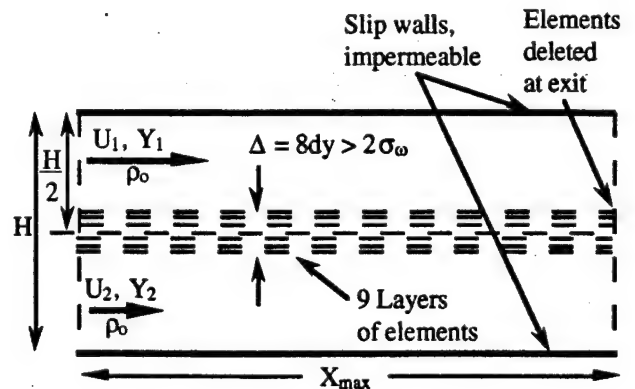

Figure 1. Schematic representation of the geometry of the computational domain together with the initial element configuration and some of the boundary conditions

3

IV. PROBLEM STATEMENT

A two-dimensional channel geometry of height H and length X_{max} is considered as shown in Fig.1. Two parallel fluid streams of different velocities but same density, ρ_o, and temperature, T_o, previously separated by a thin splitter plate located half way between the walls, mix along the channel length. Each stream carries a single reactant. H, ρ_o and T_o are used as the reference length, density and temperature, respectively, while U_1, the velocity of the top, fast, stream, as the reference velocity.

The top and bottom walls are modeled as rigid, slip, impermeable and adiabatic planes. At the exit, uniform conditions are assumed for the potential components while for the rotational-gradient components the corresponding elements are simply deleted as they exit the domain.

Two sets of inlet conditions are considered, identified as the 'errorfunction' and the 'wake-modified' conditions. Their main difference lies in that the first includes the effects of the presence of the wake which is reminiscent of the boundary layers formed along the walls of the upstream splitter plate, while the second does not. This is in accordance with the main objective of this paper which is to investigate the importance of the presence of the wake deficit in the inlet velocity profile on the exothermic flow dynamics.

The two sets of conditions are specified under the following general profiles for the velocity and the S-Z scalars:

$$u\left(\frac{y^*}{\sigma_\omega}\right) = \left(\frac{1+r}{2}\right) + \left(\frac{1-r}{2}\right)erf\left(\frac{y^*-y_o}{\sigma_\omega}\right) - \frac{W}{\sqrt{\pi}}exp\left(-\frac{(y^*-y_o)^2}{\sigma_\omega^2}\right) \quad (10)$$

$$\lambda\left(\frac{y^*}{\sigma_g}\right) = \left(\frac{1-\phi}{2}\right) + \left(\frac{1+\phi}{2}\right)erf\left(\frac{y^*}{\sigma_g}\right) \quad (11)$$

$$\gamma\left(\frac{y^*}{\sigma_g}\right) = 1 \quad (12)$$

where erf and exp are the errorfunction and exponential functions, respectively, $y^* = y - 0.5$, σ_ω and σ_g are the standard deviations of the related vorticity and scalar gradient profiles, respectively, $r = \frac{U_2}{U_1}$ is the velocity ratio, W is the wake component strength and y_o is a cross-stream adjustment length which allows the wake-modified profile to experience its minimum at $y^* = 0$.

For both conditions $r = 0.5$ and $\phi = 1$. For the errorfunction condition both W and y_o are set equal to zero while for the wake-modified condition $W = 1.1$ and $y_o = \frac{\sigma_\omega}{W}\left(\frac{1-r}{2}\right)$. The thickness of the velocity profile for both conditions is $\sigma_\omega = \sigma_{\omega W} = \sigma_{\omega E} = 0.039$. Both these velocity profiles are shown in Fig.2 which displays the profile specified by Eq.(10) for a variety of values of W.
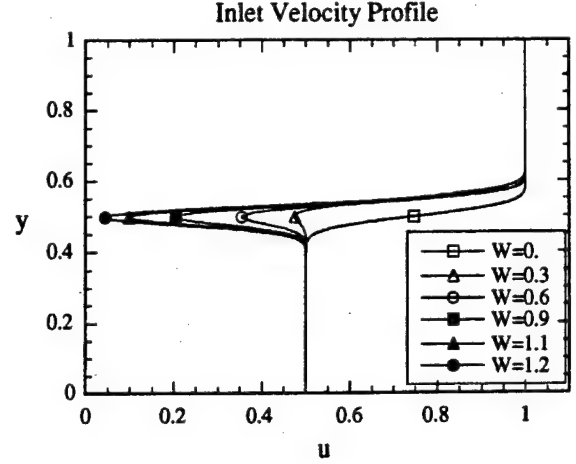

Figure 2. The velocity profile described by Eq.(10) for $r = 0.5$, $\sigma_\omega = 0.039$ for various values of the wake parameter W. Cases with $W = 0$ and 1.1 are used as inlet conditions in the numerical simulations.
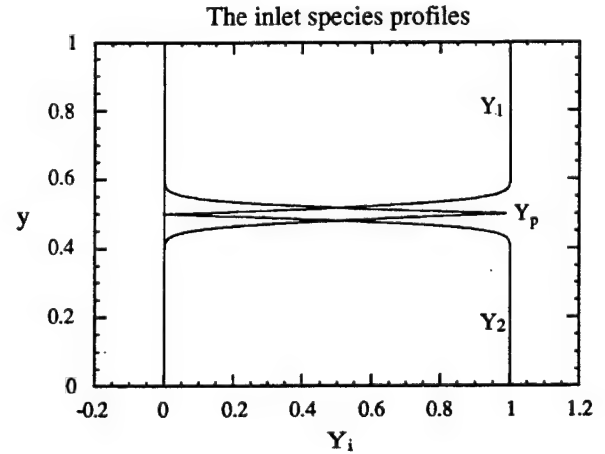

Figure 3. The species mass-fraction profiles specified at the inlet for the errorfunction inlet profile flow.

The choice of the SZ scalar profiles, like those of the velocity profiles is motivated by the flow physics. Equations (9) imply that the specification of the λ inlet profile as an errorfunction suggests that the reacting species, in the regions where they exist, will also be errorfunctions. As a result the product follows a profile which experiences a sharp peak in the neighborhood of the reaction region. The choice of γ as unity implies that temperature variation is only a consequence of reaction. (It is noted that this choice together with the nature of the governing transport equations and the rest of the boundary conditions given earlier imply that $\gamma(x,t) = 1$. As a result the computational solution is substantially simplified.) These scalar profiles which are shown in Fig.3 for the

4

errorfunction inlet condition for which the thickness of the scalar profiles is the same as that of the velocity profiles, i.e. $\sigma_{gE} = \sigma_\omega$, are not unlike those encountered downstream of the splitter plate. For the wake-modified inlet condition the scalar profiles are assumed to be thinner than those of the errorfunction case, and hence than the velocity profiles as well. Specifically $\sigma_{gW} = 0.5\,\sigma_\omega$. This is to approximate the unmixed nature of the scalar profiles just downstream of the splitter plate. It is noted that the particular choice of this thickness, as well as the earlier choice of W, are limited by discretizing constrains. The errorfunction scalar profiles are thicker due to the assumed mixing between the edge of the splitter plate and the location of the inlet condition which, as was stated earlier, is assumed to annihilate the wake component of the velocity profile.
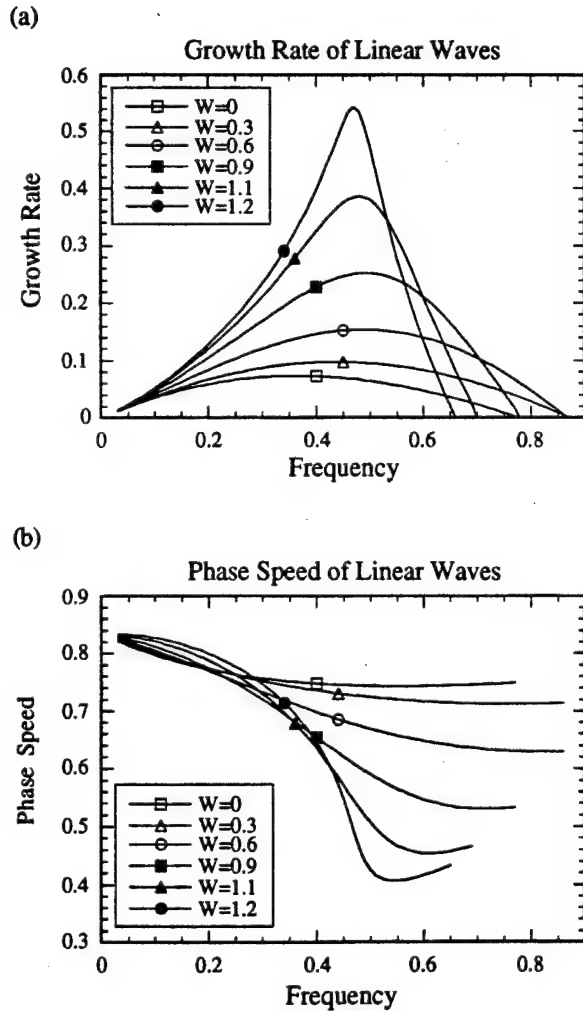
(a)

(b)

Figure 4. The growth rate (a) and phase speed (b) of spatially growing linear instability waves of a parallel shear flow with base velocity profile that described by Eq.(10). Curves for different values of the wake parameter W are indicated. The particular cases shown correspond to those of Fig.2.

The particular choice in the value of the thickness of the inlet velocity profiles noted above is motivated by the stability characteristics of the flow. Equation (10) indicates that the velocity profile chosen is essentially an errorfunction profile with a Gaussian wake deficit component. Stability analysis of a flow using this profile as a base profile indicates that the wake component alters the stability characteristics from that of the plain errorfunction profile in a non-trivial way. First, it introduces a second instability mode, the 'varicose' or 'wake' mode, to the single mode of the errorfunction, i.e. the 'sinus' or 'shear layer' mode [10-13]. It is found, however, that under most conditions the sinus mode still dominates. Second, it amplifies the growth of the sinus mode. This is shown in Fig.4 which displays the spatial growth rate (a) and phase speed (b) of this mode as a function of the wake strength, W, for the non-reacting uniform density flow. The cases displayed correspond to the velocity profiles of Fig.2. Clearly the magnitude of the growth-rate of the instability is highly sensitive to the wake strength W, increasing with increasing values of this parameter. The most unstable frequency of the flow, on the other hand, does not seem to be strongly dependent on W. The phase speed of the instability waves is also strongly modified by the wake, decreasing with increasing the wake deficit, particularly so around the most unstable frequency. This implies that the wavelength of the most unstable mode also changes significantly. For the profiles considered here, i.e. where $W = 0.0$ and 1.1 the corresponding most unstable wavelengths are $\Lambda_E = 12.8\sigma_\omega$ and $\Lambda_W = 6.5\sigma_\omega$. That is, the wavelength of the unstable waves arising from the wake-modified profile is approximately half of that of the errorfunction profile.

Simulations of shear layers with errorfunction inlet profiles indicate that the wavelength of the linear waves remains approximately constant as the flow develops into the non-linear stage, i.e. it is indicative of the size of the first generation eddies [15]. Thus, one would expect the eddies of the wake-modified profile to be about half the size of those of the errorfunction. The choice of σ for the errorfunction profile noted earlier is such that two such eddies fit inside the channel height. This is done with the aim that a paired eddy may be accommodated in the channel. In contrast, for the wake-modified case this implies that the channel may fit about four eddies. This argument also implies that with half the domain length in the case of the wake-modified flow similar number of eddies may be captured. For this reason, and with the aim of limiting the computational cost, in the simulations the length of the domain was varied between $X_{max} = 8$ and 4 for the errorfunction and the wake-modified inlet profiles, respectively.

Initialization of the calculation is carried out by assuming that the inlet conditions persist throughout the domain. Hence, transport elements are distributed over nine flat material layers (lines) lying within the region of finite vorticity and λ-gradient defined by the above profiles. The elements are of square area of side $h=0.0195$. The value of the core radius is $\delta=0.0234$, i.e. $h/\delta=0.833$. The time-step in all simulations was $\Delta t = 0.1$.

V. RESULTS AND DISCUSSION

The main objective of this paper lies in analyzing the effects of the presence of the splitter plate related wake component in the mean velocity profile on the flow dynamics in the case where exothermic combustion is present. To achieve this, simulations at a fixed Reynolds and Peclet number, $Re = Pe = 12800$, with and without combustion exothermicity, $Q_o = 0$ and 6, were carried out for both the errorfunction and the wake-modified inlet condition flows.

Instantaneous visualizations of both the errorfunction and the wake-modified simulation results in terms of the vorticity and product mass fraction are shown in Figs. 5 and 6, respectively. Parts (a) and (b) of each figure display the errorfunction inlet profile flow. In part (a) the entire computational domain is shown (i.e. $X_{max} = 8$) while in part (b) a domain equal in size to that of the wake-modified flow is presented (i.e. $X_{max} = 4$) - note that the size of this domain is also indicated in part (a). Part (c) displays the wake-modified inlet condition flow results. Each part compares the $Q_o = 0$ (top) with the $Q_o = 6$ (bottom) cases. The locus of the reaction interface is indicated in all visualizations by a dark line.

V.1 Overall Features

Figures 5 and 6 show that there are differences as well as similarities between the errorfunction and wake-modified flows. Two major conclusions: (i) The wake-modified flow gets destabilized earlier and more vigorously than its errorfunction counterpart. This is in agreement with the stability analysis results of the previous section. As a result, the convolution of the reaction interface is much more significant for the wake-modified flow and the resulting burning is clearly enhanced. (ii) For both the errorfunction and wake-modified flow, exothermicity tends to delay the destabilization of the flow and the intensity of the rollup.

Both conclusions are confirmed by the mean flow results shown in Fig.7, where the growth of the mean shear region (a) and of the product integral (b), for both the errorfunction and the wake-modified flows, are depicted. The shear region is based on the streamwise evolution of the mean velocity profile. It is defined as the distance between the points of the profile where the velocity first deviates by 0.01(1% of U_1) from the value of the neighboring free stream. The product integral is defined as $I_p = \int_o^1 Y_p \, dy$. It is clear that the shear region and the amount of product formed are substantially diminished when the errorfunction inlet profile is used. It is also seen that for both the errorfunction and wake-modified flows, exothermicity reduces the amount of product formed over most of the domain. A similar conclusion cannot be drawn for the mean shear region, however, particularly in the case of the wake-modified flow which exhibits a more complex behavior. As will be clarified in what follows this is because, unlike the

errorfunction case, in the wake-modified case the shear and mixing regions do not always coincide.

(a)

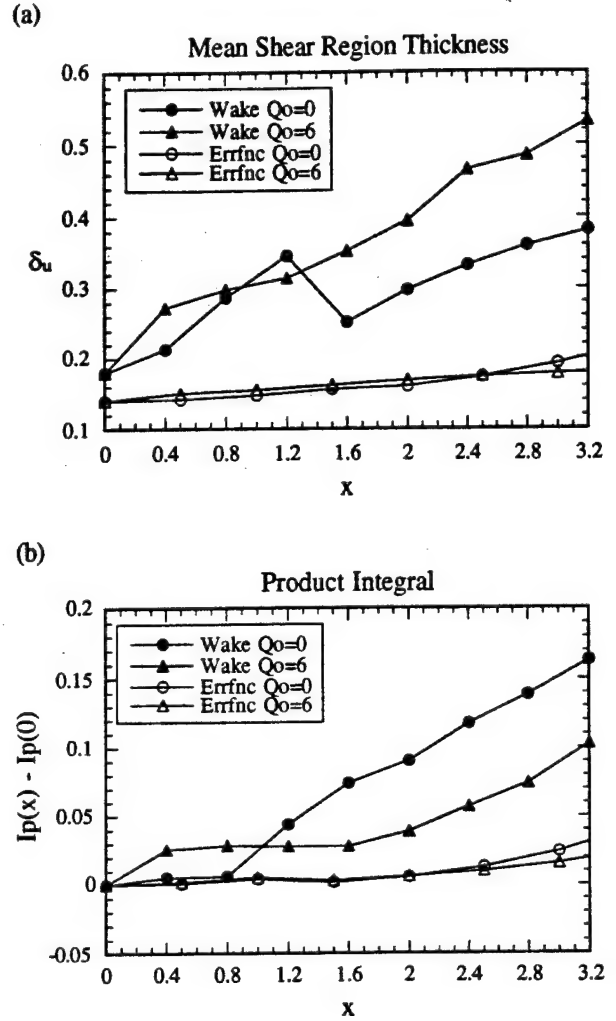Mean Shear Region Thickness

(b)

Product Integral

Figure 7. The mean shear region (a) and the product integral (b) the errorfunction and wake-modified flows with and without combustion exothermicity.

V.2 Detailed features

The instantaneous realizations shown in Figs. 5 and 6 can be used to answer several important questions relating to the mechanisms by which the reduction in the

Figure 5. (Figure on opposite page) Instantaneous vorticity distributions for the errorfunction (a-b) and the wake-modified (c) flows. Part (a) displays the entire errorfunction flow computational domain while part (b) concentrates on a section equal in size to the domain of the wake-modified flow. Each part of the figure contrasts the $Q_o = 0$ (top) and $Q_o = 6$ (bottom) cases. In all cases the locus of the reaction interface is indicated (black line).

6
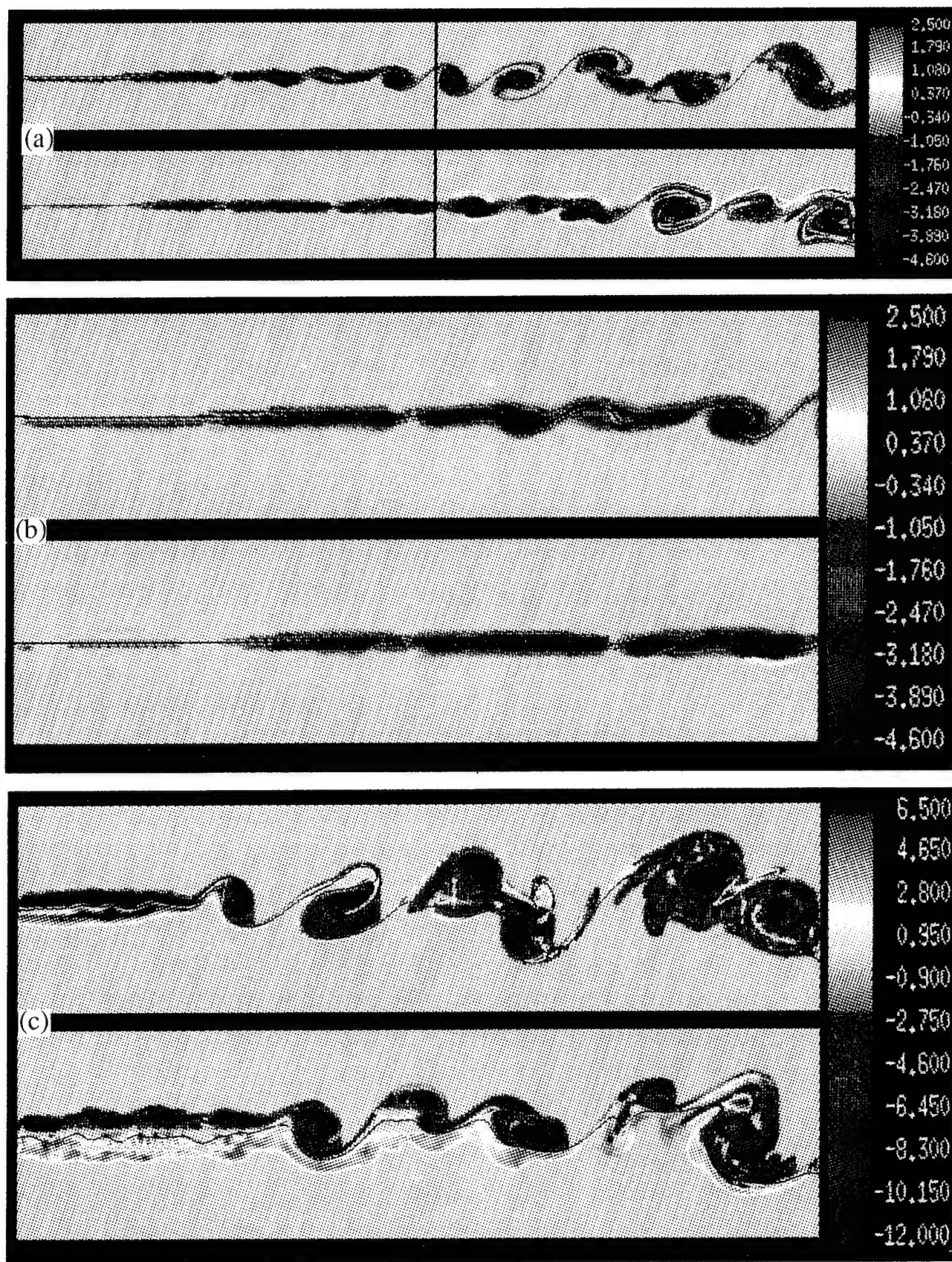
Figure 5. Caption on opposite page

Figure 6. Caption on following page

Figure 6. (Figure on previous page) Instantaneous product mass-fraction distri-butions for the errorfunction (a-b) and wake-modified (c) flows. The distributions depicted correspond to those of the vorticity of Fig.5. Part (a) displays the whole errorfunction flow computational domain while part (b) concentrates on a section equal in size to the domain of the wake-modified flow. Each part of the figure contrasts the $Q_o = 0$ (top) and $Q_o = 6$ (bottom) cases. In all cases the locus of the reaction interface is indicated (black line).
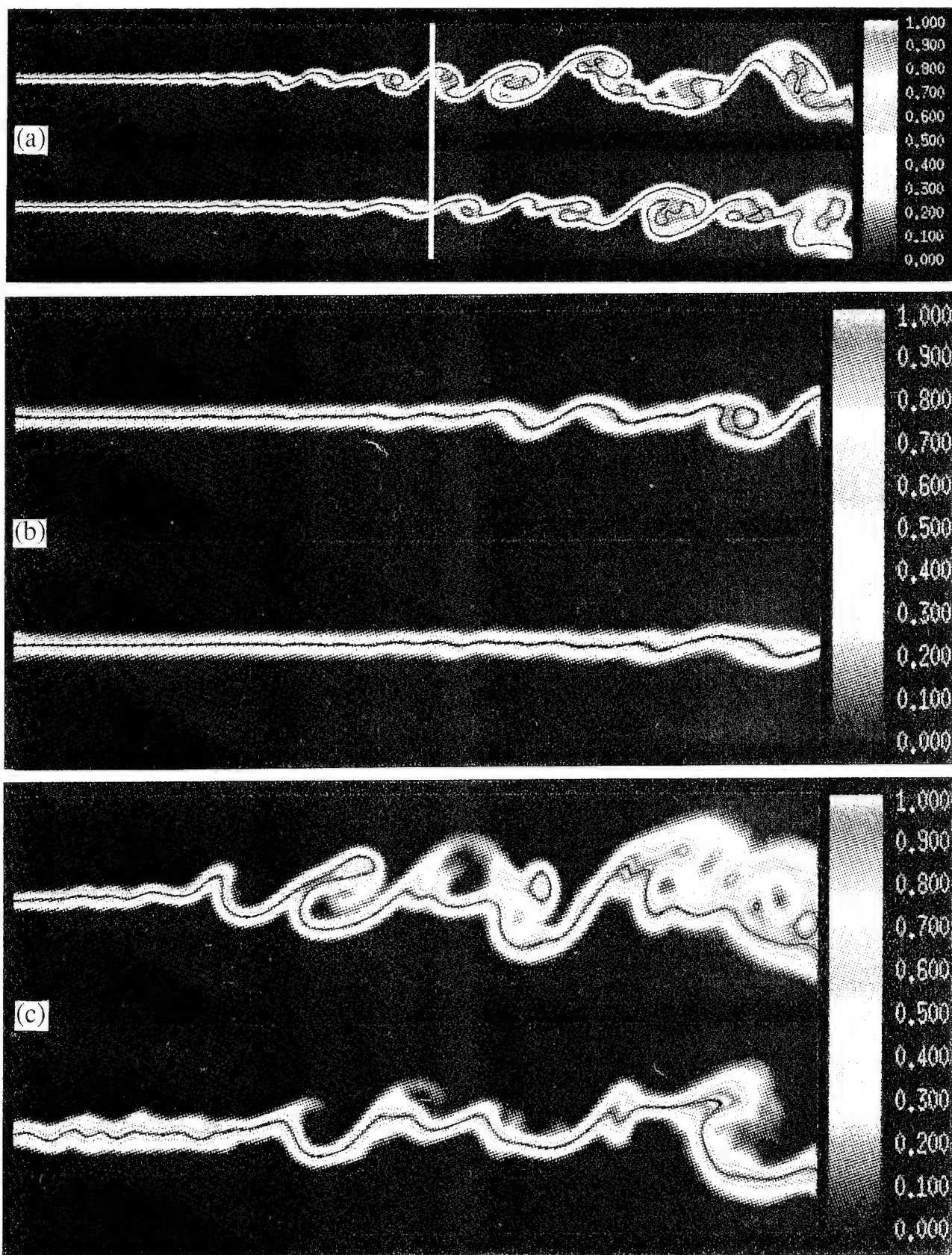
burning due to combustion exothermicity comes about in the two flows. For instance, can one claim that the only difference between the wake-modified and errorfunction cases is the one related to the streamwise location and the growth rate of the initial destabilization? And if that is the case, can the errorfunction flow be used as a good approximation of the wake-modified behavior via a spatial shifting or scaling? The figures indicate that this is clearly not true. The errorfunction and wake-modified flows exhibit differences in their evolution of fundamental nature. Examples of these are the origin and locus of the positive (conterclockwise rotating) vorticity and the relative location of the reaction interface with respect to the vortical structures.

V.2.1.The non-exothermic, uniform density flow

The vorticity field

Even in the absence combustion exothermicity and of the associated density variation, the evolution of the wake-modified flow exhibits important differences from the errorfunction flow. When the density is uniform, the vorticity of a fluid element may change only via diffusion. As a result, its sign cannot change. Thus, the sign of the vorticity field in the non-exothermic flow is uniquely determined by the inlet condition. For the errorfunction flow, where the inlet velocity profile is monotonic, the inlet vorticity is of a single sign, namely negative (top stream faster). Hence the vorticity of the downstream field is also always negative. In contrast, for the wake-modified flow the non-monotonicity of the inlet profile, results in vorticity of both signs. These observations are evident in Fig.5 which also points to their significance to the downstream flow dynamics.

For the errorfunction case, the evolution of the flow is manifested through the destabilization and convolution of a single sign vorticity layer which leads to the formation of a series of vortical structures. For the wake-modified case, on the other hand, the flow evolves through the interaction of two vorticity layers of opposite signs. The negative vorticity layer is the stronger of the two and dominates the dynamics. As a result the destabilization of the flow leads to the formation of downstream vortical structures which exhibit substantial similarities to those of the errorfunction inlet profile flow. The positive vorticity is wrapped around the negative vorticity layer and is finally entrained inside the vortical

structures. Remnants of it survive far downstream in small regions of counter-rotating flow which are very beneficial to the local mixing but whose effect on the large scale dynamics is secondary. The downstream similarity of the errorfunction and wake-modified flowfields in the uniform density case is also evident in the analysis of the mean flow. Mean velocity profiles of the wake-modified flow, shown in Fig.8 (top) indicate that within 1.6 channel heights downstream the wake deficit has been annihilated and the velocity profile has been altered to an errorfunction profile, the characteristic downstream profile of the errorfunction flow. Thus the 'wake region', i.e. the region where the mean flow experiences large scale wake features is rather small. The results of Fig.8 (top) also provide an explanation for the nonmonotonic behavior of the shear region shown in Fig.7a. Evidently the drop around $1.2 < x < 1.6$ is related to the elimination of the wake region and the transformation of the mean velocity profile to an errorfunction.

The reacting field

The initial location of the reaction interface with respect to the vorticity layers is crucial to the evolution of the reacting field. This fundamentally distinguishes the errorfunction and wake-modified flows. In the former, the reaction interface is initially located at the center of the single sign vorticity layer, that is, it coincides with the surface of maximum (magnitude-wise) vorticity. As this layer gets destabilized it stretches the interface and augments the burning. This behavior continues further downstream where the instability of the layer evolves into its non-linear stages and vortical structures form. In contrast, when the wake-modified inlet profile is used, the reaction interface is located between the two opposite sign vorticity layers. As the flow develops essentially through the destabilization of the negative vorticity layer, the interface is wrapped around this layer rather than being inside it. This arrangement implies that the shear and mixing regions of the flow do not coincide initially. This can clearly be seen in the first two vortical structures of the $Qo = 0$ wake-modified flow in Figs. 5 and 6 (parts(c), top) where large regions of shear do not mix reactants but consist primarily of the reactant carried by the fast stream. It is only further downstream, where neighboring vortical structures pair, that the reaction interface is moved towards the center of the shear region and its evolution resembles that of the errorfunction inlet profile flow.

The impact of these differences between the errorfunction and the wake modified flows on the burning can clearly be assessed through the mean shear region and product integral plots of Fig.7. For the errorfunction flow, the rise in the amount of product formed is closely related to the destabilization of the flow and the growth of the shear region. For the wake-modified flow, on the other hand, the shear region and the product integral do not correlate initially. Close to the inlet, growth of the shear region does not translate to more product. Rather the rate of product formation (judged by the slope of the product integral curve) is substantially increased around the region where the vorticity layer starts wrapping the reaction
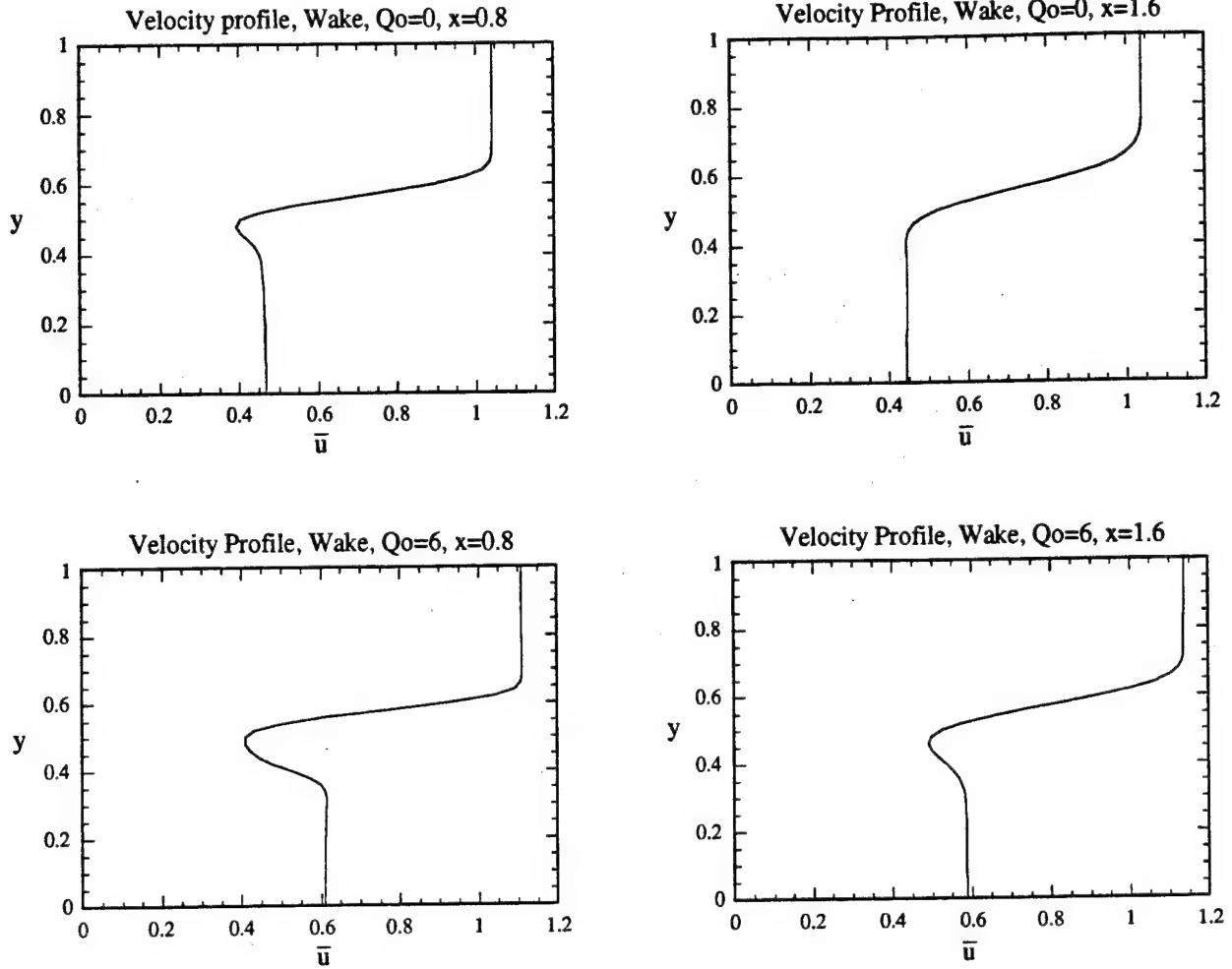
9

Figure 8. Mean velocity profiles of the wake-modified flow at two downstream locations, $x = 0.8$ (left) and $x = 1.6$ (right), for the $Q_o = 0$ (top) and $Q_o = 6$ (bottom) cases.

interface around it (note approximate location in Figs.5 and 6.). Furthermore, it continues at an approximately constant rate further downstream as the pairing maintains the mixing and burning at high levels. In contrast, the shear region experiences a drop at the early stages of this region of high burning. As was shown earlier this drop is related to the elimination of the wake region but here it may also serve as an additional example of the finite separation of the shear and mixing regions.

The relationship between the shear and mixing regions for the wake-modified and the errorfunction flow is further investigated in Fig.9 (top) and Fig.10 (top), respectively, which contrast mean product mass-fraction and turbulent kinetic energy profiles at two different downstream locations for the wake-modified and errorfunction flows, respectively. The turbulent kinetic energy is defined as $KE = 0.5\left(\overline{u'^2} + \overline{v'^2}\right)$. The figures clearly indicate that for the wake-modified flow, the cross-stream locations of the maxima of the kinetic energy and mass-fraction profiles are not the same. This

misalignment is reduced downstream where the negative vorticity layer mixes the reactants. The profiles corresponding to the errorfunction case, shown in Fig.10, on the other hand, do not experience any such misalignment in the profiles. This implies that in the wake-modified case turbulence does not necessarily lead to scalar mixing which is in agreement with earlier statements. As will shortly be seen this difference between the errorfunction and wake-modified flows has important ramifications when combustion exothermicity is present.

V.2.2. The exothermic, variable density flow

The differences between the errorfunction and the wake-modified flows are even more substantial in the reacting case. This is mainly a consequence of the difference in the location of the reaction interface with respect to the vorticity field and the resulting displacement of the shear and mixing regions noted above. That the over all effect of exothermicity on the
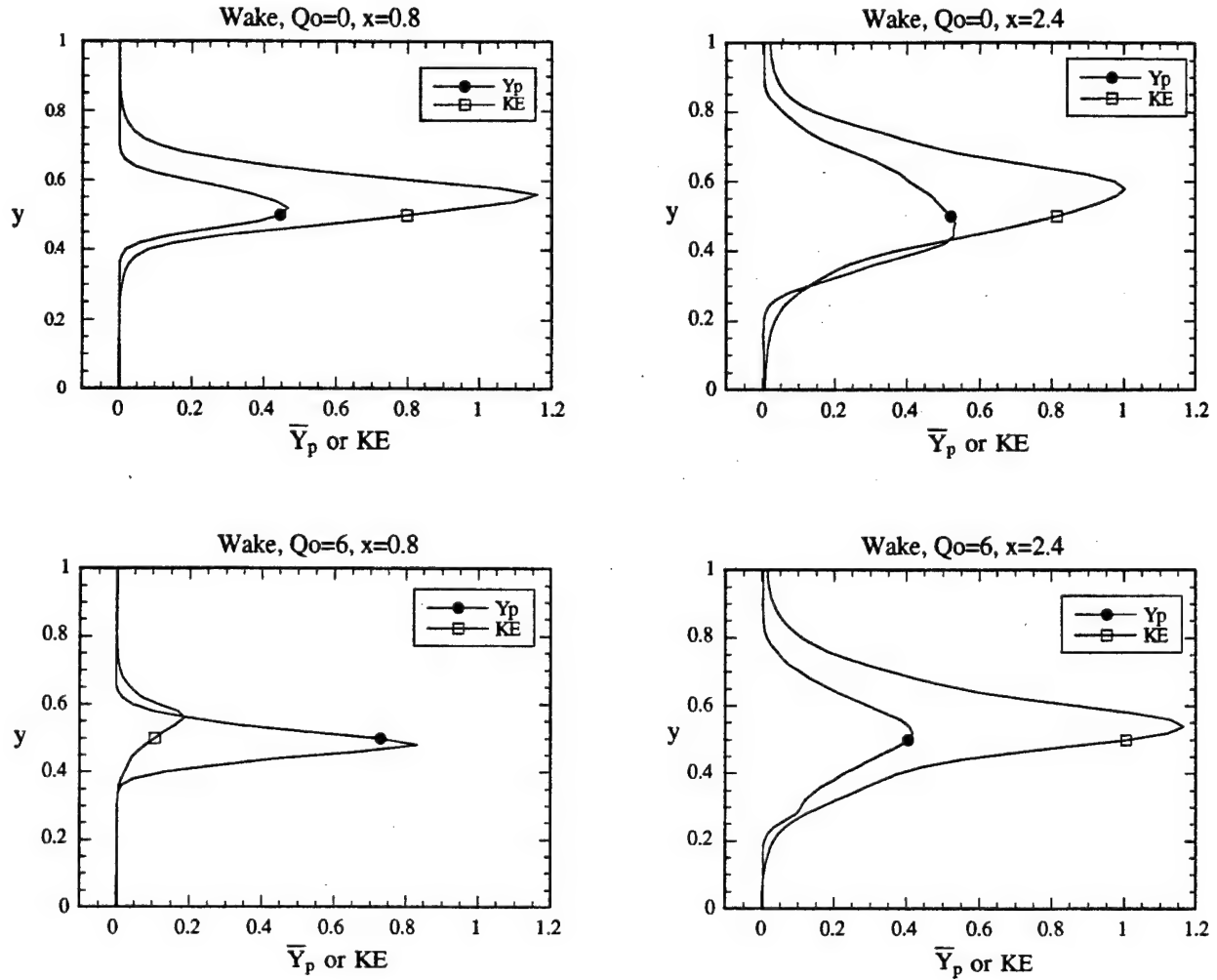
10

Figure 9. Mean product mass-fraction and turbulent kinetic energy profiles of the wake-modified flow at two downstream locations, $x = 0.8$ (left) and $x = 2.4$ (right), for the $Q_o = 0$ (top) and $Q_o = 6$ (bottom) cases.

mean product formation is similar (i.e. reduced in both cases) is in fact a result of different mechanisms.

The errorfunction flow

In the errorfunction case the deposition of energy and, hence, the creation of volume, takes place at the center of the negative vorticity layer where the vorticity magnitude is maximum. As a result this also becomes the region of minimum density. This coincidence of the vorticity, density-gradient and volumetric expansion fields has important implications on the dynamics of the flow. The reader is referred to Refs.[4, 6] where detailed discussions of the vorticity dynamics of a similar flow are presented. Essentially the vorticity field is modified by two major mechanisms; volumetric expansion and baroclinic generation (see Eq.(3)). The first expands the area and proportionately decreases the vorticity to preserve the circulation. Consequently, this mechanism

does not alter the vorticity sign. By thickening the vorticity layer, however, it delays the destabilization of the flow. Furthermore, by weakening the vorticity it results in downstream eddies with smaller rotation rates than those of the uniform density flow. Both the delay in the onset of the instability and the weakening of the vorticity are major reasons for the reduction of the shear region and the related (see earlier comments) reduction in the product integral seen in Fig.7.

The baroclinic generation term is strongly directional and modifies the vorticity of the fluid in regions where the pressure-gradient (or equivalently the fluid acceleration) and the density-gradient vectors are misaligned. The contribution of this term tends to improve the mixing within individual vortical structures but, at the same time, to inhibit their large scale interactions. This is because this term is the origin of the positive vorticity surrounding the errorfunction flow
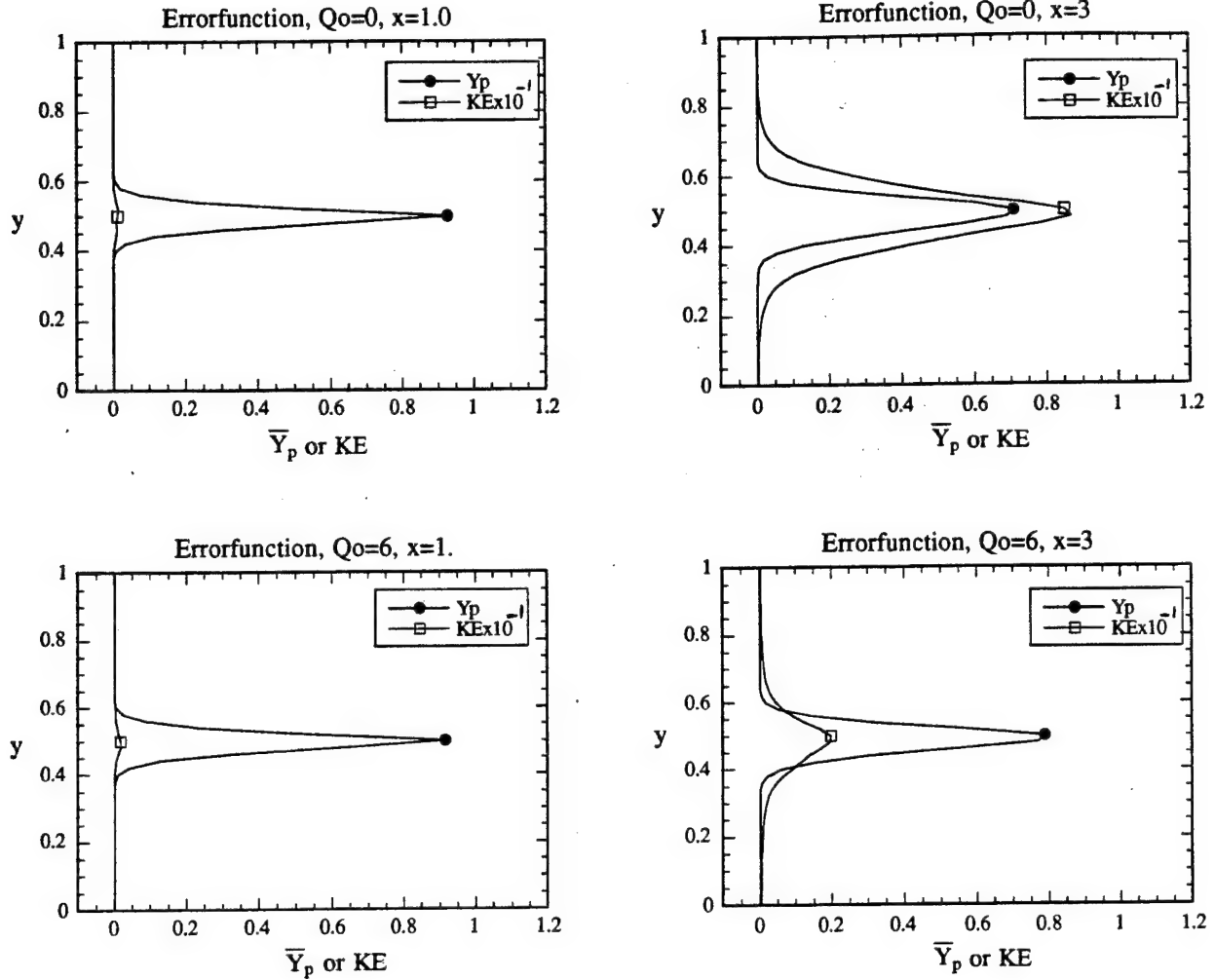
11

Figure 10. Mean product mass-fraction and turbulent kinetic energy profiles of the errorfunction flow at two downstream locations, $x = 1.0$ (left) and $x = 3.0$ (right), for the $Q_o = 0$ (top) and $Q_o = 6$ (bottom) cases.

eddies seen in Fig.5a(bottom) which resists the clockwise pairing interaction of neighboring structures imposed by the free-stream velocity ratio. The inhibition of pairing is another reason for the reduction in the mixing and burning in the errorfunction flow.

The wake-modified flow

In the wake-modified case the dynamics are quite different. Due to the location of the reaction interface the deposition of energy takes place between the two opposite sign vorticity layers, i.e. it does not coincide with the region where vorticity is quantitatively most significant. There are two major consequences of this: (i) The interaction of two vorticity layers is delayed as compared to that of the non-exothermic wake-modified flow, and (ii) the direct effects of volumetric expansion and baroclinic generation on the vorticity dynamics are substantially diminished as compared to those in the

exothermic errorfunction flow. These points are elaborated upon in what follows.

The creation of volume between the two vorticity layers pushes them away from one another and from the reaction interface. As a result, their interaction is delayed. This delay must also be, to some extend, due to the weakening of the vorticity due to the expansion. Both of these effects are evident in Fig.5c. For the exothermic case the interaction of the two layers, i.e. the entrainment of the positive vorticity layer by the negative vorticity layer, is substantially delayed. The motion of the layers away from one another close to the inlet and the decay in the magnitude of the vorticity there, are also clear. The delayed interaction of the two vorticity layers essentially implies that the wake region survives further downstream. This can be verified by the mean velocity profiles of Fig.8 and by the corresponding size of the mean shear region of Fig.7a. The former indicate that the wake component of

12

the mean velocity profile survives further downstream in the exothermic case. The latter further clarifies that for the exothermic case the wake region does not totally get eliminated within the computational domain.

Earlier comments on the importance of the early interaction of the two vorticity layers to combustion indicate the significance of its delay in the exothermic case. A reduction of mixing and burning is to be expected, and this was seen in the product integral plots of Fig.7b. The instantaneous flow visualizations help provide a detailed understanding of how this comes about. The lack of interaction between the two vorticity layers leads to their rather independent initial development. This is particularly true of the stronger, negative vorticity layer, which rolls very much like its errorfunction counterpart. As in the non-exothermic wake-modified flow, however, its effect on the reacting field is fundamentally different from the errorfunction flow since the reaction interface is no longer located inside the negative vorticity layer. In contrast to the uniform density wake-modified flow, its ability to convolute the reaction interface is diminished as the two are spaced further away from one another due to the intervening volumetric expansion filed. Thus, vortical structures grow and pair away from the flame which essentially remains flat (see Figs. 5 and 6). In other words, the shear mixing is initially irrelevant to combustion. It is only downstream, where the vortical structures become strong enough that they start wrapping the flame around them. Evidence of this can be seen in the growth rate of the product integral which experiences a sharp increase in its growth rate when convolution of the flame by the vorticity field finally takes place.

The mean product mass-fraction and turbulent kinetic energy profiles of Figs.9 and 10. further clarify these points. They indicate that in the early sections of the domain the displacement of the shear and mixing regions witnessed in the wake-modified flow (Fig.9) is enhanced in the presence of exothermicity. As in the non-exothermic flow this displacement is reduced downstream where the negative vorticity layer is able to effectively mix the reactants. In agreement with the non-exothermic case the errorfunction does not experience any such displacement of the shear and mixing regions.

In the wake-modified case, volumetric expansion occurs away from the area where the vorticity magnitude is large. This diminishes its effect on the vorticity field. As a result, both of the important consequences of the presence of volumetric expansion on the errorfunction flow, i.e. the delay in the onset of the instability and the formation of weaker eddies are not as important in the wake-modified flow. The instantaneous visualizations indicate that the destabilization of the flow takes place at about the same streamwise location for all the wake-modified flow simulations. The effect of exothermicity is restricted to a somewhat lower growth rate of the destabilizing perturbation. As was already pointed out, the reduction in the burning in this case is more closely related to the lack of convolution of the reaction interface rather than to a delay of the roll-up of the vorticity layer itself. As long as the vorticity layer rolls, sooner or later it will wrap the flame around it and enhance the burning.

This implies that the wake-modified flow is much more resistant to the negative impact of combustion exothermicity than the errorfunction. (Note that the specification of thicker inlet scalar profiles for the errorfunction than for the wake-modified inlet condition - see Section IV- implies that the difference between the errorfunction and wake-modified flows on the issue of instability suppression in the results presented here is actually underestimated).

The displacement of the initial vorticity with respect to the variable density regions for the wake-modified flow also diminishes the contribution of the baroclinic vorticity generation term as compared to that of the errorfunction flow. In the latter, this mechanism resulted in the appearance of positive vorticity around the vortical structures. The locus of the positive vorticity in the visualizations of the wake-modified flow shown in Fig.5c, on the other hand, implies that this vorticity is a result of the inlet condition and not of generation. The negative vorticity layer of the wake-modified flow which rolls like a uniform density errorfunction does not experience any regions of positive vorticity.

VI. CONCLUSIONS

Results of two-dimensional numerical simulations of spatially-developing shear layers reacting at an infinite rate indicate that the presence of a wake deficit in the inlet velocity profile modifies the downstream dynamics in such a way that mixing and burning are increased. Combustion exothermicity reduces the burning in this flow. While a similar trend is experienced in the flow arising from a monotonically varying inlet profile, in this case an errorfunction, the mechanisms by which this is achieved in the two flows are different.

Linear stability analysis of the uniform density flow indicates that the flow arising from the wake-modified profile is much more unstable than that from the errorfunction. This result is confirmed by the numerical simulations, which also indicate that the stronger instability of the wake-modified flow translates to better mixing and increased burning.

Beyond stability characteristics, the most important differences in the behavior of the errorfunction and wake-modified flows arise due to the relative location of the reaction interface with respect to the vorticity field. In the errorfunction flow the reaction interface is located at the center of a single, negative vorticity layer, and gets highly convoluted by it. For the wake-modified flow the reaction interface is located between two vorticity layers of opposite signs. The negative layer, which dominates, convolutes the interface by wrapping it around itself.

The difference in the location of the reaction interface with respect to the negative vorticity layer between the errorfunction and wake-modified flows has the following important consequences: (i) The shear and mixing regions do not always coincide in the wake-modified flow as they do in the errorfunction. (ii) In the wake-modified flow exothermicity decreases the product

13

formation through a delay in the convolution of the reaction interface by the negative vorticity layer as volumetric expansion pushes the two away from one another. In the errorfunction flow the reduction comes about by the weakening of the vorticity field by volumetric expansion. (iii) The wake-modified case is much more resistant to the exothermicity related instability suppression than the errorfunction case. This is because volumetric expansion takes place away from the regions where the vorticity is most significant. (iv) The interaction of the two vorticity layers of the wake-modified case is delayed in the exothermic case. As a result the size of the region is enlarged in this case.

REFERENCES

1. Riley, J.J., Metcalfe, R.W. and Orszag, S.A., "Direct Numerical Simulations of Chemically Reacting Turbulent Mixing Layers," *Phys. Fluids*, **29**, pp.406-422, 1986.

2. Givi, P. and Jou, W.H., "Direct Numerical Simulations of a Two-Dimensional Reacting, Spatially Developing Mixing Layer by a Spectral-Element Method," *22nd Symposium (International) on Combustion*, The Combustion Institute, Pittsburgh PA, pp. 635-643, 1988.

3. Ghoniem, A.F. and Heidarinejad, G., "Effect of Damkohler Number on the Reactive Zone Structure in a Shear Layer," *Combustion and Flame*, **83**, pp.1-16, 1991.

4. McMurtry, P.A., Riley, J.J. and Metcalfe, R.W., "Effects of Heat Release on the Large-Scale Structure in Turbulent Mixing Layers," *J. of Fluid Mech.*, **199**, pp.297-332, 1989.

5. Grinstein, F.F and Kailasanath, K., "Chemical Energy Release and Dynamics of Transitional, Reactive Shear Flows," *Phys. Fluids*, A **4**, pp.2207-2221, 1992.

6. Soteriou, M.C. and Ghoniem, A.F., "The Vorticity Dynamics of an Exothermic Spatially Developing, Forced, Reacting Shear Layer," *25th Symposium (International) on Combustion*, The Combustion Institute, 1994. (in press).

7. Brown, G.L. and Roshko, A., "On Density Effects and Large Structure in Turbulent Mixing Layers," *J. Fluid Mech.*, **64**, pp.775-816, 1974.

8. Dimotakis, P.E., "Turbulent Free Shear Mixing," AIAA Paper 89-0262, 1989, also "Turbulent Free Shear Mixing and Combustion," GALCIT Report FM91-2, 1991

9. Dimotakis, P.E. and Brown, G.L., "The Mixing Layer at High Reynolds Number: Large-Structure Dynamics and Entrainment," J. Fluid Mech., **78**, pp.535-560, 1976.

10. Koochesfahani, M.M., and Frieler, C.E., "Instability of Nonuniform Density Free Shear Layers with a Wake Profile", *AIAA J.*, **27**, pp.1735-1740, 1989.

11. Knio, O.M. and Ghoniem, A.F., "Stability Analysis of Differentially-Heated Asymmetric Vorticity Layers," J.T. Beale et al. (eds.), *Vortex Flows and Related Numerical Methods*, pp.341-372, 1993

12. Marasli, B., Champagne, F.H. and Wygnaski, I.J., "Modal decomposition of velocity signals in a plane turbulent wake," *J.Fluid Mech.*, **198**, pp.255-273, 1989.

13. Yu M-H and Monkewitz, P.A., "The effect of Nonuniform Density on the Absolute Instability of Two-Dimensional Inerial Jets and Wakes," *Phys. Fluids* A **2** (7), pp.1175-1181, 1990.

14. Ashurst, W.T., "Numerical Simulation of Turbulent Mixing Layers via Vortex Dynamics," Durst et al. (eds.), *Turbulent Shear Flows*, **1**, pp.402-413, Springer-Verlag, Berlin, 1979.

15. Soteriou, M.C. and Ghoniem, A.F. "Manipulation of the Growth Rate of a Variable Density Spatially Developing Mixing Layer via External Modulation," AIAA-91-0081 paper, 1991.

16. Soteriou, M.C. and Ghoniem, A.F., "On the Application of the Infinite Reaction Rate Model in the Simulation of the Dynamics of Exothermic Mixing Layers," *Comb. Sci. and Tech.*, 1994. (in press).

17. Soteriou, M.C. and Ghoniem, A.F. "Dynamics of Reacting Shear Flows; Effects of Exothermicity and Forcing," AIAA-94-0777 paper, 1994.

APPENDIX II

AIAA 95 - 0380

An Unsteady Strained Flame Model with Multi-Step Chemical Kinetics for Turbulent Combustion Simulations

C. A. Petrov and A.F. Ghoniem
Massachusetts Institute of Technology
Cambridge, MA 02139

33rd Aerospace Sciences Meeting and Exhibit
January 9-12, 1995 / Reno, NV

An Unsteady Strained Flame Model with Multi-Step Chemical Kinetics for Turbulent Combustion Simulations

Constantin A. Petrov[1] and Ahmed F. Ghoniem[2]
Massachusetts Institute of Technology
Cambridge, MA 02139

ABSTRACT

The objectives of this work are to develop a combustion submodel for high Damkohler number turbulent combustion simulation, and to investigate the transient dynamics of strained flame. A series of mathematical transformations are used, under the assumption that the applied strain rate is constant throughout the flame structure, to translate the system of equations governing flame propagation in an unsteady stagnation point flow into a set of reaction-diffusion equations. Combustion is described by a multi-step chemical kinetics mechanism. The flame structure computed using this model is compared with the "exact" numerical solutions obtained for unstrained and highly strained stoichiometric, atmospheric pressure, methane-air flames. In the case of an unstrained flame, our model predictions agree very well with the exact solution. In the case of a highly strained flame, the temperature and major species profiles are well predicted, while the minor species (radicals) on the products side are overpredicted. The transient dynamics of lean and stoichiometric flames are investigated by exposing the flame to a sudden change in strain. For a given value of strain, we find that the stoichiometric flame, which has the highest heat release rate, has the smallest response time. As the mixture becomes leaner, the heat release rate drops causing the flame response time to increase. For a given equivalence ratio, the response time first increases with strain reaching a maximum at approximately 700 1/s, then monotonically decreases. For strains lower than 700 1/s, the flame is convected by the flow while its structure remains almost unchanged and the flame dynamics are governed by the flame thermal-diffusion time scale which increases with equivalence ratio. For strains higher than 1000 1/s, when the influence of the flow on the flame structure is dominant, the flow time scale determines the flame dynamics and makes it independent of the equivalence ratio. The results show that for turbulent combustion simulation, the assumption of instantaneous flame response to strain is accurate only for near-stoichiometric flames .

1 Graduate Research Assistant
2 Professor, Associate Fellow, AIAA

1. INTRODUCTION

Numerical modeling and simulation of turbulent combustion in premixed gases, at conditions when the flame thickness is smaller than the smallest turbulent eddies, have adopted the flamelet and thin flame approaches, respectively. In both approaches, turbulence, while weakly changing the internal structure of the flame and thus its burning velocity, extends its overall surface area and thus substantially increases the overall burning rate per unit volume. This is reasonable when the turbulence intensity, as measured by, e.g., the square root of the total kinetic energy of the fluctuating field, is weak relative to the burning velocity. As the intensity increases, local flow gradients become comparable with the gradients across the flame and turbulence induced strain rates alter the flame structures in non trivial ways. These effects are the subject of this paper.

In our previous paper on this subject [1], we investigated the effect of the Lewis number and the heat release rate on the flame response to a sudden change in the strain rate and to an oscillating strain using a "uniform" strain model. We have shown that both the heat release and the deviation of the Lewis number from unity can have

profound effects on the flame dynamics. A simple one-step chemical mechanism and constant thermodynamic properties were used in these studies. While providing insight into the mechanisms governing the flame dynamics, that model is not capable of predicting the dynamics of real hydrocarbon-air flames due to the simplicity of the chemical kinetics and transport mechanisms utilized.

The objectives of this work are to investigate the performance of our model when used in situations where multi-step kinetics are important, and to determine the flame response time when unsteady perturbations are imposed. We show that our model, which makes the simplification that the strain rate is constant throughout the flame structure, predicts accurately the flame structure in terms of the major species, over a wide range of strain rates. This simplification allows one to transform the governing equations into reaction-diffusion equations and thus reduces the computational effort required to obtain the solution, especially in the unsteady case. We also find that the response time of the flame is a strong function of the heat release rate and the applied strain.

This paper represents a logical application of the approach developed in [1] to flames described by the multi-step chemical kinetics. The problem of flame propagation in mixtures with a multi-step kinetics mechanism has been studied before using different models (see, for example, [2], [5], [7], [8]-[12] among others). Most of these studies assume steady flames and, thus, may not be applicable as sub-models in a turbulent combustion simulation in situations when the dynamics of flame-flow interactions are important. As we showed in our previous studies [1], [13], flame response to unsteady perturbation can have a significant impact on the burning rate, extinction and combustion instability.

The paper is organized as follows. In Section 2, the unsteady problem is formulated and the solution procedure is described. Section 3 deals with the numerical aspects of the problem. In Section 4, we discuss the results of the calculations, compare the model with two exact numerical solutions for the cases of unstrained and strained flames and show the effect of a step-wise variation in the strain on the response time at different equivalence ratios. Section 5 contains the conclusions.

2.1 FORMULATION

The flow configuration is depicted in figure 1. The flame is located in the stagnation point flow produced by two counter-flowing planar jets of reactants and products. The x- and y-axes are directed parallel and perpendicular to the flame, respectively. The flame is, in general, unsteady, i.e. its location and burning velocity change with time due to changes in the flow field, species concentration or the temperature.

Applying the boundary layer approximation, in which diffusion along the boundary layer, taken here to be the x-axis, is negligibly small, we write the equations governing the flame structure as follows:

$$\frac{\partial \rho}{\partial t} + \frac{\partial (\rho u)}{\partial x} + \frac{\partial (\rho v)}{\partial y} = 0 , \qquad (2.1)$$

$$\rho \frac{\partial Y_k}{\partial t} + \rho u \frac{\partial Y_k}{\partial x} + \rho v \frac{\partial Y_k}{\partial y} = - \frac{\partial}{\partial y} \left(\rho Y_k V_k \right) + \dot{\omega}_k W_k, \text{ for } k = 0, K \quad (2.2)$$

$$\rho c_p \left(\frac{\partial T}{\partial t} + u \frac{\partial T}{\partial x} + v \frac{\partial T}{\partial y} \right) = \frac{\partial}{\partial y} \left(\lambda \frac{\partial T}{\partial y} \right)$$
$$- \sum_{k=0}^{K} \rho Y_k V_k c_{p,k} \frac{\partial T}{\partial y} - \sum_{k=0}^{K} \dot{\omega}_k H_k , \quad (2.3)$$

$$p = \rho \frac{R_u}{W_{mix}} T , \qquad (2.4)$$

$$\rho \frac{\partial u}{\partial t} + \rho u \frac{\partial u}{\partial x} + \rho v \frac{\partial u}{\partial y} = - \frac{\partial p}{\partial x}, \qquad (2.5)$$

where ρ is the mixture density; u and v are the velocities of fluid in the x and y directions, respectively; Y_k is the mass fraction; D_k is the mixture averaged diffusion coefficient; $\dot{\omega}_k$ is the

2

production rate; W_k is the molecular weight; c_p and $c_{p,k}$ are the constant pressure specific heats of the mixture and individual species, respectively; $(K+1)$ is the total number of chemical species; T and p are the thermodynamic temperature and pressure, respectively; λ is the thermal conductivity of the mixture; R_u is the universal gas constant; W_{mix} is the molecular weight of the mixture; H_k is the enthalpy in molar units; and the diffusion velocity V_k is defined as follows:

$$V_k = -\frac{D_k}{X_k}\frac{\partial X_k}{\partial y} + V_{cor} + \frac{D_k\, k_{T,k}}{X_k}\frac{1}{T}\frac{\partial T}{\partial y},$$

$$for\ k = 0, K$$

where V_{cor} is the correction velocity introduced in order to satisfy the identity $\sum_{k=0}^{K} Y_k V_k = 0$; $k_{T,k}$ is the thermal diffusion coefficient. In the following, we neglect the thermal diffusion velocity (the last term of the above equation) and the correction velocity. As shown in [2], this simplification does not significantly affect the results. In the above equations, we neglected the diffusion terms in the x-momentum equation, and the heat and mass transport equations, and the dissipation term in the energy equation.

Along the stagnation streamline $x = 0$, and due to symmetry : $u = 0$, $\frac{\partial}{\partial x} = 0$, leading to the following simplifications of equations (2.1-5):

$$\frac{\partial \rho}{\partial t} + \rho\,\frac{\partial u}{\partial x} + \frac{\partial(\rho v)}{\partial y} = 0 \qquad (2.6)$$

$$\rho\,\frac{\partial Y_k}{\partial t} + \rho\, v\,\frac{\partial Y_k}{\partial y} = \frac{\partial}{\partial y}\left(\frac{\rho D_k}{W_{mix}}\frac{\partial(W_{mix} Y_k)}{\partial y}\right) +$$

$$\dot{\omega}_k\, W_k, k = 0, K \qquad (2.7)$$

$$\rho\, c_p\frac{\partial T}{\partial t} + \rho\, c_p v\,\frac{\partial T}{\partial y} = \frac{\partial}{\partial y}\left(\lambda\frac{\partial T}{\partial y}\right) -$$

$$\sum_{k=0}^{K}\rho Y_k V_k c_{p,k}\frac{\partial T}{\partial y} - \sum_{k=0}^{K}\dot{\omega}_k\, H_k \quad (2.8)$$

$$p = \rho\,\frac{R_u}{W_{mix}}\, T \ . \qquad (2.9)$$

while the x-momentum equation is redundant along the stagnation streamline. The latter simplification makes our model different from the models described in Refs. [2], [5], [7], [8] - [12], where the momentum equation is solved. The implication of not satisfying the momentum equation will become clear when we compare the model results with the exact solution.

The boundary conditions for equations (2.6-8) are:

$$y = -\infty\ :\ Y_k = Y_{k,b}\ ,\quad T = T_b\ ,\ \frac{\partial T}{\partial y} = 0 \quad (2.10)$$

$$y = +\infty\ :\ Y_k = Y_{k,u}\ ,\quad T = T_u \qquad (2.11)$$

where the subscripts u and b denote values on the unburnt and the burnt side, respectively. The boundary conditions for the velocity field will be discussed later. Although along the stagnation streamline $u = 0$, the $\partial u\,/\,\partial x$ term of equation (2.6) does not vanish. Since the boundary conditions for Y_k and T are independent of x, it can be demonstrated [1] that the flame structure near the stagnation streamline is similar to that described by equations (2.6-9).

One more simplification of the problem is made. The energy equation (2.8) contains a term in the form

$$\sum_{k=0}^{K}\rho Y_k V_k c_{p,k}\frac{\partial T}{\partial y}.$$

Smooke [2] showed that this term can be safely neglected virtually for all important configurations of strained and unstrained flames. Eliminating this term, equation (2.11) becomes:

$$\rho\, c_p\left(\frac{\partial T}{\partial t} + v\,\frac{\partial T}{\partial y}\right) = \frac{\partial}{\partial y}\left(\lambda\frac{\partial T}{\partial y}\right) - \sum_{k=0}^{K}\dot{\omega}_k\, H_k$$
$$(2.12)$$

3

The solution technique applied here to solve the system of equations (2.6-12) with boundary conditions (2.10-11) is identical to that used in our previous work [1]. Hence, we will describe it only briefly. First, we decompose the velocity field as follows:

$$\vec{v} = \vec{V} + \vec{v_c} \qquad (2.13)$$

where $\vec{v}$ is the total velocity, $\vec{v_c}$ is the combustion generated velocity, and $\vec{V}$ is the externally imposed velocity which satisfies the following incompressible continuity equation:

$$\frac{\partial U}{\partial x} + \frac{\partial V}{\partial y} = 0 \qquad (2.14)$$

Substituting equation (2.13) into continuity equation (2.6), using equation (2.14) and assuming that on the stagnation streamline $\partial u_c / \partial x = 0$, we obtain:

$$\frac{\partial \rho}{\partial t} + \frac{\partial(\rho v_c)}{\partial y} + V \frac{\partial \rho}{\partial y} = 0 \qquad (2.15)$$

Substitution the velocity decomposition in equation (2.13) into equations (2.7) and (2.12) yields:

$$\rho \frac{\partial Y_k}{\partial t} + \rho (V + v_c) \frac{\partial Y_k}{\partial y} = \frac{\partial}{\partial y}\left(\frac{\rho D_k}{W_{mix}} \frac{\partial(W_{mix} Y_k)}{\partial y}\right) + \dot{\omega}_k W_k, k = 0, K \qquad (2.16)$$

$$\rho c_p \frac{\partial T}{\partial t} + \rho c_p (V + v_c) \frac{\partial T}{\partial y} = \frac{\partial}{\partial y}\left(\lambda \frac{\partial T}{\partial y}\right) - \sum_{k=0}^{K} \dot{\omega}_k H_k \qquad (2.17)$$

Second, if the externally imposed inviscid irrotational velocity field $\vec{V}$ is specified as

$$\vec{V} = (\varepsilon(t) x, -\varepsilon(t) y) \qquad (2.18)$$

where ε is the strain rate, then the following transformation [3]

$$\tilde{y} = exp\left(\int_0^t \varepsilon(t') \, dt'\right) y \equiv B(t) y, \quad \tilde{t} = t \qquad (2.19)$$

eliminates the $V \, \partial/\partial y$ operators from equations (2.15-17). Following the application of the transformation in equation (2.19), the governing equations take the form:

$$\frac{\partial \rho}{\partial \tilde{t}} + B \frac{\partial(\rho v_c)}{\partial \tilde{y}} = 0, \qquad (2.20)$$

$$\rho \frac{\partial Y_k}{\partial \tilde{t}} + \rho \, v_c B \frac{\partial Y_k}{\partial \tilde{y}} = B^2 \frac{\partial}{\partial \tilde{y}}\left(\frac{\rho D_k}{W_{mix}} \frac{\partial(W_{mix} Y_k)}{\partial \tilde{y}}\right) + \dot{\omega}_k W_k, k = 0, K \qquad (2.21)$$

$$\rho \, c_p \frac{\partial T}{\partial \tilde{t}} + \rho \, c_p \, v_c B \frac{\partial T}{\partial \tilde{y}} = B^2 \frac{\partial}{\partial \tilde{y}}\left(\lambda \frac{\partial T}{\partial \tilde{y}}\right) - \sum_{k=0}^{K} \dot{\omega}_k H_k \qquad (2.22)$$

The combustion generated velocity $\vec{v_c}$ is eliminated by applying another (Howarth) transformation to equations (2.20-22):

$$\xi = \int_0^{\tilde{y}} \overline{\rho} \, d\tilde{y}' , \quad \tau = \tilde{t} , \qquad (2.23)$$

where the overbar denotes the density normalized by its value on the reactants side, ρ_u. To apply this transformation, we divide the continuity equation by ρ_u and integrate it to obtain:

$$\int_y^{\tilde{y}} \frac{\partial \overline{\rho}}{\partial \tilde{t}} \, d\tilde{y}' + B \, \overline{\rho}(\tilde{y}) \, v_c(\tilde{y}) - B \, \overline{\rho}(0) \, v_c(0) = 0 \qquad (2.24)$$

4

At the stagnation point $y = 0$ the total velocity must be zero. This requirement imposes the following boundary condition $v_c(0) = 0$ and equation (2.24) is reduced to:

$$\int_y^{\tilde{y}} \frac{\partial \overline{p}}{\partial t} d\tilde{y}' = -B \, \overline{\rho}(\tilde{y}) \, v_c(\tilde{y}) \qquad (2.25)$$

Mapping equations (2.21-22) onto the (ξ, τ) domain, and using the chain rule and equation (2.25), we get:

$$\rho \, \frac{\partial Y_k}{\partial \tau} = B^2 \overline{\rho} \, \frac{\partial}{\partial \xi} \left(\frac{\rho D_k}{W_{mix}} \overline{\rho} \, \frac{\partial (W_{mix} Y_k)}{\partial \xi} \right)$$
$$+ \, \dot{\omega}_k \, W_k \quad for \; k = 0, K \quad (2.26)$$

$$\rho \, c_p \frac{\partial T}{\partial \tau} = B^2 \, \overline{\rho} \, \frac{\partial}{\partial \xi} \left(\lambda \, \overline{\rho} \, \frac{\partial T}{\partial \xi} \right) - \sum_{k=0}^{K} \dot{\omega}_k \, H_k \quad (2.27)$$

Finally, equations (2.26-27) are non-dimensionalized using the length scale based on the thermal diffusion length $y_{scl} = \sqrt{\alpha_u \, t_{scl}}$, where α_u is the thermal diffusivity coefficient of the mixture on the reactants side, $t_{scl} = \alpha_u / S_u^2$, and S_u is the unstrained flame burning velocity. Introducing the non-dimensional temperature, $\theta = (T - T_u) / (T_b - T_u)$, we get:

$$\rho \, \frac{\partial Y_k}{\partial \overline{\tau}} = B^2 \overline{\rho} \, \frac{1}{\alpha_u} \frac{\partial}{\partial \overline{\xi}} \left(\frac{\rho D_k}{W_{mix}} \overline{\rho} \, \frac{\partial (W_{mix} Y_k)}{\partial \overline{\xi}} \right)$$
$$+ \, t_{scl} \, \dot{\omega}_k \, W_k \quad for \; k = 0, K \quad (2.28)$$

$$\rho \, c_p \frac{\partial \theta}{\partial \overline{\tau}} = B^2 \, \overline{\rho} \, \frac{1}{\alpha_u} \frac{\partial}{\partial \overline{\xi}} \left(\lambda \, \overline{\rho} \, \frac{\partial \theta}{\partial \overline{\xi}} \right) -$$
$$\frac{t_{scl}}{(T_b - T_u)} \sum_{k=0}^{K} \dot{\omega}_k \, H_k, \qquad (2.29)$$

where $\overline{\xi} = \xi / y_{scl}$, and $\overline{\tau} = \tau / t_{scl}$, and the boundary conditions are given by equations (2.10-11).

Next, we discuss the evaluation of the transport coefficients λ and D_k, $k = 1, K$. We used the SANDIA Transport [4] and Premixed Flame [5] codes to study the variation of these parameters with temperature. In accordance with Smooke [2], we found that the Lewis numbers $L_{e, k} = \lambda / (\rho \, c_p \, D_k)$ of all species in the stoichiometric, atmospheric pressure, methane/ air flame are almost constant with temperature. Therefore, in our calculations we used, the following values for the Lewis numbers:

Table 1. Constant Lewis Numbers of Different Species.

Species	Lewis Number
CH_4	0.97
O_2	1.11
H_2O	0.83
CO_2	1.39
H	0.18
O	0.70
OH	0.73
HO_2	1.10
H_2	0.30
CO	1.10
H_2O_2	1.12
HCO	1.27
CH_2O	1.28
CH_3	1.00
CH_2O	1.30
N_2	1.00

For an accurate simulation it is extremely important to have the correct dependence of the thermal conductivity coefficient on temperature. At the same time, its direct calculations using the collisions integrals could be computationally prohibitive. Using the SANDIA Transport code, we found that the interpolation for the thermal conductivity coefficient suggested by Smooke [2], $\lambda = 2.58 \; 10^{-4} c_p \, (T / T_u)^{0.7}$ (CGS units), produces results which are virtually identical to those obtained from the code over the entire range of temperature. Thus, this interpolation formula has been adopted in our model.

Using the assumption of constant Lewis number, $L_{e, k} = \lambda / (\rho \, c_p \, D_k) = const$, and the Smooke correlation $\lambda = 2.58 \; 10^{-4} c_p \, (T / T_u)^{0.7}$, we rewrite the diffusion terms in the governing equations (2.28-29). For the mass fraction equation:

5

$$\rho D_k \bar{\rho} = \frac{\lambda}{c_p \, L_{e,\,k}} \frac{\rho}{\rho_u} = \frac{1}{L_{e,\,k}} \frac{\lambda}{\lambda_u} \frac{c_{p,\,u}}{c_p} \frac{\rho}{\rho_u} \frac{\lambda_u}{c_{p,\,u}} =$$

$$\frac{1}{L_{e,\,k}} \frac{\lambda}{\lambda_u} \frac{c_{p,\,u}}{c_p} \rho \; \alpha_u \; , \quad (2.30)$$

where we used the definition of the thermal diffusivity coefficient, $\alpha_u = \lambda_u / \rho_u \, c_{p,\,u}$. For the energy equation:

$$\lambda \, \bar{\rho} = \lambda \, \frac{\rho}{\rho_u} = \lambda_u \frac{\lambda}{\lambda_u} \frac{\rho}{\rho_u} \frac{c_{p,\,u}}{c_{p,\,u}} = \alpha_u \rho \; c_{p,\,u} \frac{\lambda}{\lambda_u}$$

$$(2.31)$$

Using Smooke's correlation and the equation of state, we evaluate:

$$\frac{\lambda}{\lambda_u} \frac{c_{p,\,u}}{c_p} = \left[\frac{T}{T_u}\right]^{0.7} , \qquad \frac{\lambda}{\lambda_u} = \frac{c_p}{c_{p,\,u}} \left[\frac{T}{T_u}\right]^{0.7}$$

$$\frac{\rho}{\rho_u} = \frac{W_{mix}}{W_{mix,\,u}} \frac{T_u}{T} \qquad (2.32)$$

Dividing equations (2.28-29) by ρ and $\rho \, c_p$, respectively, and using equations (2.32), we obtain:

$$\frac{\partial Y_k}{\partial \bar{\tau}} = \frac{B^2}{L_{e,\,k}} \frac{\partial}{\partial \bar{\xi}} \left(\left[\frac{T}{T_u}\right]^{-0.3} \frac{\partial}{\partial \bar{\xi}} \left(\frac{W_{mix}}{W_{mix,\,u}} Y_k \right) \right) +$$

$$\frac{t_{scl} \, \dot{\omega}_k \, W_k}{\rho} \qquad for \; k = 0, K \qquad (2.33)$$

$$\frac{\partial \theta}{\partial \bar{\tau}} = B^2 \; \frac{1}{c_p} \frac{\partial}{\partial \bar{\xi}} \left(c_p \left[\frac{T}{T_u}\right]^{-0.3} \frac{W_{mix}}{W_{mix,\,u}} \frac{\partial \theta}{\partial \bar{\xi}} \right) -$$

$$\frac{t_{scl}}{\rho \, c_p (T_b - T_u)} \sum_{k=0}^{K} \dot{\omega}_k \, H_k \qquad (2.34)$$

with boundary conditions given by equations (2.10-2.11).

The standard-state thermodynamic properties are evaluated in terms of the polynomial fits of the specific heats at constant pressure, as done in Chemkin II [6]. The coefficients of the fits are taken from the SANDIA thermal data base file "THERMDAT". The properties of the mixture for the given mass fraction vector $\{Y_0, Y_1, ..., Y_K\}^T$ and temperature are evaluated as follows:

$$c_p = \sum_{k=0}^{K} \frac{C_{p,\,k} \, Y_k}{W_k} , \quad W_{mix} = \left[\sum_{k=0}^{K} \frac{Y_k}{W_k} \right]^{-1} ,$$

$$\rho = \frac{p \, W_{mix}}{R_u \, T} \qquad (2.35)$$

where c_p is the specific heat of mixture in mass units.

The following mechanism of 18 elementary non-reversible reactions and 13 reacting species was used to describe the methane-air atmospheric pressure combustion [7]:

Table 2. The chemical kinetics mechanism used in the model.
SPECIES :
      CH4 CH3 CH2O HCO CO2 CO
      H2 H O2 O OH   HO2 H2O N2 #

Reaction		A	n	E
CH4+H=>CH3+H2	;	2.2E4	3.0	8527.7
CH4+OH=>CH3+H2O	;	1.6E6	2.1	2452.2
CH3+O=>CH2O+H	;	7.0E13	0.0	0.0
CH2O+H=>HCO+H2	;	2.5E13	0.0	40003.3
CH2O+OH=>HCO+H2O	;	3.0E13	0.0	1199.8
HCO+H=>CO+H2	;	2.0E14	0.0	0.0
HCO+M=>CO+H+M	;	7.14E14	0.0	16811.7
HCO+O2=>CO+HO2	;	3.0E12	0.0	0.0
CO+OH=>CO2+H	;	4.4E6	1.5	-740.9
CO2+H=>CO+OH	;	1.6E14	0.0	26338.4
H+O2=>OH+O	;	1.2E17	-0.91	16532.0
OH+O=>H+O2	;	1.8E13	0.0	0.0
O+H2=>OH+H	;	1.5E7	2.0	7564.5
OH+H=>O+H2	;	6.7E6	2.0	5573.6
OH+H2=>H2O+H	;	1.0E8	1.6	3303.0
H+H2O=>OH+H2	;	4.6E8	1.6	18601.8
2*OH=>H2O+O	;	1.5E9	1.14	0.0
H2O+O=>2*OH	;	1.5E10	1.14	17282.5
H+O2+M=>HO2+M	;	2.0E18	-0.8	0.0
HO2+M=>H+O2+M	;	2.77E18	-0.8	46701.7
H+OH+M=>H2O+M	;	2.15E22	-2.0	0.0
H2O+M=>H+OH+M	;	3.87E23	-2.0	119397.7
HO2+H=>2*OH	;	1.5E14	0.0	1001.4
HO2+H=>H2+O2	;	2.5E13	0.0	690.7
HO2+OH=>H2O+O2	;	2.0E13	0.0	0.0

where each line describing a reaction contains the reaction equation, the pre-exponential factor, the temperature exponent, and the activation energy of the forward reaction constant, respectively. All numerical values are in CGS units except for the activation energy which is given in cal / mole. This mechanism is capable of predicting with

6

reasonable accuracy the burning velocity and the profiles of temperature and species mass fractions in lean to stoichiometric flames. The mechanism is read by an interpreter function which sets up the chemical kinetics and thermal data bases. The format of the mechanism description file is very close to that used in Chemkin II [6]. The calculation of the species production rates is also very similar and will not be described here. For the above reaction mechanism, the values of the third body efficiencies are give in [7] as

$$\alpha_{H, i} = 1, \quad \alpha_{H_2, i} = 1, \quad \alpha_{O_2, i} = 0.4$$

$$\alpha_{H_2O, i} = 6.5, \quad \alpha_{CO, i} = 0.75, \quad \alpha_{CO_2, i} = 1.5$$

$$\alpha_{CH_4, i} = 6.54, \quad \alpha_{N_2, i} = 0.4.$$

The values of third-body efficiencies for other species are equal to zero.

3. NUMERICAL SOLUTION

The numerical solution of equations (2.33-34) with boundary condition (2.10-11) is obtained using a Crank-Nicholson finite-difference scheme using an implicit approximation of the source term to maintain stability, and the Thomas tri-diagonal matrix inversion algorithm. The details of the numerical procedure were described extensively in our previous work [1] where a solution for the one-step chemistry model was obtained. Here we present only the features of the numerical procedure which are different when a multi-step chemical kinetics mechanism is considered.

First, in the case of multi-step chemistry, the grid in the computational domain $(\bar{\tau}, \bar{\xi})$ must be nonuniform because the reaction zone is thinner than the overall flame structure thickness. This is due to the difference in the time scales of the fast fuel consumption and the slow CO_2 formation reactions. Following a rapid initial increase in temperature in the reaction zone, a relatively long zone, of the order of 10 cm under normal conditions, is required for the temperature to reach its equilibrium value. Every time step, the grid is adapted in such a way that the regions of strong gradients of the dependent variables

$Y_0, Y_1, ..., Y_K, \theta$ are well resolved following the criteria:

$$|f_{i+1} - f_i| < \alpha \, |max \, (f) - min(f)| \qquad (3.1)$$

$$\left| \left(\partial f / \partial \bar{\xi} \right)_{i+1} - \left(\partial f / \partial \bar{\xi} \right)_i \right| <$$

$$\beta \, \left| max \left(\partial f / \partial \bar{\xi} \right) - min \left(\partial f / \partial \bar{\xi} \right) \right|$$

where α and β are the adaptation tolerance parameters of the order of 0.1; f_i and $\left(\partial f / \partial \bar{\xi} \right)_i$ are the values of a dependent variable and its derivative at grid point i. If criteria (3.1) are not satisfied, a new grid point is introduced half way between the points $i+1$ and i. The values of mass fractions and temperature at this midpoint are calculated as the average values: $f_{i+1/2} = \frac{1}{2} (f_{i+1} + f_i)$. This interpolation maintains the second order of accuracy.

Second, at the onset of every time step the thermal thickness of the flame is compared to the distance from the flame to the upstream and downstream boundaries of the computational domain. If either of these distances is smaller than two flame thicknesses, the computational domain is regridded by moving the boundaries further away from the flame. The values of the mass fractions and the temperature at the added mesh points are taken to be equal to the boundary values of the "old" mesh. Hence, the zero-gradient boundary conditions are naturally satisfied on the new mesh. Each time step, the physical coordinate y_i is recalculated in such a way that the stagnation point, $y_i = 0$, remains fixed.

Third, the time step of the calculation is taken to be the minimum of the characteristic time scales of species production:

$$t_{scl, \, k} \equiv \frac{1}{3} \frac{[X_{k, \, max}]}{max \, \{\dot{\omega}_k\}} \qquad (3.2)$$

where $max \, \{\dot{\omega}_k\}$ is the maximum of the production rate of the k-th species, $[X_{k, \, max}]$ is its molar concentration at this maximum; and the computational time scale based on a Courant criterion:

$$t_{scl, \, Courant} \equiv min \, \left\{ \Delta \bar{\xi} \right\}^2 exp \, (- 2 \, K_a \, \bar{\tau}), \quad (3.3)$$

7

i.e.

$$d\tau = min \ \{ \ t_{scl, \ 0}, \ t_{scl, \ 1}, t_{scl, \ 2}, \ ..., t_{scl, \ K}, t_{scl, \ Courant}/ \ 2 \ \} \quad . (3.4)$$

Equation (3.4) shows that the Courant time step is an exponentially decreasing function of time. For highly strained flames, at large K_a, the time step decreases rapidly with time, exponentially slowing down the calculation. A way to avoid this problem is to regrid the computational domain in such a way that $min \ \{\Delta \ \bar\xi\}^2$ is increased whenever the time step becomes exceedingly small.

We use the profiles provided by the SANDIA Premix Code with the chemical kinetics model described in Table 2 as the initial profiles.

4. RESULTS AND DISCUSSION

Comparison with Test Profiles

To establish the validity of our model, we tested the steady-state species mass fraction and temperature profiles obtained by our model in the case of unstrained and strained flame against those of Smooke [2] and Rogg [7], respectively. In the case of the unstrained flame, the profiles were plotted against the following normalized coordinate:

$$\hat{y} = \rho_u \ S_u \ (y - y_f) \ c_p/ \ \lambda \qquad (4.1)$$

In figure 2 we show the temperature and the reactants mole fraction profiles, CH_4 and O_2. The agreement between the model prediction and the exact solution is good, although the model slightly overpredicts the temperature in the flame region, while it underpredicts it on the reactants side. Consistent with these temperature profiles, our model produces slightly lower values for X_{CH_4} behind the reaction zone, $\hat{y} = 0$, than these obtained in Smooke's model [2]

In figures 3-4 the major species H_2O , H_2, CO, and CO_2, and the radical H mole fraction profiles are plotted. The agreement between the model results and the exact solution is very good. The strongest disagreement is detected in the values of H. Although the part of the profile on the reactants side and its maximum value are actually captured by our model, the post-flame values are

lower than that predicted in [2]. This could be explained by the strong sensitivity of the H profile to the temperature which is overpredicted by our model in the post-flame region (see figure 2). Since our model predicts accurately the major species profiles, we expect the burning velocity to be close to the exact value. The value provided by our model, 38 cm/s, is very close indeed to the exact solution value of 37.67 cm/s [2].

In the case of a highly strained flame, the test profiles of Rogg [7] and our profiles are plotted in broken and solid lines in figures 5-8. The profiles of Rogg [7] were shifted in such a way that the positions of the fuel consumption layers in both models match. The temperature profiles are shown in figure 5. Our model's profiles and those obtained using the original equations exhibit very close similarity, especially in the reaction zone region. In the post-flame zone, the temperature is higher in Rogg's results [7]. It should be noted that the equilibrium values of the temperature in both models are the same. However, the part of the domain shown in the figure is not large enough to include the "hot" boundary used in the calculations. The exact and model results for CH_4, H_2O and O_2 mass fractions are virtually identical. The CO_2 and CO mass fraction profiles are shown in figure 6. The profiles are identical in the reaction zone but differ slightly in the post-flame region. The profile of CO_2 predicted in [7] has slightly higher values of CO_2 mass fraction here. The same can be said about the CO mass fraction profiles. Clearly, the model predicts well the temperature and major species profiles with the maximum discrepancy in the CO profile being close to 10 % .

A more stringent test for the model is how accurately it predicts the minor species profiles. These species are present in very low concentrations, and many of them are extremely sensitive to the temperature and chemical kinetics mechanism. One of these species is HO_2 , which is shown in figure 7. The agreement between the model predictions and the exact solution is good, although the peak value is slightly overpredicted. In figure 8, OH, H, and O radicals profiles are depicted. Within the reaction zone, our profiles match well the exact solution. The post-flame values are, however, overpredicted by our model.

The above indicates that our model accurately predicts the integral characteristics of the flame, e.g. the burning velocity, and the major species profiles over a wide range of strains. Moreover, at all values of strain, the minor species are well predicted within the reaction zone but deviate somewhat on the products side. The reason

8

for the latter appears to be the absence of the momentum equation in our model. Although the momentum equation is redundant along the stagnation streamline, it provides means by which the condition

$$\varepsilon_b = \varepsilon_u \ \sqrt{\rho_u / \rho_b} \ ,$$

which relates the strains on the reactants and products sides, can be imposed. This condition implies that for the stoichiometric, atmospheric pressure flame the strain on the products side is approximately three times larger than that on the reaction side. Our model does not satisfy this boundary condition, accounting for the density variation in the reaction zone by the combustion velocity only, and hence it is does not allow the strain to vary throughout the flame structure. Thus, effectively, while the flame structure is resolved correctly, the strain rate on the products side in our model is lower than its actual value.

The Transient Dynamics of Strained Flames

The response of the flame to a step-wise change in the strain rate is now investigated using results of lean and stoichiometric flames. To vary the equivalence ratio, the number of moles of oxygen and methane are changed in such a way that the total number of the moles remains constant. Three values of the equivalence ratio are considered: $\phi = 0.6, 0.8, 1.0$. To characterize these flames, the steady-state values of the total heat release rate are plotted in figure 9 as a function of the strain rate and equivalence ratio . For the unstrained stoichiometric flame this value is close to 0.1 kJ/ cm^2-s. As the strain rate increases, the value gradually decreases to 0.07 kJ/ cm^2-s at $\varepsilon = $ 1800 1/s, corresponding to the Karlovitz number of 0.18. For leaner mixtures with equivalence ratios of 0.8 and 0.6, the total heat release is approximately 0.08 and 0.04 kJ/ cm^2-s, respectively. Again, the heat release rate decreases monotonically as the strain rate increases and the flame approaches extinction. Due to the boundary conditions (2.10-11), however, extinction is only an asymptotic state.

We found that the total heat release determines the flame dynamic response. A typical response of a flame with multi-step kinetics to a sudden change in the strain rate, shown in figure 10, is very similar to that observed when using a one-step kinetics. To quantify the flame response time, the total heat release as a function of time is interpolated using the following exponential function

$$\dot{Q} => a_1 + a_2 \ exp(- t / \tau),$$

$$\text{where } \dot{Q} \equiv \int_{-\infty}^{+\infty} \sum_{k=0}^{K} \dot{\omega}_k \ H_k dy \ ,$$

and the coefficients a_1, a_2 and τ are calculated using a least-square interpolation procedure.

In figure 11 the flame response time, τ, is shown as a function of the equivalence ratio and the applied strain. For every equivalence ratio considered, the time constant increases with strain, reaching a maximum around 700 1/s and then decreases. This value of strain corresponds to $K_a = 0.07, 0.103, 0.356$ for $\phi = 1, 0.8, 0.6$, respectively, . The impact of the strain on the response time can be explained as follows. In our previous paper [1], where a one-step kinetics model was used, we show that an increase in the heat release rate makes the flame responded faster to strain. Consistent with this result, the stoichiometric flame which has the highest heat release rate has the smallest response time. The maximum value of the $\tau \ (\ \phi, \varepsilon \ )$ curve can be explained by the competition between the different mechanisms controlling the flame dynamics. For lower values of strain, the influence of the flow manifests itself by moving the entire flame structure to a location in the stagnation flow where the mass conservation principle is satisfied. Within this range of strain rate, the structure of the flame does not change and the flame dynamics is controlled primarily by the thermal-diffusion time scale, which is $10^{-4}, 1.47 \ 10^{-4}, 5.11 \ 10^{-4}$ s. for $\phi = 1, 0.8, 0.6$, respectively. As figure 11 indicates, the switching from the regime controlled by the flame time scale to the regime controlled by the flow occurs around 700 1/s. For higher strains, the influence of the flow on the flame becomes so overwhelming that the flow time scale, $1/ \varepsilon$, starts to control the flame response. When the strain rate increases, the values of the response times of flames with different equivalence ratios become closer to each other and $\tau \ (\ \phi, \varepsilon \ )$ curves converge.

5. CONCLUSIONS

1. A model of unsteady strained flame with multi-step chemical kinetics has been developed by applying a series of mathematical

transformations to the system of equations governing flame propagation in a stagnation flow, and translating the system into a set of reaction-diffusion equations. The flame structure calculated by the model were compared with the exact solution for the cases of unstrained and highly strained stoichiometric, atmospheric pressure, methane-air flames. In the case of unstrained flame, very good agreement between the profiles has been obtained. In the case of highly strained flame the temperature and major species profiles were predicted well, while the minor species were overpredicted in the products region far behind the flame. The reason for these results is the absence of the momentum equation in our model. Although the momentum equation is redundant along the stagnation streamline, it provides means by which the boundary condition $\varepsilon_b = \varepsilon_u \sqrt{\rho_u/\rho_b}$,

which relates the strains on the reactants and products sides, can be imposed. Our model does not satisfy this boundary condition, accounting for the density variation in the reaction zone by the combustion velocity only, and hence it is does not allow the strain to vary throughout the flame structure. Thus, effectively, while the flame structure is resolved correctly, the strain rate on the products side in our model is lower than its actual value.

2. The transient dynamics of lean and stoichiometric flames, in response to a sudden change in strain, have been analyzed. It has been found that the dynamics is determined by the heat release rate in the flame. Therefore, the stoichiometric flame which has the highest heat release rate has the smallest response time. For leaner mixtures, flames respond more slowly and their time constants increase.

3. For a given equivalence ratio, the response time first increases with strain, reaching a maximum at approximately 700 1/s, then monotonically decreases. Two regimes of flame response have been identified. In the lower strain regime, the flame is convected by the flow while its structure remains almost unchanged and the flame dynamics is governed by the thermal-diffusion time scale, which increases with equivalence ratio. In the second regime the influence of the flow on the flame structure is dominant, the flow time scale determines the flame dynamics and makes it independent from the equivalence ratio.

4. In turbulent combustion simulation, our results show that only near-stoichiometric flames demonstrates instantaneous response to

typical strains and can be treated as steady. Otherwise, the unsteady local flame response must be considered in detail.

REFERENCES

1. Petrov, C. and Ghoniem, A.F. , " An Unsteady Strained Flame Model for Turbulent Combustion Simulations", *AIAA - 94 - 0776*, 32-nd Aerospace Sciences Meeting & Exhibit, January 10-13, 1994, Reno, NV. To appear in *Combustion and Flame*.

2. Smooke, M.D. and Giovangigli, V. ,"Formulation of the Premixed and Nonpremixed Test Problems," *Lecture Notes in Physics, 384*, 1, 1990.

3. Rutland and Ferziger, "Unsteady Strained Premixed Laminar Flames", *Comb. Sci. Tech., 73*, 305, 1990.

4. Kee,R.J., Dixon-Lewis, G., Warnatz, J., Coltrin, M.E., Miller,J.A., " A Fortran Computer Code Package for the Evaluation of Gas-Phase, Multicomponent Transport Properties,"*SANDIA Report SAND86-8246,* 1986.

5. Kee, R.J., Grcar, J.F., Smooke, M.D., Miller, J.A., " A Fortran Program for Modeling Steady Laminar One-Dimensional Premixed Flames," *SANDIA Report SAND85-8240*, 1985.

6. Kee, R.J., Rupley, F.M., Miller,J.A., " Chemkin-II: A Fortran Chemical Kinetics Package for analysis of Gas-Phase Chemical Kinetics," *SANDIA Report SAND89-8009* , 1989.

7. Rogg, B., " Response and Flamelet Structure of Stretched Premixed Methane-Air Flames,", *Comb. Flame, 73*, 45, 1988.

8. Darabiha, N., Candel, S. M., Giovangigli, V., Smooke,M.D.," Extinction of Strained Premixed Propane-Air Flames with Complex Chemistry, "*Combust. Sci. and Tech., 60*, 267, 1988.

9. Stahl, G. and Warnatz, J., " Numerical Investigation of Time-Dependent Properties and Extinction of Strained Methane- and Propane-Air Flamelets, " *Combustion and Flame, 85*, 285, 1991.

10. Giovangigli, V. and Smooke, M.D., " Calculation of Extinction Limits for Premixed

Laminar Flames in a Stagnation Point Flow, "
Journal of Computational Physics, **68**, 327, 1987.

11. Kee, R.J., Miller, J.A., Evans, G.H. and Dixon-Lewis, G.," A Computational Model of the Structure and Extinction of Strained, Opposed Flow, Premixed Methane-Air Flames," *Twenty Second Symposium (International) on Combustion*, The Combustion Institute, 1988, pp. 1479-1494.

12. Egolphopoulos, F.N. , " Dynamics and Structure of Unsteady, Strained, Laminar Premixed Flames, " *Twenty Fifth Symposium (International) on Combustion*, The Combustion Institute, 1994.

13. Ghomiem, A.F., Soteriou,M.C., Knio,O.M., Cetegen, B.," Effects of Steady and Periodic Strain on Unsteady Flamelet Combustion," *Twenty -Fourth Symposium (International) on Combustion*, The Combustion Institute, 1992, pp. 223-230.

NOMENCLATURE

ρ - the mixture density,

$\vec{v} = (u, v)$- the total velocity of fluid,

$\vec{V} = (U, V)$ - the inviscid irrotational velocity component,

$\vec{v_c} = (u_c, v_c)$:- the combustion generated velocity,

Y_k - the mass fraction of the k -th species,

X_k- the mole fraction of the k -th species,

$[X_k]$- the molar concentration of the k -th species,
D_k -the mixture averaged diffusion coefficient of the k -th species,

$\dot{\omega}_k$ - the production rate of the k -th species,

W_k - the molecular weight of the k -th species,
c_p - the constant pressure specific heat of mixture, mass units,

$c_{p, k}$ - the constant pressure specific heat of the k -th species, mass units,

$K+1$ -the total number of chemical species,

T - the thermodynamic temperature,

p - the pressure,

λ - the thermal conductivity of mixture,

R_u - the universal gas constant,

W_{mix} - the molecular weight of mixture,
H_k - the enthalpy of the k -th species, molar units,

V_k- the diffusion velocity,

V_{cor} - the correction velocity,

$k_{T, k}$ - the thermal diffusion coefficient of the k -th species,

(x, y, t) - physical coordinates,

$(\tilde{y}, \tilde{t})$- coordinates of the first transformed domain,

$(\bar{\xi}, \bar{\tau})$ - computational coordinates,

$\varepsilon(t)$ - the strain rate,

$L_{e, k}$- the Lewis number of the k -th species,

α- the thermal diffusivity of mixture,

θ- the non-dimensional temperature,
α_{ki}- the third-body coefficient of the k -th species in reaction i,

p_{atm}- the pressure of one atmosphere,

SUBSCRIPTS

u- unburnt mixture,

b- burnt mixture,

scl- scale value,

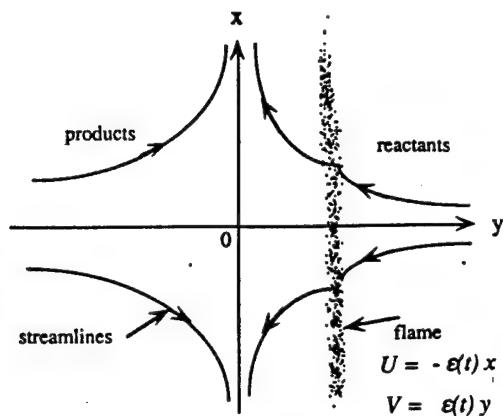k- species number,

n- time layer number,

mix- mixture.

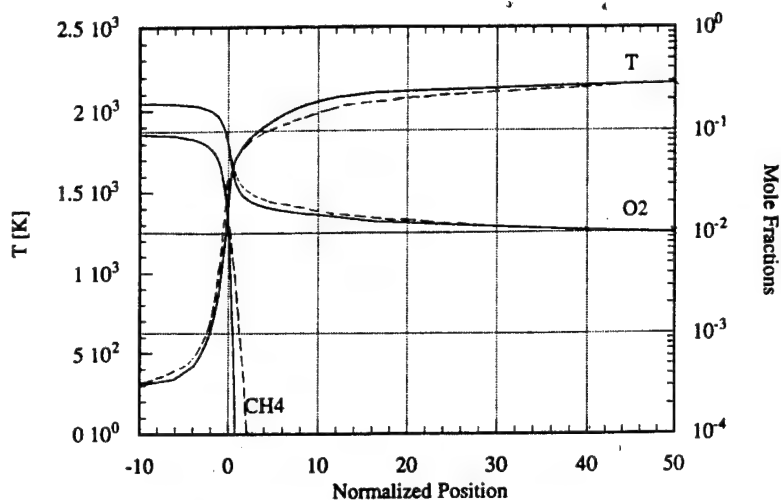Figure 1. Flame propagation in a stagnation point flow.

Figure 2. A comparison between the computed temperature and mole fraction profiles for a stoichiometric, unstrained flame obtained by our model (solid line) and by Smooke's model (dashed line).
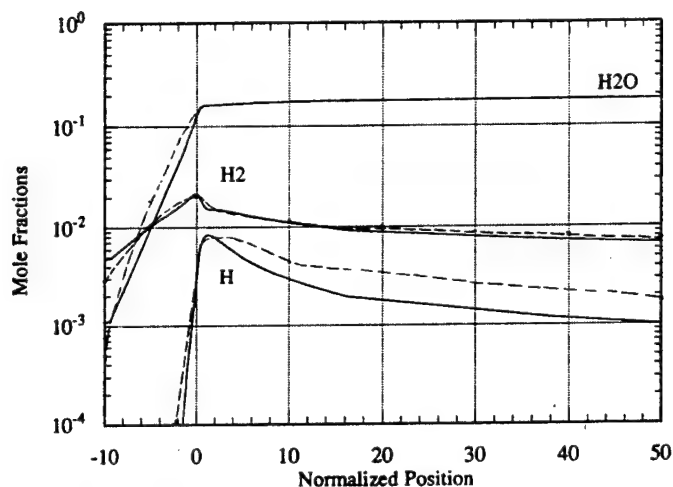

Figure 3. A comparison between the computed mole fraction profiles for a stoichiometric, unstrained flame obtained by our model (solid line) and by Smooke's model (dashed line).
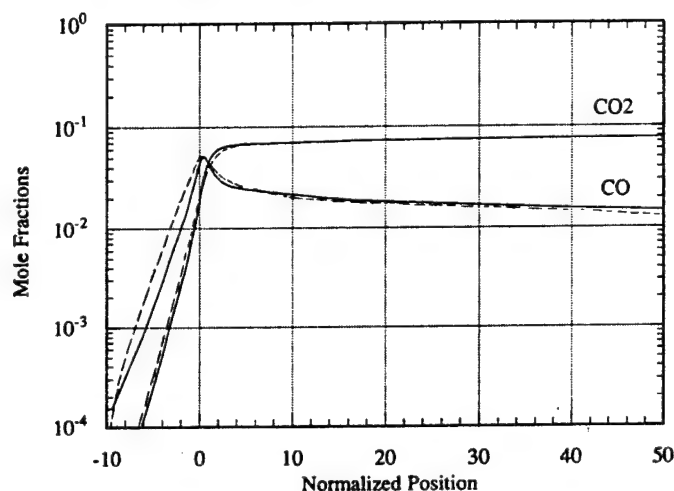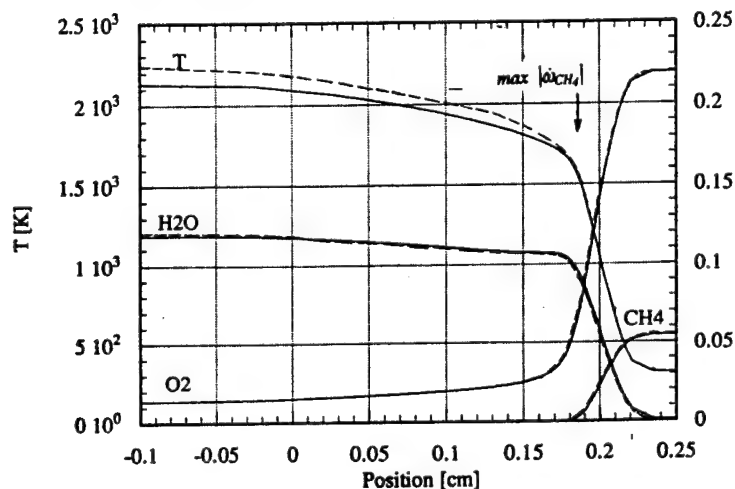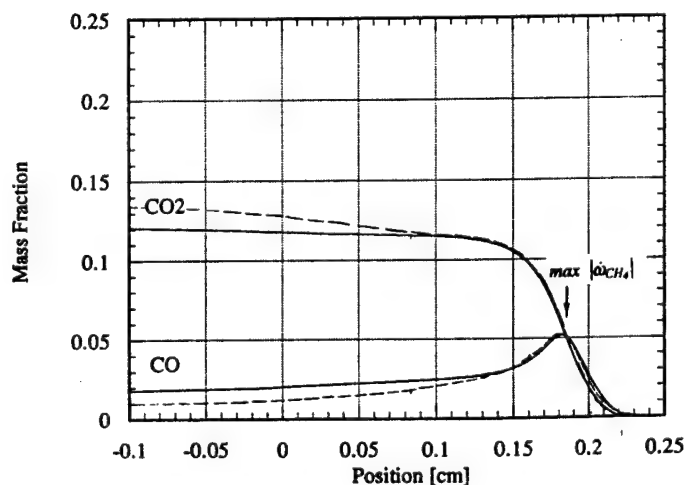

Figure 4. A comparison between the computed mole fraction profiles for a stoichiometric, unstrained flame obtained by our model (solid line) and by Smooke's model (dashed line).

Figure 5. A comparison between the computed temperature and mass fraction profiles for a stoichiometric, strained flame employing our model (solid line) and the model of Rogg (dashed line); strain rate = 1,000 1/s.

Figure 6. A comparison between the computed mass fraction profiles for a stoichiometric, strained flame employing our model (solid line) and the model of Rogg (dashed line); strain rate = 1,000 1/s.
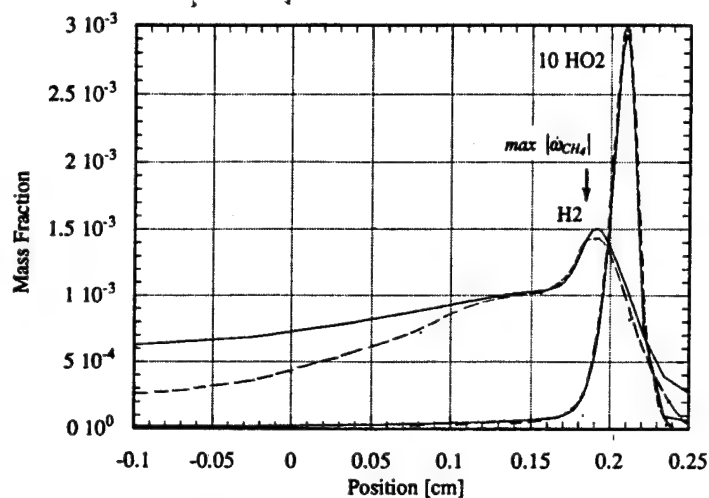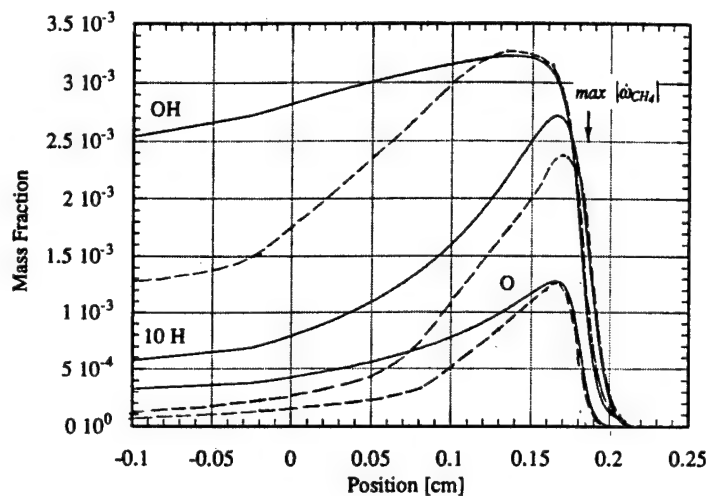
Figure 7. A comparison between the computed mass fraction profiles for a stoichiometric, strained flame employing our model (solid line) and the model of Rogg (dashed line); strain rate = 1,000 1/s.

Figure 8. A comparison between the computed mass fraction profiles for a stoichiometric, strained flame employing our model (solid line) and the model of Rogg (dashed line); strain rate = 1,000 1/s.
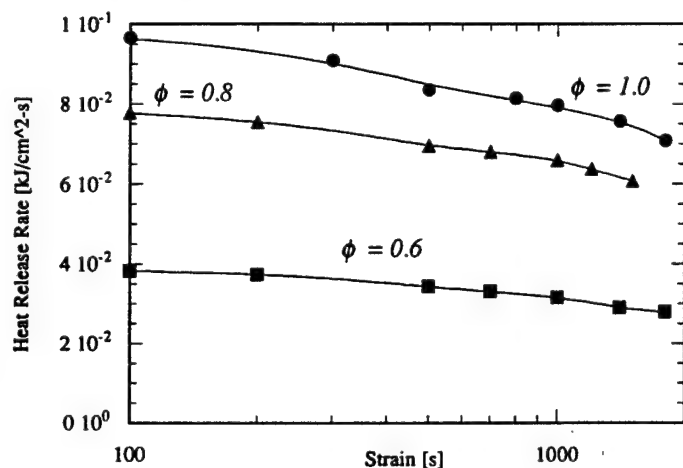
Figure 9. The steady-state heat release rate of a premixed, methane-air flame as a function of the strain rate and the equivalence ratio.
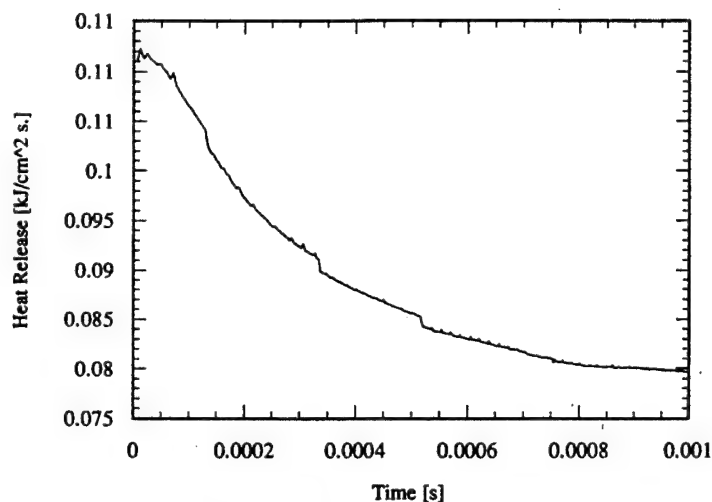

Figure 10. A typical response of a premixed, stoichiometric, atmospheric pressure, methane-air flame to a step-wise change in the strain rate; strain rate = 1,000 1/s.
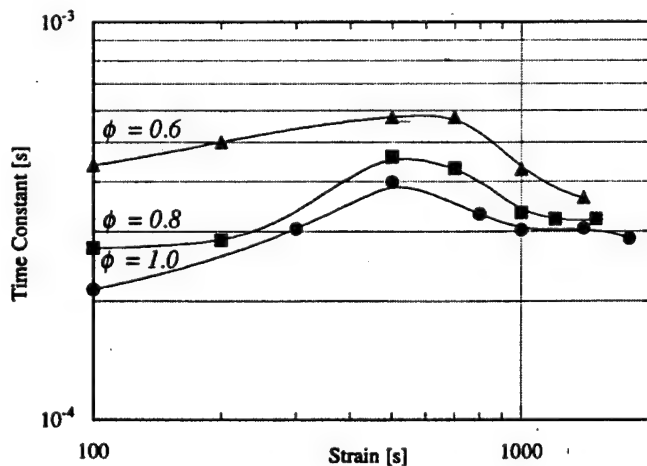

Figure 11. The response time of a premixed, methane-air flame as a function of the applied strain and the equivalence ratio.

APPENDIX III

A Uniform Strain Model of Elemental Flame for Turbulent Combustion Simulation

Constantin Petrov and Ahmed Ghoniem,
Massachusetts Institute of Technology,
Cambridge MA 02139, USA

I. *Introduction*

The paper describes part of our effort to develop an unsteady strained laminar flame model with detailed chemistry and transport which can be used as a combustion submodel in a turbulent combustion simulation. The combustion submodel is based on tracking the flame surface as it is expanded, convoluted and strained by the turbulent structures. The flame surface is divided into a large number of elemental flames, whose burning rate (diffusion flame) or burning velocity (premixed flame) is computed using the elemental flame structure solution. In order to predict correctly the burning rate and the pollutants formation in a turbulent reacting flow, each flame and its interactions with other elemental flames must be modeled adequately, i.e. all important phenomena which affect instantaneous flame structure must be accounted for in numerical model.

It has been determined in a large number of previous studies (see, e.g., a review by Peters [1]) that the strain rate, unbalanced molecular diffusion and curvature effects can significantly alter the burning rate. In our previous papers (Refs. [2]-[4]) we established that a flame does not respond instantaneously to a rapid change in the strain rate, frequently making the quasi-steady assumption inappropriate. Similar results regarding the importance of transient response were also obtained in Refs. [5] - [8]. The requirement of predicting the pollutants formation, such as CO and NOx, necessitates application of complex chemistry or reduced kinetics mechanisms. Furthermore, at some locations of a nonpremixed combustor premixed or partially premixed combustion occurs and must be simulated using the same flame model.

Summarizing, a model of elemental flame must account for the following physical phenomena : (1) the strain rate, (2) unsteadiness of flame-flow interaction, (3) complex chemistry

1

and transport. It must be able to (4) predict diffusion, premixed and partially premixed flames at the same time. As far as the numerical requirements are concerned, the model should be (5) numerically efficient and (6) robust in order to be able to predict such extreme phenomena as ignition and extinction. If these requirements are to be met, the influence of curvature on combustion should be accounted on a global scale by combining elemental flames and modeling their interaction. This problem is beyond the scope of our paper.

The specifications of the model are implemented as follows. The effect of the strain rate exerted by the flow on the flame is accounted for by considering the widely used configuration of flame propagating in a stagnation point flow. After testing the shooting technique and finite-difference boundary-value-problem technique of solving the equations governing flame propagation in this type of flow, we chose to solve the transient problem using an implicit finite difference scheme. This approach satisfies requirements (1)-(4) and (6). As far as the requirement (5) of numerical efficiency is concerned, we found that the rapid advances in the computer technology and the robustness of the time integration procedure in the region near flammability limits, ignition and in the case of, for example, high pressure, outweighs perceived high computational cost as compared to the finite-difference boundary-value-problem techniques used by Smooke [10], Rogg [11], Kee et. al. [16].

In this paper we propose two approaches to compute the structure of an elemental flame. Both are able to predict unsteady one-dimensional premixed as well as diffusion flames. In the first, which we call the Unsteady Strained Elemental Flame (*USEF*), we integrate the unsteady continuity, momentum, energy and species mass fraction equations governing flame propagation in a stagnation point flow. We use this solution as a benchmark to compare with the predictions of the Uniformly Strained Elemental Flame (*UniSEF*) model in which we assume a uniform effective strain throughout the flame structure. This simplification allows us to decouple the energy and mass fraction equations from the momentum equation and to transform the former into a set of reaction- diffusion equations. The advantage of solving the reaction- diffusion equations governing *UniSEF* instead of the full system governing *USEF* is the robustness of the numerical integration

2

procedure used in the former since the troublesome convective terms are eliminated from the system. Another advantage is the reduced number of governing equations. While this may have little significance in the case of detailed chemical kinetics since most of the run time is spend calculating the Jacobian and the chemical source terms, it could be important if a reduced chemical kinetics mechanism with a smaller number of species is adopted.

The paper is organized as follows. In Section II, we present the formulation and the reduction to the *UniSEF*. In Section III, we describe the numerical procedure used to integrate the equations in both cases. In Section IV, we compare the solution of *USEF* with these of Ref. [10], and investigate the error in *UniSEF* by comparing its results with those of *USEF* in terms of the steady state premixed and diffusion flame structures and their time responses.

II. *Formulation*

In the *USEF* model, we integrate a reduced version of the unsteady equations governing the strained flame propagation along the stagnation streamline of a stagnation point flow (12.11-14) of Ref. [9]. We start with the general unsteady equations for mass, momentum, chemical species and energy :

$$\frac{\partial \rho}{\partial t} + \frac{\partial(\rho u)}{\partial x} + \frac{\partial(\rho v)}{\partial y} = 0 \tag{1}$$

$$\rho \frac{\partial u}{\partial t} + \rho u \frac{\partial u}{\partial x} + \rho v \frac{\partial u}{\partial y} + \frac{\partial p}{\partial x} - \frac{\partial}{\partial y}\left(\mu \frac{\partial u}{\partial y}\right) = 0 \tag{2}$$

$$\rho \frac{\partial Y_k}{\partial t} + \rho u \frac{\partial Y_k}{\partial x} + \rho v \frac{\partial Y_k}{\partial y} - \frac{\partial}{\partial y}\left(\rho D_k \frac{\partial Y_k}{\partial y}\right) - \dot{\omega}_k W_k = 0 \quad k = 1, ..., KK \tag{3}$$

$$\rho \frac{\partial T}{\partial t} + \rho u \frac{\partial T}{\partial x} + \rho v \frac{\partial T}{\partial y} - \frac{1}{c_p}\frac{\partial}{\partial y}\left(\lambda \frac{\partial T}{\partial y}\right) + \sum_{k=1}^{KK} \frac{\dot{\omega}_k H_k}{c_p} = 0 \tag{4}$$

where x and y axes are directed parallel and perpendicular to the flame, respectively, t is the time, u and v are the x and y velocity components, ρ is the density, p is the pressure, μ is the

3

molecular viscosity, Y_k is the mass fraction, D_k is the diffusion coefficient, W_k is the molecular weight, $\dot{\omega}_k$ is the production rate, T is the temperature, c_p is the specific heat of mixture in mass units, λ is the thermal conductivity of mixture, H_k is the total enthalpy in mole units. The system of equations is closed by the ideal gas law. We neglected the enthalpy flux term in the energy equation and the thermal diffusion velocity in the species equations. It has been shown by Smooke [10], and confirmed by us, that these terms are relatively unimportant.

The free-stream velocity outside the boundary layer is given by

$$u_\infty = \varepsilon(t)\, x$$ (5)

where ε is the strain rate. In the outer layer the y-derivatives in the momentum equation are negligible and we can write

$$\rho\, \frac{\partial u_\infty}{\partial t} + \rho u_\infty \frac{\partial u_\infty}{\partial x} + \frac{\partial p}{\partial x} = \rho\, u_\infty \frac{1}{\varepsilon} \frac{\partial \varepsilon}{\partial t} + \rho u_\infty \varepsilon + \frac{\partial p}{\partial x} = 0 \quad,$$

which allows us to express the pressure gradient as a function of the imposed velocity. Considering the solution of the above equations along the stagnation streamline, $x = 0$, where $u = 0$, $\dfrac{\partial}{\partial x} = 0$ and introducing the notations of Ref. [2] $U = u / u_\infty$, $V = \rho v$, we rewrite Eqs. (1) - (4) as follows

$$\frac{\partial \rho}{\partial t} + \rho U \varepsilon + \rho u_\infty \frac{\partial U}{\partial x} + \frac{\partial V}{\partial y} = 0$$ (6)

$$\rho\, u_\infty \frac{\partial U}{\partial t} + \rho\, U\, u_\infty \frac{1}{\varepsilon} \frac{\partial \varepsilon}{\partial t} + \rho u_\infty^2 U \frac{\partial U}{\partial x} + \rho u_\infty U^2 \varepsilon + $$

4

$$V u_\infty \frac{\partial U}{\partial y} - \rho_\infty u_\infty (\frac{1}{\varepsilon} \frac{\partial \varepsilon}{\partial t} + \varepsilon) - u_\infty \frac{\partial}{\partial y} \left(\mu \frac{\partial U}{\partial y} \right) = 0 \tag{7}$$

$$\rho \frac{\partial Y_k}{\partial t} + \rho u_\infty U \frac{\partial Y_k}{\partial x} + V \frac{\partial Y_k}{\partial y} - \frac{\partial}{\partial y} \left(\rho D_k \frac{\partial Y_k}{\partial y} \right) - \dot{\omega}_k W_k = 0 \tag{8}$$

$$\rho \frac{\partial T}{\partial t} + \rho u_\infty U \frac{\partial T}{\partial x} + V \frac{\partial T}{\partial y} - \frac{1}{c_p} \frac{\partial}{\partial y} \left(\lambda \frac{\partial T}{\partial y} \right) + \sum_{k=1}^{KK} \frac{\dot{\omega}_k H_k}{c_p} = 0 \tag{9}$$

In the momentum equation there are two terms containing the time derivative of strain. Since the density inside the flame is usually much lower than the density outside and U is of order of unity, the following inequality holds

$$\rho U u_\infty \frac{1}{\varepsilon} \frac{\partial \varepsilon}{\partial t} << \rho_\infty u_\infty \frac{1}{\varepsilon} \frac{\partial \varepsilon}{\partial t} .$$

In the vicinity of the stagnation streamline $u_\infty = \varepsilon x \approx 0$. It can be demonstrated using dimensional analysis that close to the stagnation streamline all convective terms in the x- direction are small compared to the corresponding terms in the y-direction. Dividing the momentum equation by u_∞ , we finally obtain

$$\rho \frac{\partial U}{\partial t} + V \frac{\partial U}{\partial y} - \frac{\partial}{\partial y} \left(\mu \frac{\partial U}{\partial y} \right) - \rho_\infty (\varepsilon + \frac{1}{\varepsilon} \frac{\partial \varepsilon}{\partial t}) + \rho U^2 \varepsilon = 0 \tag{10}$$

Close to the stagnation streamline, the remaining governing equations take the form

$$\frac{\partial \rho}{\partial t} + \rho U \varepsilon + \frac{\partial V}{\partial y} = 0 \tag{11}$$

5

$$\rho \frac{\partial Y_k}{\partial t} + V \frac{\partial Y_k}{\partial y} - \frac{\partial}{\partial y}\left(\rho D_k \frac{\partial Y_k}{\partial y}\right) - \dot{\omega}_k W_k = 0 \tag{12}$$

$$\rho \frac{\partial T}{\partial t} + V \frac{\partial T}{\partial y} - \frac{1}{c_p}\frac{\partial}{\partial y}\left(\lambda \frac{\partial T}{\partial y}\right) + \sum_{k=1}^{KK} \frac{\dot{\omega}_k H_k}{c_p} = 0 \tag{13}$$

In the two jet configuration, the following boundary conditions apply

$$at \ y = +\infty \ : \ Y_k = Y_{k,+\infty}, T = T_{+\infty}, U = 1$$

$$at \ y = -\infty \ : \ Y_k = Y_{k,-\infty}, T = T_{-\infty}, U = \sqrt{\rho_{+\infty}/\rho_{-\infty}} \tag{14}$$

$$at \ y = 0 \ : V = 0 \ .$$

In the Tsuji configuration, we have

$$at \ y = +\infty \ : Y_k = Y_{k,+\infty}, T = T_{+\infty}, U = 1 \ ,$$

$$at \ y = y_w : \ Y_k = Y_{k,w} - \left(\rho D \ \partial Y_k/\partial y\right)_w / V_w, T = T_w, U_w = 0 \ , \tag{15}$$

where subscript "w" indicates the values taken at the burner surface. The mass flux at this surface, V_w, is considered to be a known value. Both configurations are shown in Fig. 1. The above equations and the boundary conditions can be applied to the strained diffusion and premixed flames. Next, we formulate the alternative *UniSEF* model.

The *UniSEF* model is based on the approach suggested by Carrier et. al. [12] for diffusion flames with infinite rate chemistry, extended by Rutland and Ferziger [13] to the unity Lewis number premixed flame with single step chemistry, by Cetegen and Bogue [7] to a diffusion flame, by Ghoniem et.al. [6] to a diffusion flame with single step chemistry and by Petrov and Ghoniem [2] to the nonunity Lewis number premixed flame with single step chemistry, and to the complex chemistry premixed flame [3]. The solution procedure for a generic strained (i.e. premixed and/ or diffusion) flame is identical to that described in detail in Ref. [3]. Eqs (1)-(4) written along the stagnation streamline take the form :

6

$$\frac{\partial \rho}{\partial t} + \rho \frac{\partial u}{\partial x} + \frac{\partial(\rho v)}{\partial y} = 0 \qquad , \tag{16}$$

$$\rho \frac{\partial Y_k}{\partial t} + \rho v \frac{\partial Y_k}{\partial y} = \frac{\partial}{\partial y}\left(\rho D_k \frac{\partial Y_k}{\partial y}\right) + \dot{\omega}_k W_k, \, k = 1, .., K \qquad , \tag{17}$$

$$\rho c_p \frac{\partial T}{\partial t} + \rho c_p v \frac{\partial T}{\partial y} = \frac{\partial}{\partial y}\left(\lambda \frac{\partial T}{\partial y}\right) - \sum_{k=0}^{K} \dot{\omega}_k H_k , \tag{18}$$

where x-momentum equation is eliminated because it is trivially satisfied. We decompose the velocity field into two components :

$$\vec{v} = \vec{v_p} + \vec{v_c} \qquad , \tag{19}$$

where $\vec{v}$ is the total velocity, $\vec{v_c}$ is the combustion generated velocity, and $\vec{v_p}$ is the externally imposed velocity which satisfies the following incompressible continuity equation:

$$\nabla . \vec{v_p} = 0 \tag{20}$$

If the externally imposed inviscid irrotational velocity field ,$\vec{v_p}$, is specified as

$$\vec{v_p} = (\, \varepsilon_{eff}(t) \, x, \, -\varepsilon_{eff}(t) \, y \,) \tag{21}$$

where ε_{eff} is the *effective* strain rate, then the following transformations (see Ref. [3]), where the overbar denotes the density normalized by its value at positive infinity, $\rho_{+\infty}$,

$$\tilde{y} = exp \, (\int_0^t \varepsilon_{eff}(t') \, dt') \, y \equiv B(t) y, \, \tilde{t} = t \qquad \xi = \int_0^{\tilde{y}} \bar{\rho} \, d\tilde{y}' \, , \quad \tau = \tilde{t} \tag{22}$$

eliminate the $v_p\, \partial/\partial y$ operators from the governing equations. The uniform strain model assumes a constant value of strain across the flame, ε_{eff}. However, in the exact solution, the values of strain change inside the flame structure from ε_{max} and ε_{min} which can be significantly different. The exact steady state profiles of temperature, heat release rate and normalized strain rate U in premixed and diffusion flame are shown in Fig. 2. The location of the maximum heat release rate is denoted by a vertical dashed line. We found that an effective strain rate equal to the strain inside the reaction zone, i.e. the value of strain at the intersection of the dashed line and the strain rate profile significantly improves the predictions of the *UniSEF* solution. For a premixed and diffusion flame, this value is approximately equal to average of the minimum and maximum values of strain in the domain, ε_{max} and ε_{min}, i.e.

$$\varepsilon_{eff} = (\varepsilon_{max} + \varepsilon_{min})/2 = \varepsilon_{+\infty} \left(1 + (\rho_{+\infty}/\rho_b)^{1/2}\right), \tag{23}$$

where $\varepsilon_{min} = \varepsilon_{+\infty}$ and ρ_b corresponds to the adiabatic flame temperature. In the derivation of this relationship the momentum equation we used and the first and second derivatives of U at the location of ε_{max} assumed to be equal zero.

Mapping the governing equations onto the (ξ, τ) domain, we get the final form of the *UniSEF* equations:

$$\frac{\partial Y_k}{\partial \bar{\tau}} = \frac{B^2(\bar{\tau})}{\alpha_{+\infty}} \frac{\partial}{\partial \bar{\xi}} \left(D_k \, \bar{\rho}^2 \frac{\partial Y_k}{\partial \bar{\xi}} \right) + \frac{t_{scl} \, \dot{\omega}_k \, W_k}{\rho} \quad for\ k = 1, ..., K, \tag{24}$$

$$\frac{\partial \theta}{\partial \bar{\tau}} = \frac{B^2(\bar{\tau})}{\rho_{+\infty} c_p \alpha_{+\infty}} \frac{\partial}{\partial \bar{\xi}} \left(\lambda \, \bar{\rho} \frac{\partial \theta}{\partial \bar{\xi}} \right) - \frac{t_{scl}}{\rho \, c_p T_{+\infty}} \sum_{k=1}^{K} \dot{\omega}_k \, H_k \quad . \tag{25}$$

These equations are non-dimensionalized using a length scale based on the thermal diffusion length, i.e. $y_{scl} = \sqrt{\alpha_{+\infty} t_{scl}}$, where $\alpha_{+\infty}$ is the thermal diffusivity coefficient of the mixture at

8

infinity, $t_{scl} = 10^{-4}s$. The non-dimensional temperature is $\theta = T / T_{+\infty}$, $\bar{\xi} = \xi / y_{scl}$, and $\bar{\tau} = \tau / t_{scl}$. The boundary conditions remain the same as in Eqs. (14) or (15) with the exception of those for U and V which are not required anymore.

In order to solve the governing equations of *USEF* and *UniSEF* a transport model is necessary to evaluate the mixture conductivity and the diffusion coefficients of chemical species. We adopted a simplified approach of Smooke [10] :

(a) the Lewis numbers of different species are constant in y - direction

$$L_{e,k} = \frac{\lambda}{\rho \, c_p \, D_k} = const \quad , \tag{26}$$

(b) the following curve fit can be used to calculate the ratio λ / c_p

$$\lambda / c_p = 2.58 \; 10^{-4} \, (T / 298)^{0.7} \quad (CGS \; units) \quad , \tag{27}$$

and

(c) the Prandtl number is constant and equal to 0.75

$$\frac{\partial}{\partial y} (\mu \frac{\partial U}{\partial y}) = P_r \frac{\partial}{\partial y} (\frac{\lambda}{c_p} \frac{\partial U}{\partial y}) = 0.75 \frac{\partial}{\partial y} (\frac{\lambda}{c_p} \frac{\partial U}{\partial y}) \quad .$$

The validity of these assumptions has been extensively tested and confirmed by us using Chemkin Transport Properties Package [14]. However, Smooke [10] demonstrates that this simple transport model leads to a lower value of the extinction strain. We exercised caution in applying this model and tested the results produced by *USEF* against those obtained using the complex transport version of the model which is also available.

9

The starting chemistry models of methane oxidation due to Smoke [10] is used in the paper. It contains 25 reactions and 16 species.

III. *Numerical Solution Method*

The numerical solution of Eqs (10)-(13) and (24)-(25) with boundary conditions (14) or (15) is obtained using an implicit Euler method and Newton-like iterations. Here as an example we present the finite-difference approximation of Eq. (13). Other equations are descretized similarly. Assume that all dependent variables are known at time layer n. In the implicit Euler method, the time derivatives are approximated as

$$\rho \frac{\partial T}{\partial t} \approx \rho_j^{n+1} \frac{T_j^{n+1} - T_j^n}{\Delta t}, \tag{28}$$

where subscript j indicates the grid point and the superscript n denotes the n-th time layer, Δt is the time step.

An approximation of the convective term in *USEF* is extremely important for the accuracy and stability of the simulation. In our method, we use a central difference formula

$$V \frac{\partial T}{\partial y} \approx V_j^{n+1} \left(\frac{h_{j-1} T_{j+1}^{n+1}}{h_j (h_j + h_{j-1})} + \frac{(h_j - h_{j-1}) T_j^{n+1}}{h_j h_{j-1}} - \frac{h_j T_{j-1}^{n+1}}{h_{j-1} (h_j + h_{j-1})} \right), \tag{29}$$

where $h_j = y_{j+1} - y_j$, to calculate the first derivatives in the convective terms wherever it is possible. In the regions of potential numerical instability we use the following upwind derivatives

$$V \frac{\partial T}{\partial y} \approx V_j^{n+1} \frac{T_{j+1}^{n+1} - T_j^{n+1}}{h_j} \quad \text{if} \quad V_j^n < 0 \qquad \text{, and} \tag{30}$$

$$V \frac{\partial T}{\partial y} \approx V_j^{n+1} \frac{T_j^{n+1} - T_{j-1}^{n+1}}{h_{j-1}} \quad \text{if} \quad V_j^n > 0 \tag{31}$$

In these regions the first derivative of temperature repeatedly changes sign. The diffusion and the source terms in *USEF* and *UniSEF* are approximated in the usual way

$$\frac{1}{c_p} \frac{\partial}{\partial y} \left(\lambda \frac{\partial T}{\partial y} \right) \approx \frac{1}{c_{p,j}^{n+1}} \frac{2}{y_{j+1} - y_{j-1}} \left[\lambda_{j+1/2}^{n+1} \frac{T_{j+1}^{n+1} - T_j^{n+1}}{h_j} - \lambda_{j-1/2}^{n+1} \frac{T_j^{n+1} - T_{j-1}^{n+1}}{h_{j-1}} \right] ,$$

$$\sum_{k=1}^{KK} \frac{\dot{\omega}_k H_k}{c_p} \approx \sum_{k=1}^{KK} \frac{\dot{\omega}_{k,j}^{n+1} H_k^{n+1}}{c_{p,j}^{n+1}} , \tag{32}$$

where subscript $j+1/2$ indicates the value taken half-way between the j-th and the (j+1)-th mesh points.

The resulting system of non-linear algebraic equations is solved by a damped Newton algorithm. In the *USEF* model, we define the i-th Newton iteration of the partial (without V - component) solution vector $\phi^{n+1\,(i)}$ at the $(n+1)$ time layer as follows

$$\phi^{n+1,\,(i)} = \{ \; Y_{k,1}^{n+1,\,(i)}, T_1^{n+1,\,(i)}, U_1^{n+1,\,(i)} \; ; \, ...;$$

$$Y_{k,j}^{n+1,\,(i)}, T_j^{n+1,\,(i)}, U_j^{n+1,\,(i)} \; ; \, ...;$$

$$Y_{k,JJ}^{n+1,\,(i)}, T_{JJ}^{n+1,\,(i)}, U_{JJ}^{n+1,\,(i)} \}^T \; , \; k = 1, \, ..., \, KK$$

In the *UniSEF* model, the solution vector has no U and V - components. When an arbitrary solution vector is substituted into the finite-difference analog of Eqs (10) - (13) and (24)-(25), the right-hand-sides of these equations are not equal to zero as they would if the true solution were

substituted. We denote this residual vector by F. The purpose of the Newton iterations is to find a vector $\phi^{n+1\,(i)}$ which satisfies the following equation

$$F\left(\phi^{n+1\,(i)}\right) = 0$$

with acceptable accuracy.

The initial guess of the solution vector is obtained by extrapolating the converged solution vectors from two previous time steps. Once the initial guess is obtained, the next iteration for the solution vector at the (n+1) time layer is calculated using a damped Newton- like algorithm

$$F\left(\phi^{n+1,\,(i)}\right) = -\chi^{(i)}\left(\frac{\partial F}{\partial \phi}\right)^{n+1,\,(i)}\left(\phi^{n+1,\,(i+1)} - \phi^{n+1,\,(i)}\right) \tag{33}$$

where $\partial F / \partial \phi$ is the numerically evaluated Jacobian matrix,

$$(\partial F / \partial \phi)^{n+1,\,(i)} \approx \left(F\left(\phi^{n+1,\,(i)} + \delta\right) - F\left(\phi^{n+1,\,(i)}\right)\right) / \delta, \quad \delta = 0.0001\,\phi^{n+1,\,(i)},$$

and $\chi^{(i)}$ is a damping coefficient of order of unity. For the given system of equations the Jacobian matrix has a block - tridiagonal structure. The system of linear algebraic Eqs (33) is solved numerically using a standard numerical procedure (see Ref. [15]). The Newton - like iterations continue until a norm of the correction vector, $\left|\phi^{(i)}_{cor}\right| = \left|\phi^{n+1,\,(i+1)} - \phi^{n+1,\,(i)}\right|$ is smaller than a user specified tolerance parameter. The norm is calculated as follows

12

$$\left|\phi_{cor}^{(i)}\right| = \frac{1}{KK\,JJ} \sum_{j,k=1}^{JJ,KK} \frac{\left|Y_{k,j}^{n+1,(i+1)} - Y_{k,j}^{n+1,(i)}\right|}{\left|Y_{k,max}^{n+1,(i+1)} - Y_{k,min}^{n+1,(i+1)}\right|} +$$

$$\frac{1}{JJ} \sum_{j=1}^{JJ} \frac{\left|T_j^{n+1,(i+1)} - T_j^{n+1,(i)}\right|}{\left|T_{max}^{n+1,(i+1)} - T_{min}^{n+1,(i+1)}\right|} +$$

$$\frac{1}{JJ} \sum_{j=1}^{JJ} \frac{\left|U_j^{n+1,(i+1)} - Y_j^{n+1,(i)}\right|}{\left|U_{max}^{n+1,(i+1)} - Y_{min}^{n+1,(i+1)}\right|} \ .$$

For every time step, a single iteration was often sufficient for convergence. In *USEF* , in the case of two jet configuration, once the profiles of chemical species, temperature and *U*- velocity are obtained at the *(n+1)* time layer, the mass flux is calculated by integrating the continuity equation

$$\frac{\partial \rho}{\partial t} + \rho U \varepsilon + \frac{\partial V}{\partial y} = 0$$

from the stagnation point $y = 0$, where $V = 0$, to the left- and right- hand boundaries of the computational domain. The $\partial V / \partial y$ derivative is approximated by an upwind scheme

$$\frac{V_{j+1}^{n+1} - V_j^{n+1}}{h_j} + \left(\frac{\partial \rho}{\partial t} + \rho U \varepsilon \right)_{j+1/2}^{n+1} = 0 , \ y > 0$$

$$\frac{V_j^{n+1} - V_{j-1}^{n+1}}{h_{j-1}} + \left(\frac{\partial \rho}{\partial t} + \rho U \varepsilon \right)_{j-1/2}^{n+1} = 0 , \ y \leq 0$$

13

In the Tsuji flame configuration the continuity equation is integrated from the burner surface, y_w, where the value of V_w is known, to infinity. In *UniSEF* , only the temperature and species equations are solved and no integration of the continuity equation is required.

After the complete solution vector is obtained in both models, the computational mesh is adapted following a procedure described in detail in Ref. [16]. At every time step the thermal thickness of the flame is compared with the distance from the flame to the upstream and downstream boundaries of the computational domain. If either of these distances is smaller than two flame thickness, the computational domain is regridded by moving the boundaries away from the flame. The time step of the calculations is taken to be the minimum of the characteristic time scales of species production and is bounded to be lower than 1.0e-06 s.

IV *Results and Discussion*

In Fig. 3 the steady state structures of an atmospheric pressure, stoichiometric, diffusion, methane-air flame with a strain rate $\varepsilon_{+\infty} = 100$ 1/s in the Tsuji configuration obtained using *USEF* (solid lines) and a phase-space, pseudo-arc-length continuation method [10] (dashed lines) are compared. The same chemical kinetics and transport models are used in both simulations. The profiles of species and temperature are shown as a function of the mixture fraction, Z, defined as a solution of the mixture fraction transport equation

$$\rho \frac{\partial Z}{\partial t} + V \frac{\partial Z}{\partial y} - \frac{\partial}{\partial y}\left(\frac{\lambda}{c_p}\frac{\partial Z}{\partial y}\right) = 0 \quad , \tag{34}$$

where the mixture fraction is equal to unity on the oxidizer side and to zero on the fuel side. We observe an excellent agreement in terms of the shapes, locations and peak values of the temperature and chemical species. Some discrepancies in the CH_4 profile around $Z = 0.07$ are enhanced by

14

the choice of the mixture fraction as an independent variable and, probably, due to a high numerical diffusion of the upwind discretization scheme applied in some grid points of our computational domain.

The above test run serve to demonstrate that the *USEF* model is capable of predicting accurately the steady state structure of strained flame and that it can be used as a benchmark solution for a comparison with the simplified, uniform strain *UniSEF* model.

Comparison of USEF and UniSEF

The *USEF* and *UniSEF* models are compared in terms of the transient dynamics and steady state premixed and diffusion flame structures. In this paper an atmospheric pressure, premixed flame with a strain rate $\varepsilon_{+\infty} = 1000$ 1/s and an atmospheric pressure, diffusion flame with a strain rate $\varepsilon_{+\infty} = 200$ 1/s are used as examples. In both test cases, the flames are simulated in the two jet configuration and their steady state structures are shown in Figs. 7 and 8, respectively.

Before we compare the transient dynamics and steady state structures of *USEF* and *UniSEF*, it is worthwhile to understand how the assumption of uniform strain affects the velocity and mass flux fields in both flames. Fig. 4 shows steady state heat release, mass flux and y-velocity profiles obtained using both solutions in the premixed flame case. Fig. 5 shows the same profiles in the diffusion flame. In both figures all *UniSEF* profiles are drawn by dashed lines, *USEF* profiles - by solid lines. We note that near the peak values of the heat release rate profiles the mass flux and y-velocity profiles of the exact and simplified solution are very close. This is due to the choice of the uniform strain (see Eq. (23)) as the exact strain inside the reaction zone. Combustion inside the reaction zone in *UniSEF* occurs at almost the same conditions as in *USEF*. In the next section we will see that, although outside the reaction zone the mass flux and velocity profiles of the two solutions differ significantly, their closeness inside the zone leads to a very good agreement in terms of the transient dynamics and steady state structures.

Premixed Flame

We start the comparison of the models with the premixed flame. Both solutions are initiated with identical arbitrary profiles of the dependent variables constructed from the hyperbolic tangent and bell-shaped exponential functions or a combination of both. The values of the variables far behind the flame on the products are set equal to the equilibrium values for a given pressure and chemical kinetics mechanism. The peak values of radical profiles are of the order of typical values encountered in premixed methane-air flames. The initial thickness of all profiles is 6 mm, the initial location of flame, defined as the location of the maximum fuel consumption, is 1 mm from the stagnation point. The chemical kinetics and transport models of Ref. [10] are used in all simulations. At time $t = 0$ s. the initial profiles are introduced into the models and the strain rate $\varepsilon_{+\,\infty}$ is instantaneously put equal to 1000 1/s.

In Fig. 6a the *USEF* time histories of the burning velocity and flame location are shown by lines with empty symbols, the *UniSEF* time histories - by lines with solid symbols. Fig. 6a demonstrates virtually identical time response of *USEF* and *UniSEF* to a step-wise change in the strain rate. This figure clearly show that the transient response of a premixed flame can be modeled using *UniSEF* . In the case considered, the methane-air premixed flame response time of $O (10^{-3})$ s. This could be several times higher than a typical time step in a turbulent flow making the quasi - steady assumption invalid. A comparison of the quasi-steady approximation and the transient approach is made later in the paper using the diffusion flame case as an example.

The steady state profiles of temperature and major species produced by *USEF* (solid line) and *UniSEF* (dashed line) for the same flame are compared in Fig 7. The shapes of the temperature, major and minor species profiles are virtually identical, although the location of the *UniSEF* flame is further from the stagnation point than that of the *USEF* solution due to a much lower absolute value of the uniform strain on the products side which dominates over a somewhat higher value of the strain on the reactants side (see Fig. 2a) . Peak values of radicals also agree well.

We conclude that in the case of the premixed flame the uniform strain *UniSEF* model produces the steady state flame structure and time response which agree well with the results of the exact *USEF* model.

Diffusion Flame

The same two approaches are used to study the structure and the time response of a diffusion flame subjected to a strain $\varepsilon_{+\infty}$ of 200 1/s. Again, both simulations start with the same set of arbitrary bell-shaped profiles of the thickness of 6 mm and the peak locations of 1 mm. The ignition of the diffusion flame is achieved by introducing peak *H, OH* and *O* concentrations which are an order of magnitude higher than the typical values encountered in methane-air diffusion flames. The time responses are compared in Fig. 6b. The burning rate in the case of a diffusion flame is normalized in such a way that it has the dimensions of velocity in order to use the same characteristic of combustion rate in both premixed and diffusion flame cases:

$$\left| \frac{\int_{-\infty}^{+\infty} \dot{\omega}_{fuel}\, W_{fuel}\, dy}{\rho_{+\infty}\, (Y_{fuel,\, +\infty} - Y_{fuel,\, -\infty})} \right|.$$

The response times, steady state flame locations and burning velocities of the solutions agree quite well. The response time of the diffusion flame is again $O(10^{-3})$ s.

In Fig. 9 comparison of the quasi-steady and the transient approaches is shown in terms of the burning velocity. The applied strain as a function of time is also shown, representing four global flow simulation time steps of 10^{-3} seconds each. The initial strain of 100 1/s is applied at time 0 which, after a time step of 10^{-3} second, is changed to 200, 400 and, finally, to 50 1/s. At time t = 0 the steady state profiles corresponding to a strain of 100 1/s are introduced into *USEF* . During the initial flow time step, when the strain is 100 1/s, the burning velocity remains

17

unchanged. At time $2 \cdot 10^{-3}$ s., the external strain is changed and the flame structure starts to evolve. Since the flame response time is much larger than the flow time scale, the burning velocity does not have enough time to reach a steady state value of 1.02 cm/ s corresponding to the strain of 200 1/s. At the time for the next strain change, flame is still unsteady, lagging behind the quasi-steady value. In Fig. 8 we demonstrate that the quasi-steady assumption can produce significant errors in the burning rate predictions.

A comparison of the steady-state profiles of the temperature and species mass fractions is shown in Fig. 8. In the case of a diffusion flame the overall flame structure produced by *UniSEF* agrees well with that of *USEF*.

In a numerical simulation of complex chemistry most of the computation time is spend on the evaluation of the chemical source terms. Elimination of the momentum and continuity equations from *UniSEF* is of little value until the total number of chemical species is substantially reduced. Peters and Kee [17] proposed a systematically reduced four-step mechanism which is able to provide the essential properties of methane-air diffusion and premixed flames. This mechanism makes use of 7 so called "non-steady" species, namely *CH4, O2, CO2, CO, H2, H2O*, and *H* instead of the total of 16 species of the "starting" mechanism. The other species are assumed to be in equilibrium and various algebraic equilibrium equations are used to evaluate their concentrations in terms of the concentrations of "non-steady" species.

Incorporation of the reduced chemical kinetics into *UniSEF* can potentially provide a numerically efficient and robust model of elemental flame for turbulent combustion simulation. However, several questions remain to be answered. First, how the rather crude *UniSEF* assumption of uniform strain across the flame affects the S-curve and, in particular, the value of the extinction strain. Second, how close are the transient responses of the exact solution and *UniSEF* with reduced kinetics to a rapid change in strain. In the following we will answer the first question and make some comments on the second.

In Fig. 10 the traditional S-curve for an atmospheric pressure methane-air diffusion flame obtained using *UniSEF* with reduced chemistry (solid line), exact solution with full chemistry

[17] (dashed line with squares), and exact solution with reduced chemistry [17] (dashed line with circles) is shown. The overall agreement between the exact solutions and *UniSEF* is satisfactory in the whole range strains. The extinction strains for *UniSEF* is around 300 1/s, for exact solution - 352 1/s, and for exact solution with reduced chemistry - 400 1/s. Thus, *UniSEF* with reduced chemistry provides extinction strain values which are as different from the exact values as the values of any solution employing reduced chemistry.

As far as the unsteady responses of *USEF* and *UniSEF* with reduced chemistry is concerned, our preliminary results indicate that they are very close to the corresponding responses of the models with the "starting" mechanism. This is rather surprising since, as it is mentioned by Peters in Ref. [18], in the highly unsteady initial stages of premixed and diffusion combustion the steady state assumptions of the reduction strategy are grossly violated. We plan to address this question in the nearest future.

Conclusions

Two approaches were developed to study the structure and dynamic characteristics of complex chemistry, strained, premixed and diffusion flames and for the purpose of using them as elemental flame submodels in turbulent combustion simulation. In the exact flame solution the unsteady temperature, mass fractions, continuity and momentum equations are solved using an implicit time - integration scheme. In the simplified, uniform strain model the governing equations are reduced to the reaction-diffusion equations potentially providing a more robust solution procedure and reducing the number of governing equations by two. Since the actual strain varies inside the flame from ε_{max} to ε_{min}, the average of these values is proposed to serve as the uniform strain in the model. For a premixed and diffusion flame, this assumption provides a remarkable agreement in the time responses and the steady state flame structures of the uniform strain and exact solutions. Incorporation of the Peters reduced chemistry mechanism [17] into the model allows to take the full advantage of the reduced number of *UniSEF* governing equations and to obtain the extinction strain and S-curve which are satisfactorily close to the exact values.

Using the response of the diffusion flame to strain as an example, we demonstrate that the application of the quasi-steady assumption, when the instantaneous value of the burning velocity correspond to the instantaneous value of local strain, can potentially lead to significant errors since the flame response time might be larger than the flow calculation time step which determines the time interval between the strain changes.

References

1. Peters, N., " Laminar Flamelet Concepts in Turbulent Combustion ," *Twenty-first Symposium (International) on Combustion*, The Combustion Institute, 1986.

2. Petrov, C. and Ghoniem, A.F. , " An Unsteady Strained Flame Model for Turbulent Combustion Simulations", *AIAA - 94 - 0776*, 32-nd Aerospace Sciences Meeting & Exhibit, January 10-13, 1994, Reno, NV.

3. Petrov, C. and Ghoniem, A.F. , " An Unsteady Strained Flame Solution with Multi-Step Chemical Kinetics for Turbulent Combustion Simulations," *AIAA - 95 - 0380*, 33-nd Aerospace Sciences Meeting & Exhibit, January 9-12, 1995, Reno, NV.

4. Petrov, C. And Ghoniem, A.F. " ", *Comb. Flame*, Vol. **104**, 1995.

5. Takeo Saitoh and Yoshiro Otsuka, " Unsteady Behavior of Diffusion Flames and Premixed for Counter Flow Geometry," *Combustion Science and Technology*, Vol. **12**, 1976.

6. Ghoniam, A., Soteriou, M., Knio, O., Cetegen, B., " Effect of Steady and Periodic Strain on Unsteady Flamelet Combustion, "," *Twenty-fourth Symposimum (International) on Combustion*, The Combustion Institute, 1992.

7. Cetegen, B., Bogue " "

8. Stahl, G., Warnatz, J., " Numerical Investigation of Time-Dependent Properties and Extinction of Strained Methane- and Propane-Air Flamelets ," *Comb. Flame*, Vol. **85**, 1991.

9. Rogg, B., Peters, N., "Reduced Kinetics Mechanisms for Applications in Combustion Systems," *Lecture Notes in Physics* , **m15**, 1993.

10. Smooke, M.D. - " Reduced Kinetics Mechanisms and Asymptotic Approximations for Methane - Air Flames ", *Lecture Notes in Physics*, **384**, 1990.

11. Rogg, B., ". Response and Flamelet Structure of Stretched Premixed Methane-Air Flames,"*Comb. Flame*, **73**, 1988.

12. Carrier, G.F., Fendell, F.E. and Marble, F.E., " The Effect of Strain on Diffusion Flames, " *SIAM J. Appl. Math*, **28**, 463, 1975.

13. Rutland and Ferziger, "Unsteady Strained Premixed Laminar Flames", *Comb. Sci. Tech.*, **73**, 305, 1990.

14. 8. Kee, R.J., Dixon-Lewis, G., Warnatz, J., Coltrin, M.E., Miller, J.A., " A FORTRAN Computer Code package for the Evaluation of Gas-Phase Multicomponent Transport Properties ", SANDIA Report *SAND86-8246*, 1986.

15. Anderson, D.A., Tannehill, J.C. and Pletcher, R.H., "Computational Fluid Mechanics and Heat Transfer , " *Series in Computational Methods in Mechanics and Thermal Sciences* , Hemisphere Publishing Corporation, 1984.

16. Kee, R.J., Grcar, J.F., Smooke, M.D., Miller, J.A., " A Fortran Program for Solutioning Steady Laminar One-Dimensional Premixed Flames," *SANDIA Report SAND85-8240*, 1985.

17. Peters, N. and Kee, R.J., " The Computation of Streched Laminar Methane -Air Diffusion Flames Using a Reduced Four-Step Mechanism," *Comb. Flame,* **68**, pp. 17-29, 1987.

18. Peters, N "," *Lecture Notes in Physics*, **384**, 1990.

Figure 1. Two jet premixed/ diffusion and Tsuji diffusion flame configurations in a stagnation point flow.

Figure 2. The choice of effective uniform strain as the exact strain inside the reaction zone. *USEF* steady state temperature, strain and heat release rate profiles in the premixed (strain = 1000 1/s) and diffusion (strain = 100 1/s) stoichiometric, atmospheric pressure flames.

Figure 3. A comparison of steady state (a) temperature, major and (b) minor species profiles for an atmospheric pressure, diffusion, stoichiometric, methane-air flame using the *USEF* model (solid lines) and arclength continuation method (Smooke, Ref. [10], dashed line); strain rate = 100 1/s, chemical kinetics mechanism of Ref. [10], Tsuji flame configuration.

Figure 4. A comparison of (a) steady state heat release and mass flux profiles and (b) steady state heat release and y-velocity profiles for an atmospheric pressure, premixed, stoichiometric, methane-air flame using the *USEF* model (solid lines) and the *UniSEF* method (dashed line); strain rate = 1000 1/s, chemical kinetics mechanism of Ref. [10], two jet flame configuration.

Figure 5. A comparison of (a) steady state heat release and mass flux profiles and (b) steady state heat release and y-velocity profiles for an atmospheric pressure, diffusion, stoichiometric, methane-air flame using the *USEF* model (solid lines) and the *UniSEF* method (dashed line); strain rate = 200 1/s, chemical kinetics mechanism of Ref. [10], two jet flame configuration.

Figure 6. A comparison of time histories of (a) the burning velocity employing *USEF* (empty symbols) and *UniSEF* (solid symbols) models for an atmospheric pressure, premixed, stoichiometric, methane-air flame; strain rate = 1000 1/s, and (b) the burning velocity employing *USEF* (empty symbols) and *UniSEF* (solid symbols) models for an atmospheric pressure,

diffusion, stoichiometric, methane-air flame; strain rate = 200 1/s; chemical kinetics mechanism of Ref. [10], two jet flame configuration.

Figure 7. Calculated (a) temperature, major and (b) minor species profiles for an atmospheric pressure, premixed, stoichiometric, methane-air flame using the uniform strain *UniSEF* model (dashed) and the exact *USEF* model (solid); strain rate= 1000 1/s, chemical kinetics mechanism of Ref. [10], two jet flame configuration.

Figure 8. Calculated steady state (a) temperature, major and (b) minor species profiles for an atmospheric pressure, diffusion, stoichiometric, methane-air flame using the uniform strain *UniSEF* model (dashed lines) and the exact *USEF* solution (solid line); strain rate= 200 1/s, chemical kinetics mechanism of Ref. [10], two jet flame configuration.

Figure 9. A comparison of the transient solution obtained using *USEF* and the quasi-steady solution for an atmospheric pressure, diffusion, stoichiometric, methane-air flame; chemical kinetics mechanism of Ref. [10], two jet flame configuration; the strain history given at the bottom of the figure.

Figure 10. Calculated maximum steady state flame temperature as a function of the inverse of strain for an atmospheric pressure, diffusion, stoichiometric, methane-air flame using the uniform strain *UniSEF* model with reduced chemistry (solid line), the exact solution with starting chemistry [17] (dashed line, squares), and the exact solution with reduced chemistry [17] (dashed line, circles); Tsuji flame configuration.

Figure 1   (a)   (b)   (a)   (b)   (a)   (b)   (a)   (b)   (a)   (b)   (a)

Figure 2

Figure 3

Figure 4

Figure 5

Figure 6

Figure 7

Figure 8

Figure 9

While in a number of papers the reduced chemistry approach is proven to produce good results for the cases of steady state diffusion and unstrained premixed flames, we are unaware of any piblication where the method is applied to study the *unsteady* strained premixed and diffusion flames. This is very unfortunate since the application of it can be potentially very helpful in the simualtion of elementary flame in turbulent combustion. The reason for the absence of the unsteady applications of the method is that, strictly speaking, in the highly unsteady initial stages of premixed and diffusion combustion its steady state assumptions are violated. Different chemical reactions are important at that time. This is mentioned by Peters in Ref. [18].

Premixed Flame, two jet configuration

x

Flame

Products

$u_{+\infty} = \varepsilon_{+\infty} x$

streamlines

y

Reactants

(a)
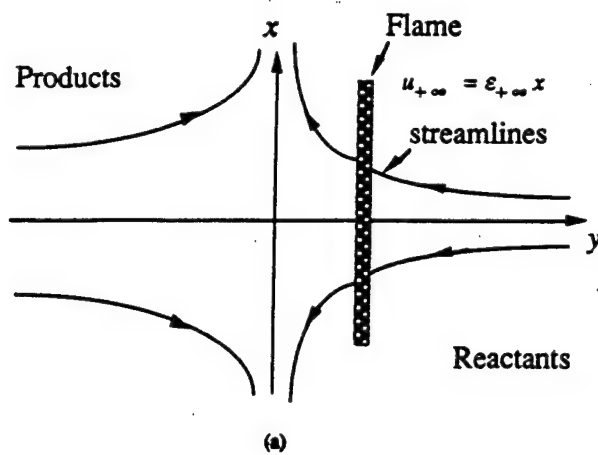
Diffusion Flame, two jet configuration

x

Flame

Fuel

$u_{+\infty} = \varepsilon_{+\infty} x$

streamlines

Air

(b)
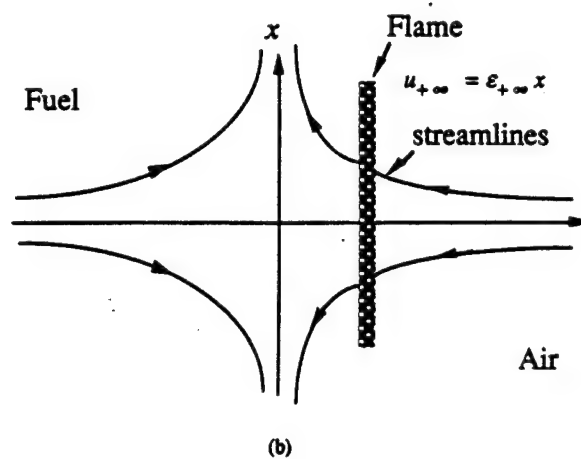
Diffusion Flame, Tsuji configuration

x

Flame

$u_{+\infty} = \varepsilon_{+\infty} x$

streamlines

Fuel

x

V_w

y

free stagnation
point

Air

(c)

Figure 1

Premixed Flame, strain rate = 1000 1/s

(a)

Diffusion Flame, strain rate = 100 1/s
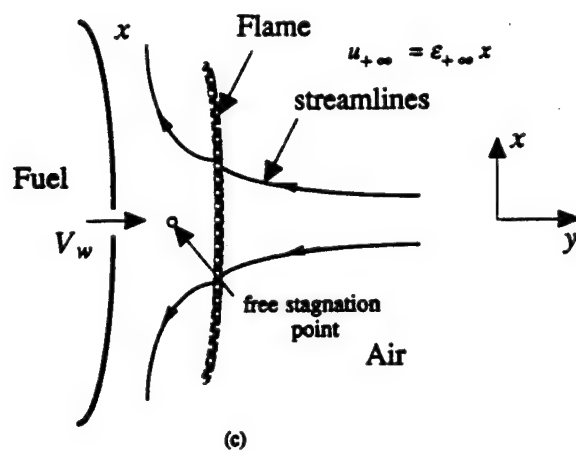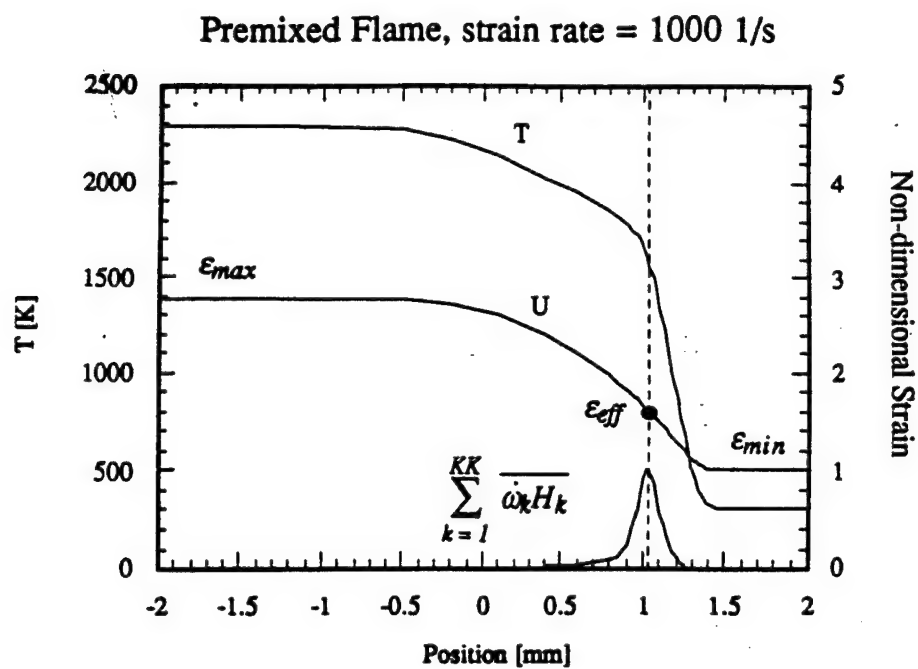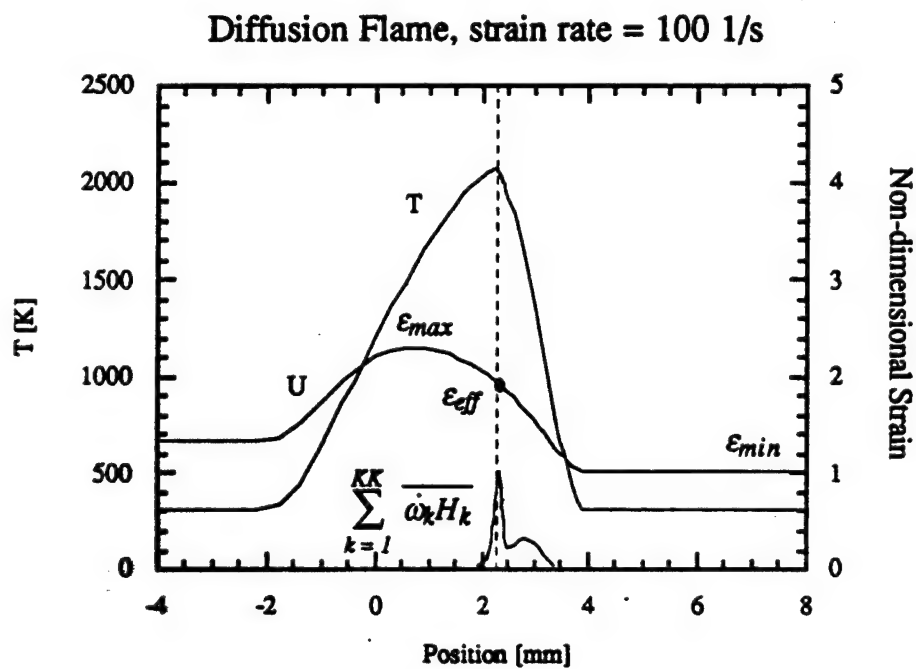
(b)

Figure 2

Major Species Profiles

(a)

Minor Species Profiles

(b)
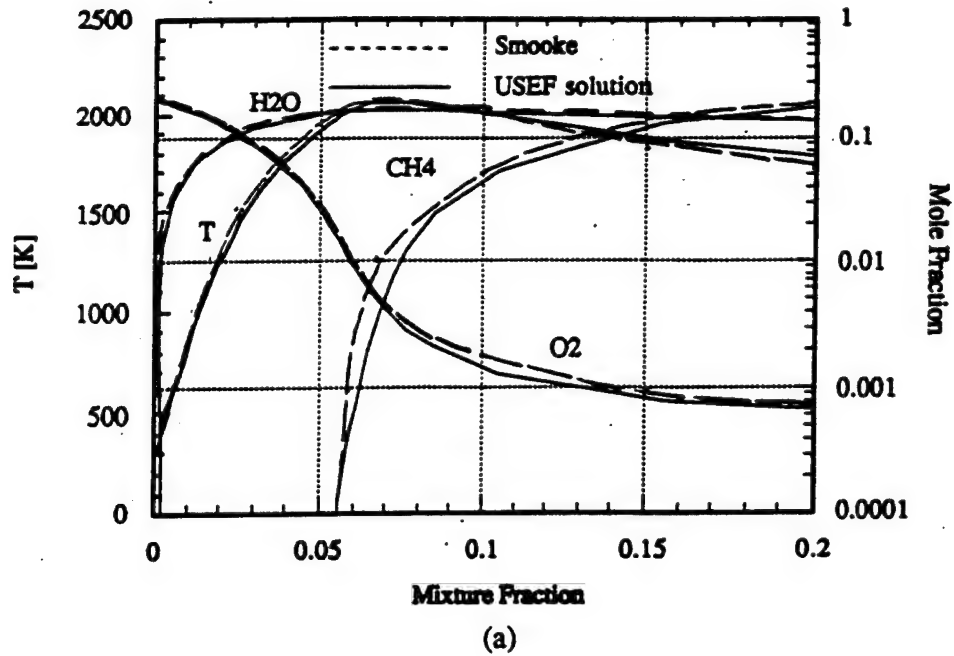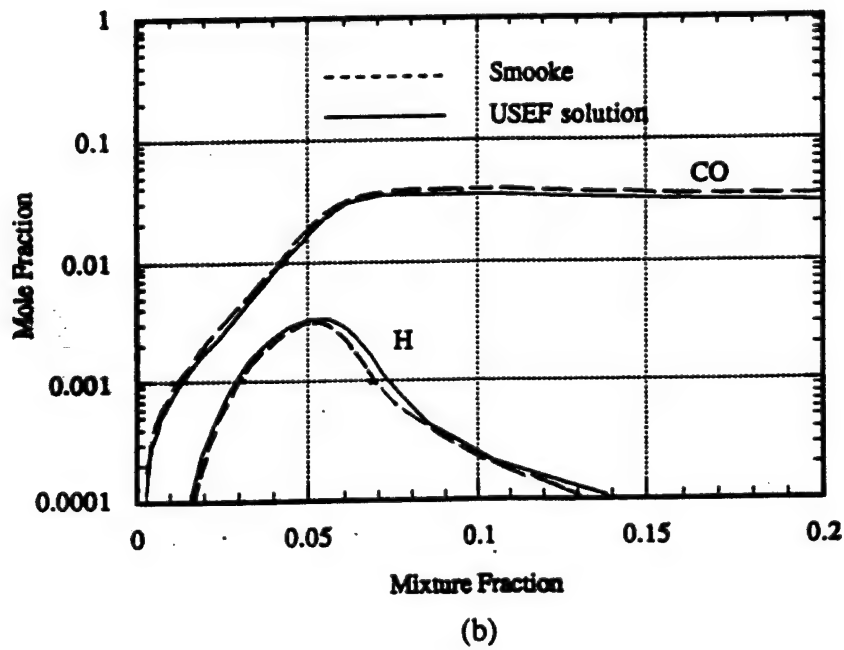
Figure 3

Premixed Flame, eps = 1000 1/s

(a)

(b)
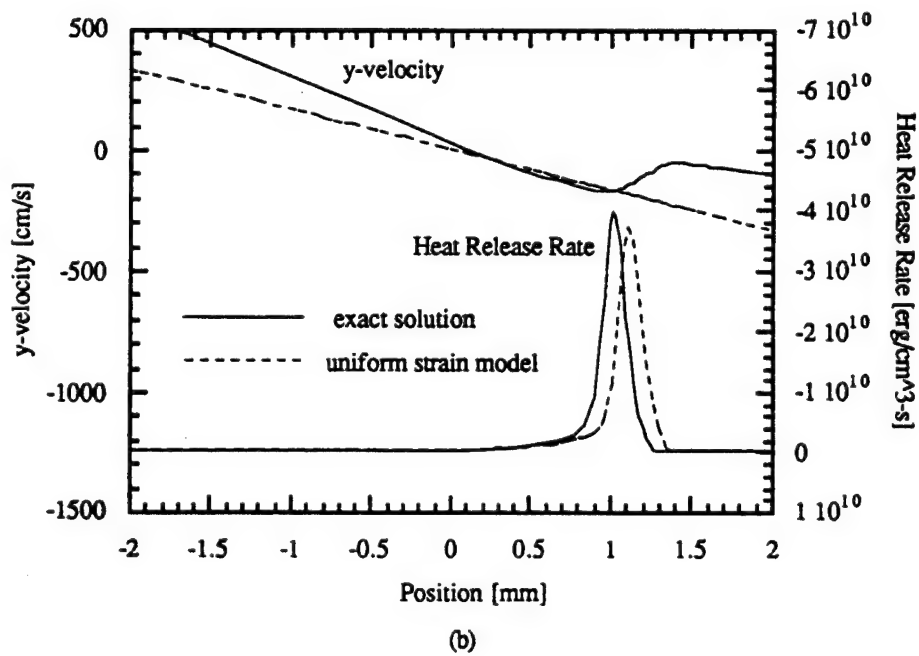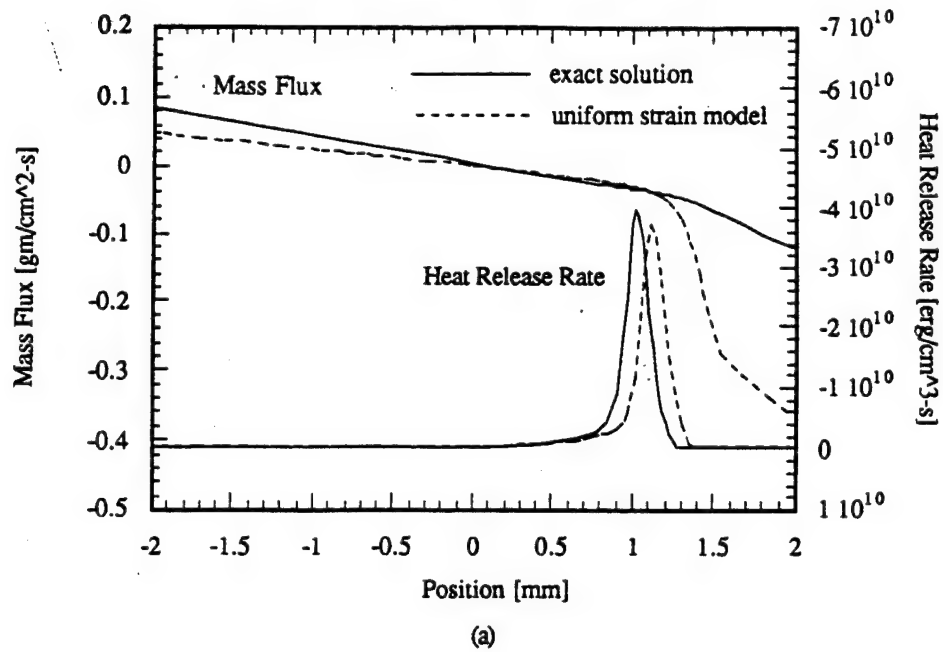
Figure 4

Diffusion Flame, eps = 200 1/s
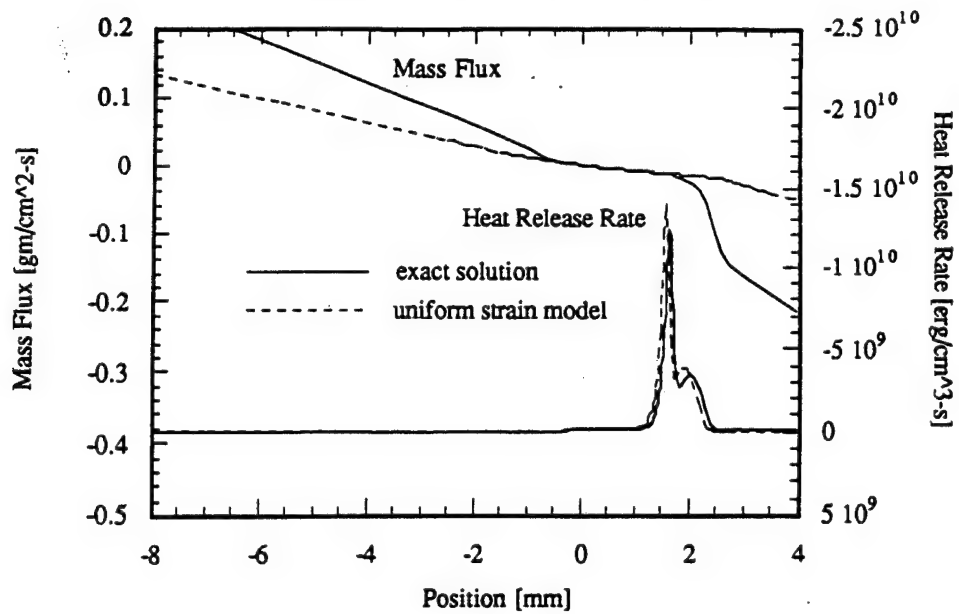
(a)
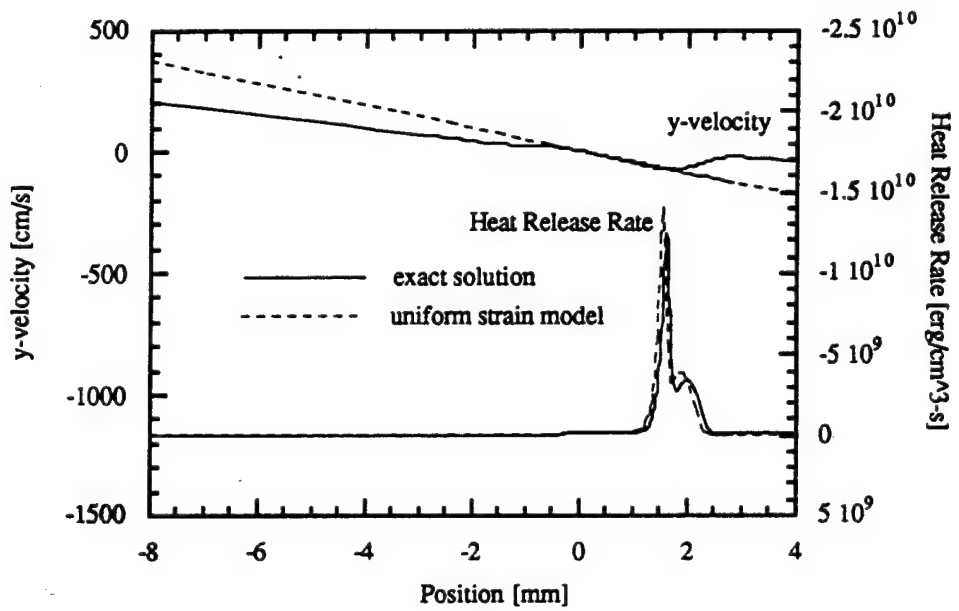
(b)

Figure 5

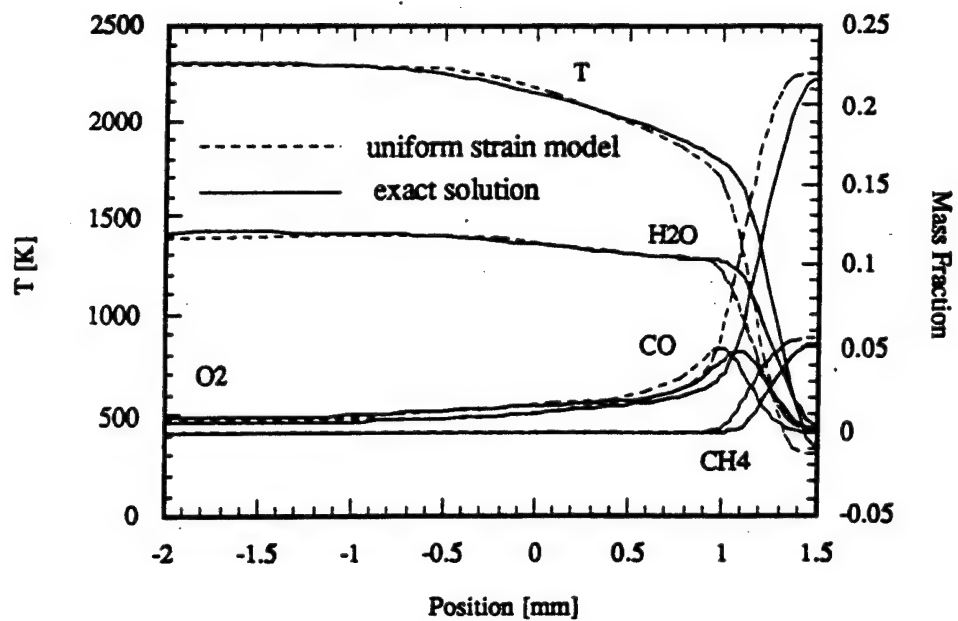# TRANSIENT RESPONSE

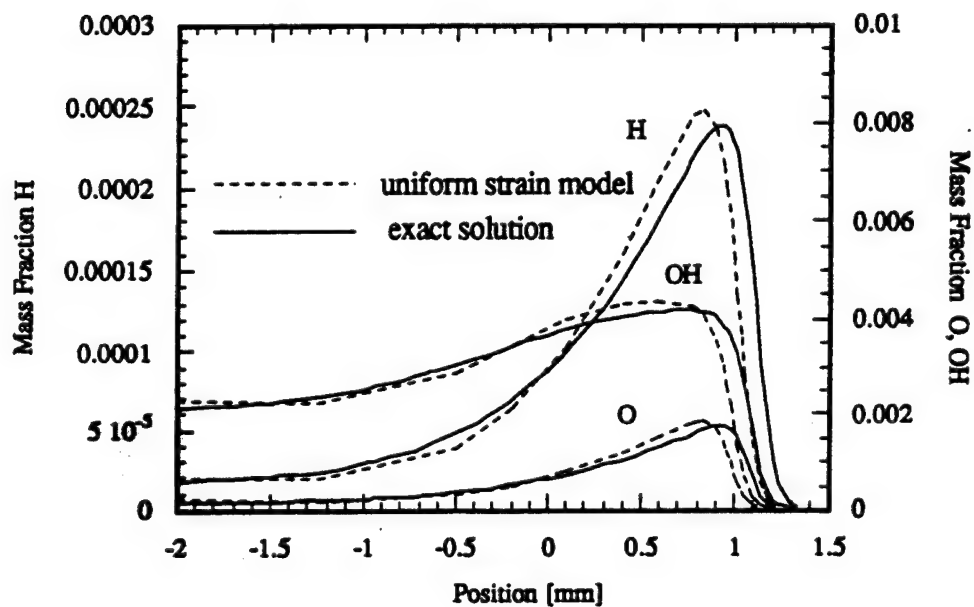### Premixed Flame, eps = 1000 1/s
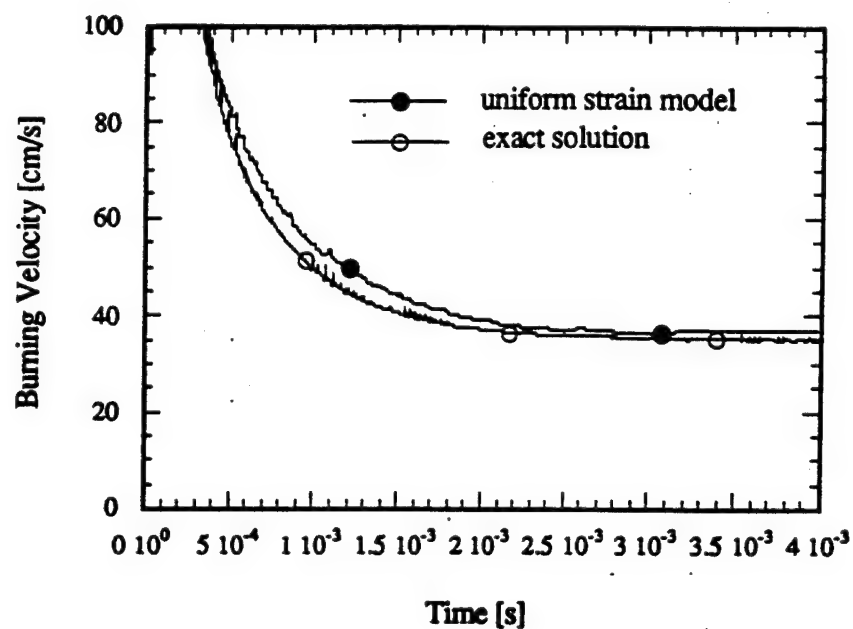
Diffusion Flame, eps = 200 1/s
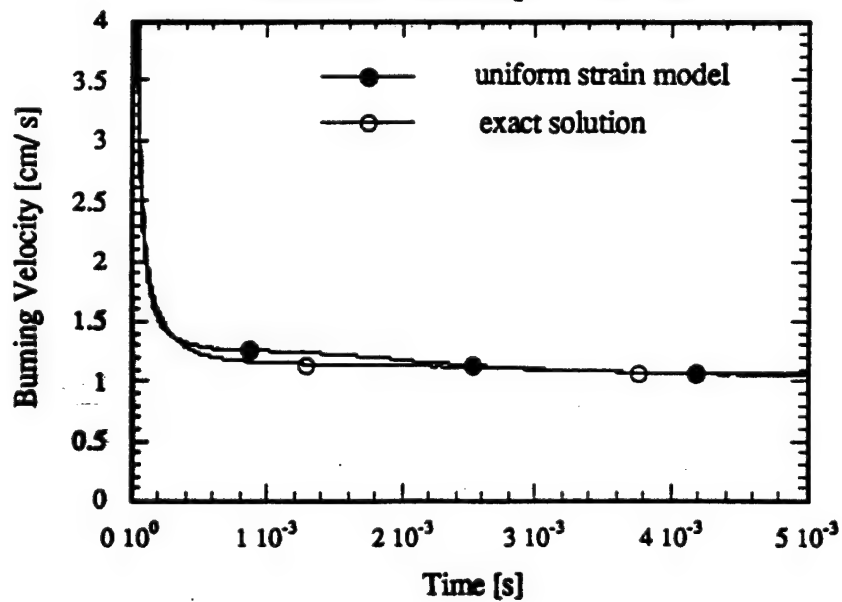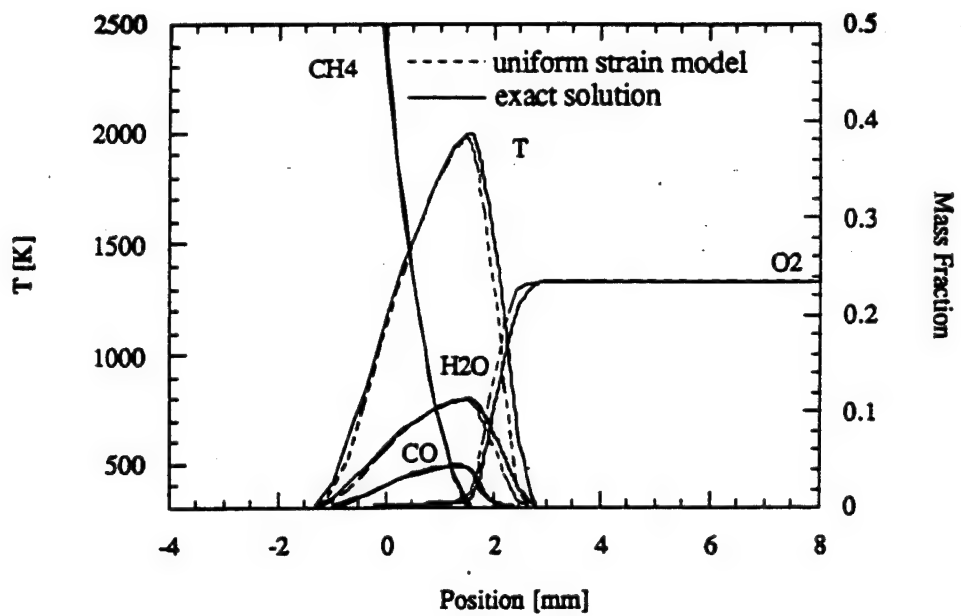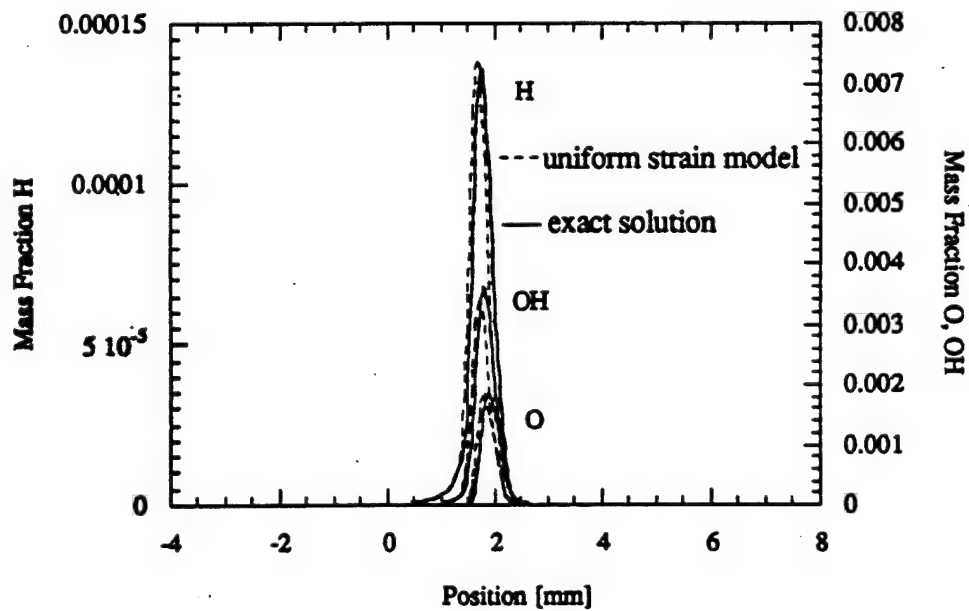

(b)

Figure 6

(a)

(b)
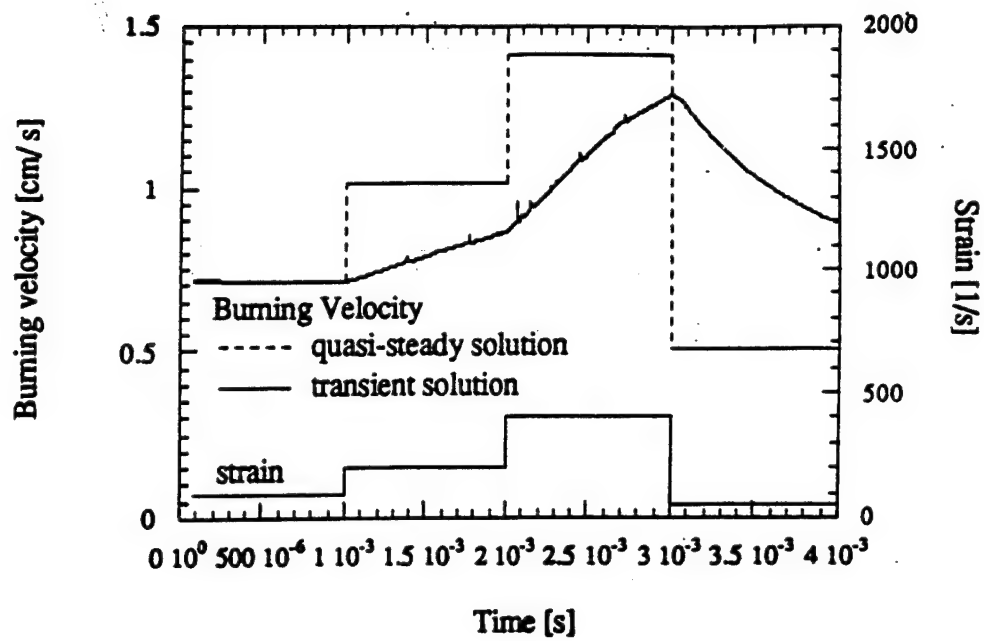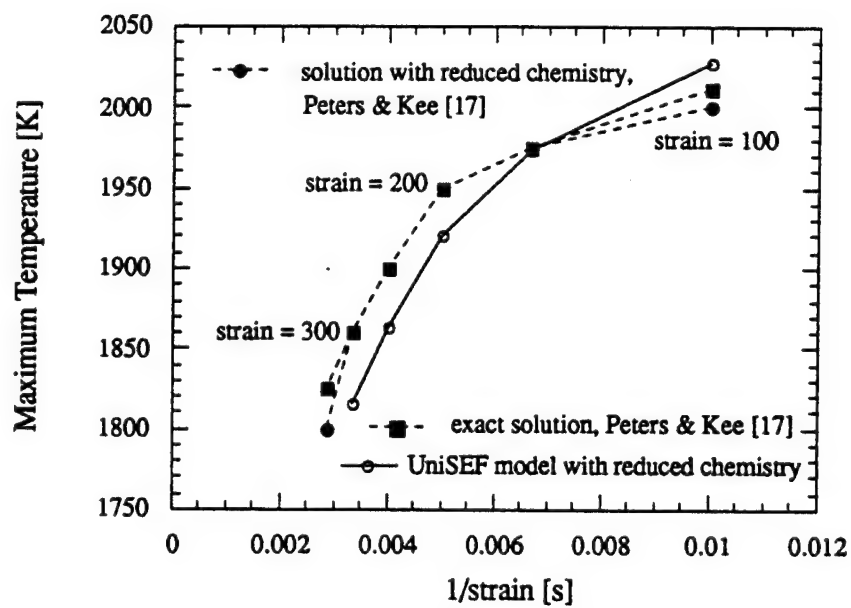
Figure 7

(a)

(b)

Figure 8

Figure 9

Figure 10

APPENDIX IV

NUMERICAL SIMULATION OF UNSTEADY COMBUSTION USING THE TRANSPORT ELEMENT METHOD

Marios C. Soteriou* and Ahmed F. Ghoniem

Department of Mechanical Engineering
Massachusetts Institute of Technology
Cambridge, MA 02139

ABSTRACT

The transport element method is described and implemented in the simulation of the non-premixed reacting shear layer. The method, a natural extention of the vortex element method, resolves the variable density flow at low Mach number and the exothermic reacting field. The effect of combustion on the flow is accommodated by incorporating a volumetric expansion velocity component and by modifying the integration of the vorticity equation to include expansion-related and baroclinic terms. The reacting field equations describing a single step, irreversible, chemical reaction, are simplified by the introduction of Shvab-Zeldovich (SZ) conserved scalars whose transport is sufficient to compute the evolution of combustion in the case of infinite reaction rate. In the case of finite rate chemistry the evolution of one primitive scalar, the product mass-fraction, is also computed. The vorticity, conserved scalar gradient and product mass fraction are discretized amongst fields of transport elements. Their time evolution is implemented by advecting the elements at the local velocity while simultaneously integrating their transport equations along particle trajectories. The integration of the vorticity and the conserved scalar gradient equations is simplified using ideas from kinematics. A novel core expansion scheme that avoids the problems associated with the conventional implementation is used to simulate diffusion. Field quantities are obtained using convolutions over the elements. Results indicate that the method is able to accurately reproduce the essential features of the flow. Convergence of the solution in time is approximately linear. Moreover, the finite reaction rate solution at low Karlovitz number bear strong similarities to that of the infinite reaction rate model. This similarity is exploited in validating the part of the numerical methodology related to the integration of the product mass-fraction equation.

---

* Current address: Department of Mechanical Engineering, University of Connecticut, Storrs, CT06269-3139

I. INTRODUCTION

Generalization of the vortex element method (VEM) [1] by incorporating the physics of scalar transport, mixing and reaction; what we have called the transport element method (TEM), has been an ongoing effort since its inception [2-9]. The essential features of this process; the discretization of primitive variable gradients, their Lagrangian transport and use of flow kinematics to monitor their evolution, offer significant advantages in the simulation of reacting flows. The simulation of reacting flows involve substantial complexities. These include the presence and continuous mixing of many species, the evolution of temporal and spatial scales which cover several decades, the presence of strongly non-linear and coupled phenomena and the coupling of the combustion energy release and the associated changes in the density and transport properties and the flow. The latter requires the modification of VEM which in its basic form deals with incompressible uniform density flow. Moreover reacting flows are characterized by thin reaction fronts, i.e. regions of sharp scalar gradients, which evolve in a highly convoluted manner.

Early attempts to simulate reacting flows using a VEM-based approach simplified the reacting field through the use of flame sheet models. In these [2] and [3], the sharpness of the flame front was exploited to represent it as a sheet which encompasses the reaction and diffusion regions of the flame and separates unmixed scalars. The effects of combustion on the flow were restricted to those associated with the volumetric expansion by distributing volumetric sources along the flame sheet.

To move beyond these simplified models, one needs a detailed description of the mixing field as a first step in the accurate representation of the reacting field. This was accomplished by the development of the Transport Element Method (TEM) in two [4] and three dimensions [5-7]. The TEM bears substantial similarities to the VEM to which it is fully compatible. Essentially, it discretizes the scalar-gradients and evolves them by using information from the kinematics of material lines. The scalars are obtained from the gradients via convolutions over their fields. A version of the TEM incorporating reaction in a two-dimensional temporally evolving flow was also proposed [7][1]. Its implementation, however, in the spatially developing model of the flow is not, in general, possible. The reason for this lies in the temporal model, which due to its utilization of periodic boundary conditions represents a mathematical idealization of the flow it attempts to represent[2] . The

---

[1] A three dimensional scheme was also proposed [8,9] but one in which the scalar-gradient approach was abandoned in favor of a primitive scalar one and temperature independent kinetics was assumed.

[2] The limitations of the temporal model in the simulation of reacting flows exceed those for the non-reacting flow which have been pointed out previously [10]. By constuction, the temporal model is valid only for very small and very large values of the Karlovitz number. The first, represents very fast combustion characterized by thin continuous flames, while for the second, gaseous fuel combustion is

2

TEM as presented in Ref.[7] takes full advantage of the simplifications offered by the temporal model and, as a result, cannot be applied in spatially developing flows.

In this work, we present a new version of TEM which is applicable to spatially developing flows. Through the introduction of SZ variables, the method is able to use a combination of scalar-gradients and a primitive scalar to completely describe the reacting field. Combustion energy release effects on the flow, at low Mach number, are captured using the variable density version of the VEM.

II. FORMULATION

A two-dimensional flow is considered. Compressibility effects are restricted to the low Mach-number limit. Combustion follows a single-step reaction which consumes two reactants, one from each stream, to form a single product according to a singe step Arrhenius mechanism. All species behave as perfect gases with equal molecular weights and equal and constant specific heats and mass diffusivities. The Lewis number is equal to unity and molecular diffusion is relatively small, i.e., the flow is at high Reynolds and Peclet numbers[3] . Accordingly, the non-dimensionalized governing equations are:

$$\frac{d\rho}{dt} + \rho \nabla \cdot \mathbf{u} = 0 ; \tag{1}$$

$$\frac{d\mathbf{u}}{dt} = -\frac{\nabla p}{\rho} + \frac{1}{Re} \nabla^2 \mathbf{u} ; \tag{2}$$

$$\frac{ds_j}{dt} = \frac{1}{Pe} \nabla^2 s_j + Q_j \frac{\dot{w}}{\rho} \tag{3}$$

with

j	1	2	3	4(+)
s_j	T	Y_f	Y_o	Y_p
Q_j	Q_o	-1	$-\phi$	$1+\phi$

---

unsustainable. Irrespective of the numerical method used, the model's implementation to flows of moderate Karlovitz number in which interaction of the flow and reaction time scales is experienced and sharply transient phenomena such as quenhing, and re-ignition take place is problematic.

[3] Most of the assumptions related to the reaction model are employed to reduce the computational effort and are not imposed by a fundamental limitation in the numerical scheme (Section III). An exception to this is the equal diffussivities assumption which enables the use of the Shvab-Zeldovich formulation. The diffussivities, however, do not necessarily have to be constant. Moreover, a larger number of species may be considered and the molecular masses may be unequal as long as it is assumed that the diffusivities are not similarly affected. This approach was followed in the implementation of the methodology presented herein for the simulation of the axisymmetric buoyant plume [11].

while $\rho T = 1$; $\eta_f + \phi^* \eta_o \rightarrow (1+\phi^*)\eta_p$, $Y_f + Y_o + Y_p = 1$ and $\dot{w} = A_f \rho^2 Y_f Y_o \exp(-\frac{T_a}{T})$.

In the above: $\mathbf{u} = (u,v)$ is the velocity vector in a right-handed Cartesian coordinate system $\mathbf{x} = (x,y)$, t is time, $\nabla = \left(\frac{\partial}{\partial x}, \frac{\partial}{\partial y}\right)$ is the gradient operator, $\frac{d}{dt} = \frac{\partial}{\partial t} + \mathbf{u} \cdot \nabla$ the material derivative, p is the pressure, ρ and T are the fluid mixture density and temperature respectively, subscripts f,o and p indicate the fuel, oxidizer and product, respectively, η_i denotes species i, i = f,o,p, Y_i is the mass-fraction for species i, $\dot{w}$ is the reaction rate, Re and Pe are the Reynolds and Peclet numbers, respectively, A_f, Q_o and T_a are the non-dimensionalized frequency factor, enthalpy of reaction, and activation temperature, respectively, and ϕ^* and ϕ are the molar and mass stoichiometry ratios, respectively.

The equations are transformed into vorticity-gradient form, and the velocity is decomposed into a vorticity-induced solenoidal component, $\mathbf{u}_\omega$, and two irrotational components; $\mathbf{u}_e$ due to volumetric expansion, , and $\mathbf{u}_b$ due to the boundary conditions,:

$$\mathbf{u} = \mathbf{u}_\omega + \mathbf{u}_b + \mathbf{u}_e, \tag{4}$$

$\mathbf{u}_\omega$ is obtained from the definition of the vorticity and by using a streamfunction, ψ, i.e.

$$\nabla^2 \psi = -\omega, \qquad \mathbf{u}_\omega = \nabla \times (\psi \hat{\mathbf{k}}), \tag{5}$$

where $\hat{\mathbf{k}}$ is the unit vector normal to the plain of motion. The irrotational components are obtained from the continuity equation by introducing two velocity potentials, Φ, such that

$$\nabla^2 \Phi_e = -\frac{1}{\rho}\frac{d\rho}{dt}, \qquad \mathbf{u}_e = \nabla \Phi_e \tag{6}$$

and $\qquad \nabla^2 \Phi_b = 0, \qquad \mathbf{u}_b = \nabla \Phi_b. \tag{7}$

The evolution of the vorticity is described by taking the curl of Eq.(2):

$$\frac{d\omega\hat{\mathbf{k}}}{dt} + (\nabla \cdot \mathbf{u}) \omega\hat{\mathbf{k}} = \frac{\nabla\rho \times \nabla p}{\rho^2} + \frac{1}{Re} \nabla^2 \omega\hat{\mathbf{k}}. \tag{8}$$

For the scalar transport equations, Shvab-Zeldovich (SZ) conserved variables, λ and γ, are introduced such that:

$$\lambda = Y_o - \phi Y_f, \qquad \gamma = T - \frac{Q_o}{1+\phi} Y_p. \tag{9}$$

4

These variables are constructed such that their governing equations are devoid of reaction source terms. If convection-diffusion equations have the same diffusivities and boundary conditions, a reduction of SZ equation set to a single equation can be achieved via appropriate scaling:

$$\frac{d\beta}{dt} = \frac{1}{Pe}\nabla^2\beta \ , \text{ where } \beta = \frac{\lambda - \lambda_2}{\lambda_1 - \lambda_2} = \frac{\gamma - \gamma_2}{\gamma_1 - \gamma_2} \tag{10}$$

and λ_1, λ_2, γ_1, γ_2 are the scaling values[4]

In analogy to the treatment of the flow equations, the S-Z scalar transport equation is recast into gradient form: $\mathbf{g} = \nabla\beta$

$$\frac{d\mathbf{g}}{dt} + \mathbf{g}\cdot\nabla\mathbf{u} + \mathbf{g} \times (\omega\hat{\mathbf{k}}) = \frac{1}{Pe}\nabla^2\mathbf{g} \ , \tag{11}$$

When the reaction rate is finite reactants do not coexist and the reaction zone collapses onto a line. Under these conditions the distributions of the S-Z variables provide a complete description of the reacting field *without the need for the solution of a reacting scalar*. The reaction interface is trivially established as the locus of $\lambda = 0$, while

$$\lambda \geq 0 \ : \ Y_f = 0, \quad Y_o = \lambda, \ Y_p = 1 - \lambda, \text{ and } \lambda \leq 0 \ : \ Y_f = -\frac{\lambda}{\phi}, \ Y_o = 0, \ Y_p = 1 + \frac{\lambda}{\phi}.$$

When the reaction rate is infinite, the complete description of the scalar field requires the solution of one reacting scalar, e.g., the product mass-fraction and

$$Y_f = \frac{-\lambda + (1-Y_p)}{1+\phi} \qquad Y_o = \frac{\lambda + \phi(1-Y_p)}{1+\phi} \qquad T = \gamma + \frac{Q_o}{1+\phi}Y_p$$

III. NUMERICAL SCHEME

<u>Discretization:</u> The vorticity, expansion source, $-\frac{1}{\rho}\frac{d\rho}{dt}$, β-gradient and product-mass-fraction are represented by a generic discretization function. Thus, a property ζ is discretized among a number of elements characterized by a finite area, A_i, and strength, ζ_i, locally distributed according to a radially-symmetric core function, f_δ. The discretization function is also used to reconstruct the discretized quantities at later times. In particular;

---

[4] In the case of the shear layer flow the scaling values are those of the two free streams - see Section IV. It should also be noted that when the two scaling values of a given property are equal then its field distribution is trivially reduced to a constant.

$$\zeta(\mathbf{x},t) = \sum_{i=1}^{N} \zeta_i(t) \, A_i(t) \, f_\delta(|\mathbf{x}-\chi_\iota|) \ , \tag{12}$$

where $\chi_\iota = \chi_\iota(\mathbf{x},t)$ is the element location. The core function, characterized by the core radius δ within which the most significant contribution of each element is concentrated, is a second-order Gaussian: $f_\delta(r) = \dfrac{1}{\pi\delta^2}\exp(-\dfrac{r^2}{\delta^2})$ which leads to second-order accuracy when core overlap among neighboring elements is maintained [12].

Discretization may follow one of two approaches. In the first, ς_i are found from Eq. (12). This yields high discretization accuracy at the cost that the element strengths do not necessarily have a physical meaning but are merely weights of an interpolation function. It is not, therefore, obvious that the strengths should be governed by the same transport equations as the properties they are used to represent. This is particularly the case when transport equations which involve source terms are considered.

In the second approach, $\zeta_r = \zeta(\chi_i)$. This alleviates the problem encountered in the first approach but at the cost of reduced discretization accuracy[5]. It is found, however, that if the discretized field is subsequenlty integrated, as is the case for the vorticity and the β-gradient, the error in the integrated quantity, i.e. the velocity and the scalar, respectively, is much smaller[6]. For this reason, in this work, this second approach is followed for the vorticity and the β-gradient. For the product mass-fraction, for which no integration of the solution is needed, an approach similar to the first is implemented but which does not involve the drawback mentioned. Details of this approach are given in the section dealing with the integration of the transport equations.

Calculation of the velocity and scalar fields: This essentially entails the solution of a number of Poisson and Laplace equations. For the former, Green's function based solutions are invoked, while for the latter conformal mapping techniques are implemented.

The Green's function solution of Eq.(5) for the streamfunction and the subcequent differenciation for the velocity are lumped into one step to yield a Biot-Savart convolution. Using the discrete vorticity field Eq. (12) we get

$$\mathbf{u}_\omega(\mathbf{x},t) = \sum_{i=1}^{N} \Gamma_i(t) \, \mathbf{K}_\delta(\mathbf{x}-\chi_\iota(t)) \ , \tag{13}$$

---

[5] The discretization accuracy in this case is a strong function of the overlap of the cores, generally decreasing as the overlap increases.

[6] A reduction of one order of magnitude (from about 5% to 0.1%) in the maximum pointwise discretization error was experienced between a Gaussian vorticity and the corresponding errorfunction velocity profiles.

where $\Gamma_i(t) = \omega_i(t)A_i(t)$ is the element circulation $K_\delta(x) = \overline{K}(x)\, F(\frac{r}{\delta})$, where

$$\overline{K}(x) = -\frac{(y,-x)}{2\pi r^2} \quad \text{and} \quad F(r) = 2\pi \int_0^r r\, f(r)\, dr = 1 - \exp(-r^2) .$$

A similar approach is followed in the solution of Eq.(6). The calculation of the expansion potential, like that of the streamfunction, is bypassed via a convolution which directly relates the expansion-source to the expansion velocity. A desingularized equivalent of this convolution is obtained using the assumed expansion-source field Eq.(12), and is:

$$u_e(x,t) = -\sum_{i=1}^{N} \left(-\frac{1}{\rho}\frac{d\rho}{dt}\right)_i (t)\, A_i(t)\, \nabla G_\delta(x-\chi_i(t)) , \qquad (14)$$

where
$$\nabla G_\delta(x) = \nabla \overline{G}(x)\, F(\frac{r}{\delta}) \quad \text{and} \quad \nabla \overline{G}(x) = -\frac{(x,y)}{2\pi r^2} .$$

The velocity induced by the boundary conditions is obtained from Eq.(7) using Schwartz–Christoffel conformal mapping and the method of images (Section IV).

The β S-Z scalar solution is obtained from the corresponding gradient field by recognizing the scalar and gradient can also be related via a Poisson equation, $\nabla^2\beta = \nabla\cdot g$.

The Green's function solution of this equation is further manipulated by performing a by-parts integration, using the divergence theorem and recognizing that the gradient field decays at infinity (unbounded domain): $\beta(x) = \int \nabla\overline{G}(x-x')\cdot g(x')\, dx'$. Using the gradient field of Eq.(12) a discrete desingularized form is obtained:

$$\beta(x,t) = \sum_{i=1}^{N} g_i(t)\, A_i(t) \cdot \nabla G_\delta(x-\chi_i(t)) + \beta_b . \qquad (15)$$

β_b here is the integration related function. It is determined using a Shwartz-Christoffel conformal mapping while satisfying the boundary condition using images.

Integration of the transport equations: The time evolution of the flow and scalar fields is established by numerically integrating the transport equations locally for each element. For this purpose, the integration takes place in two fractional steps [14], the first deals with all processes other than diffusion, while the second concentrates on the latter.

During the first step the element location is updated by numerically integrating

$$\frac{d\chi_i}{dt} = u(\chi_i,t) , \qquad (16)$$

7

using a predictor-corrector scheme. This defines element trajectories and material lines.

The element vorticity is updated by integrating the circulation equation:

$$\frac{d\Gamma_i(t)}{dt} = -\frac{[\nabla\rho]_i(t)}{\rho(\chi_i,t)} \times \frac{d\mathbf{u}(\chi_i,t)}{dt} A_i(t) \ , \tag{17}$$

were the pressure gradient has been replaced by the material acceleration using the momentum equation. The integration is accomplished using a predictor-corrector scheme in which the material acceleration is established via a two-step iteration, forward-difference algorithm. Equation (17) is obtained using kinematics[7].

Using kinematics to simplify the transport is also followed in the integration of the β-gradient transport equation. The first fractional step in the integration of this equation describes pure convection. Recognizing that in such a case isoscalar and material lines coincide and considering the kinematical evolution of the latter in conjunction with continuity we can rewrite the governing transport equation[8] (left hand side of Eq.(15)) as

$$\frac{d}{dt}\left[\frac{g_i(t)}{\rho(\chi_i,t)\ dl_i(t)}\right] = 0 \ , \tag{18}$$

with $\mathbf{g_i} = g_i\hat{\mathbf{n}}_i$ and $dl_i = |\mathbf{dl_i}|$, where $\hat{\mathbf{n}}_i$ is the unit vector normal to the material line and $\mathbf{dl_i}$ is a material line elemental segment. Equation (18) implies that $\dfrac{g_i(t)}{\rho(\chi_i,t)\ dl_i(t)} = \text{constant}$ along a material-isoscalar line. The constant is specified by the initial conditions, and $\mathbf{dl_i}$ as well as $\hat{\mathbf{n}}_i$ are readily available due to the Lagrangian nature of the scheme.

When the reaction rate occurs at infinite rate, integration of Eqs.(16-18) completes the first fractional integration step. For the general, finite reaction rate case, however, the integration of the product mass-fraction transport equation is also carried out. In this case, the concept of product particles is introduced. These particles are located at the element

---

[7] Material line kinematics expressed in the form $\dfrac{d(d\mathbf{l})}{dt} = \mathbf{dl} \cdot \nabla\mathbf{u}$, $\mathbf{dl}$ being a material line elemental segment, combined with continuity equation yields $\nabla\cdot\mathbf{u} = \dfrac{1}{dA}\dfrac{d(dA)}{dt}$ where $dA = dl\ dn$ is an elemental fluid element area with dl and dn being the element's dimensions along and normal to the material line, respectively. Substitutiing this expression into the vorticity equation and assuming that the vorticity is constant over the area of the fluid element yields: $\dfrac{d\omega}{dt} + (\nabla\cdot\mathbf{u})\ \omega = \dfrac{1}{dA}\left(dA\dfrac{d\omega}{dt} + \dfrac{d(dA)}{dt}\ \omega\right) = \dfrac{d(\omega\ dA)}{dt} = \dfrac{d\Gamma}{dt}$

[8] For derivation see Ref.[4]

centers and directly experience the reaction process. The need to use these particles stems from the fact that the nonlinearity of the reaction requires the use of precise values for the properties involved in the reaction rate. As already seen, the strengths of the elements are crude approximations of the values of the field properties at the same location. Implementing reaction on the element strength will yield erroneous, even non-physical results. In addition, depending on the diffusion algorithm to be used, the strengths may not experience the diffusion process (e.g. in the traditional expanding core [13], the random walk [1] or the diffusion velocity [15] schemes). Since only material which mixes molecularly can burn, the use of the strengths for reaction will unavoidably lead to errors[9].

This last point is important in the implementation of diffusion. Problems related to the traditional core expansion scheme are associated with the *transport* of expanded cores during convective [16]. The implementation of diffusion, on the other hand, is exact. With product particles, the expanded cores are not convected. As will be seen, the cores expand during the diffusion step, the new particle values are established, the particles are convected, and then the new interpolation function is created using the original size cores. The net result of this is that the long term effect of diffusion is to change the strengths of the elements rather than the cores. In this respect the version of the core expanding scheme presented here bears similarities to the particle exchange scheme of diffusion [17][10].

The integration of the product mass-fraction equation, like that of the rest of the transport equations, is carried out in two fractional steps. In the first step we integrate:

$$\frac{dY_p(\chi_i,t)}{dt} = (1+\phi)\ \dot{w}(\chi_i,t)\ , \tag{19}$$

for each product particle via an Euler predictor-corrector scheme. This yields the product values prior to diffusion, denoted as $Y_p^{\#}(\chi_i,t)$. These values are used to rediscretize the product field and obtain the element product strengths as noted earlier, i.e.

$$\sum_{i=1}^{N} Y_{pi}(t)\ A_i(t)\ f_\delta(|x-\chi_i|) = Y_p^{\#}(\chi_i,t) \tag{20}$$

The solution of this system of equations is simplified by taking into account the nature of the core-function which implies that only the closest neighbors contribute to the strength of an element. Thus, in establishing the strength of a given element, only elements which are $r/\delta < \sqrt{12}$ (i.e. $\exp(-(r/\delta)^2) > 10^{-6}$) away from the element are considered. A function

---

[9] In this case, reaction will cease as soon as any originally premixed material (i.e. from initial or inlet conditions), burns.

[10] We are indebted to Dr. Georges-Henri Cottet for pointing this out during a recent discussion.

iteration is used in the solution of Eq.(20) which is greatly helped by the availability of good initial guesses, offered by the values of the strengths at the previous time step.

To check the discretization error which by construction is small, and to minimize its effects, the product particle values are reconstructed from the obtained strengths yielding $Y_p^{\#\#}(\chi_i,t)$ with $\left| Y_p^{\#\#}(\chi_i,t) - Y_p^{\#}(\chi_i,t) \right|$ being the value of pointwise discretization error.

Subsequently, the diffusion step is performed via core expansion scheme

$$\delta_i^2(t+\Delta t) = \delta_i^2(t) + \frac{4\,\Delta t}{C} ,\tag{21}$$

where $C = Re$ for $\zeta = \omega$ and $C = Pe$ for $\zeta = g$ or Y_p, which is the analytical solution of the diffusion equation for each element. For the product mass-fraction, one more manipulation is executed to reduce the impact (if any) of the discretization error.

Clearly, the solution after the diffusion step, $Y_p^{\#\#D}(\chi_i,t)$, includes this error. By subtracting the discretization error from this solution, a new, corrected, solution is obtained

$$Y_p(\chi_i,t) = Y_p^{\#}(\chi_i,t) + \Delta Y_p^{\#\#D}(\chi_i,t)\tag{22}$$

where $\Delta Y_p^{\#\#D}(\chi_i,t) = Y_p^{\#\#D}(\chi_i,t) - Y_p^{\#\#}(\chi_i,t)$ which includes discretization error only in the change of the product particle field due to diffusion $\Delta Y_p^{\#\#D}(\chi_i,t)$. Since the physical problem definition specifies the diffusion to be small, this approach allows even significant discretization errors to be tolerated. In this work, however, this effect was not exploited and the average discretization error was kept smaller than 1%. The reason is while the discretization error is subtracted from the product particle solution ($Y_p(\chi_i,t)$) it is not removed from the product field solution ($Y_p(x,t)$) since it is still included in the product strengths. Thus, while the error is not fed back into the Lagrangian calculations (i.e. the integration of the product equation) it is present in any instantaneous product field.

The calculation of the density gradient necessary in the integration of the circulation equation implies knowledge of the product mass-fraction gradient field. In the infinite reaction rate case this is trivially established from the SZ gradients. For the finite reaction rate, it is established by differentiating the product mass-fraction field given by Eq.(18) as suggested by Anderson [18], i.e.

$$\nabla Y_p(x,t) = \sum_{i=1}^{N} Y_{pi}(t)\, A_i(t)\, \nabla f_\delta(x-\chi_i) .\tag{23}$$

The severe stretching of the Lagrangian mesh used in the discretization of the transported quantities, which increases the distance between neighboring elements, may lead to the deterioration of the solution accuracy. To overcome this problem, a scheme of

10

local mesh refinement is adopted, based on local conservation principles, whereby elements are continuously introduced and deleted to ensure core overlap [18, 19].

IV. GEOMETRY AND BOUNDARY CONDITIONS

The computational domain and some boundary conditions are shown in Fig.1. The shear layer evolves in a two-dimensional channel of height H and length X_{max}, between two parallel streams (1 top, 2 bottom) which mix downstream of a thin splitter plate. Initially, both streams are at the same temperature and density, T_o ρ_o, and each carries a single reactant. The top and bottom walls are modeled as rigid, free slip, impermeable and adiabatic planes. At the downstream section, a condition of vanishing vorticity and scalar gradient is used as outflow boundary condition, and is applied by removing the elements which cross the exit boundary. The error introduced by this rather arbitrary exit boundary condition was investigated by performing simulations with increasingly longer domains and quantitatively comparing the solution in their common sections. An example from this study is shown in Fig.2 which presents results of simulations of the forced non-exothermic flow for $X_{max} = 7$, top, and $X_{max} = 5$ bottom. The shear layer is represented by plotting the transport elements and their local velocity vectors relative to the mean flow[11]. We found that the difference between the two solutions was negligible at about one channel width upstream from the exit of the shorter domain (left dashed line in Fig.2).

The inlet profiles required in the simulation, the vorticity and β-gradient, and, in the case of finite reaction rate, the product mass-fraction, are: $\omega(x=0,y,t) = -\dfrac{U_1 - U_2}{\sqrt{\pi} \ \sigma} Z(y)$,

$$\nabla \beta(x=0,y,t) = \frac{1}{\sqrt{\pi} \ \sigma} Z(y), \quad Y_p(x=0,y,t) = Y_{p_{max}} Z(y), \quad \text{where } Z(y) = \exp \left(-\frac{(y-0.5)^2}{\sigma^2} \right).$$

In these above expressions, the channel height is the non-dimensionalizing lengthscale, while U_1, T_o and ρ_o are the velocity, temperature and density scales, respectively. σ, the standard deviation of the Gaussian profiles, is defined by requiring that two wavelengths of the most unstable mode of the uniform density shear layer fit $Y_p(x=0,y,t) = Y_{p_{max}} Z(y)$, within the channel height ($\sigma = 0.04$). $Y_{p_{max}}$ is chosen as 0.4.

The boundary conditions are satisfied by using a Shwartz-Christoffel conformal transformation, which maps the entire channel region onto the upper half of a complex plane (Fig.3). In this mapping the two fluid streams appear as volume sources

---

[11] The physical and numerical parameters used in obtaining the results of Fig.2 not specified here are the same as those of the main body of the results of this paper which are given in the following sections.

11

symmetrically located with respect to the origin, and solutions to the Laplace equations governing $\mathbf{u_b}$ and β_b can be simply established by using mass conservation arguments. The mapping however, is also beneficial to the implementation of the image system for the transport elements which helps impose the boundary conditions.

Initialization of the calculation is carried out by assuming that the inlet conditions persist throughout the domain. Hence, within the support of the vorticity, β-gradient and product mass fraction, a square mesh of elements of side h=0.0195 are distributed along nine material layers. The value of the core radius is δ=0.0234. It is noted that the discretization of the initial profiles may essentially be accomplished by the five central layers. The two extra layers on either side of the central five are introduced to accommodate later rediscredizations (see previous section) which may yield significant values for the strengths of the elements on the extra layers as a result of diffusion. The number of extra layers to be added is specified by considering a diffusion length argument $L \approx \sqrt{t_{res}/\alpha}$ where $t_{res} = X_{max}/[0.5\,(U_1 + U_2)]$ is the average residence time of elements within the computational domain and α is the thermal (or any other) diffussivity.

External forcing is implemented at the inlet. The forcing signal consists of in-phase components of the most unstable mode of the uniform-density layer and its subharmonic, both at an amplitude $A_f=A_s=0.025$. This forcing leads to early roll-up and pairing of the uniform density layer [6]. Forcing is implemented by displacing elements at the inlet in the cross-stream direction according to the forcing signal.

V. RESULTS AND DISCUSSION

Simulations using a range of the governing physical parameters were obtained and used to analyze the flow and reacting field dynamics [20-22]. In another study the effect the inlet boundary condition was investigated [23]. In this paper we concentrate on the effect of the numerical parameters and we keep the physical parameters fixed.

We consider a shear layer with velocity ratio $r = \dfrac{U_2}{U_1} = 0.5$ and Reynolds (and Pecled) number $Re = \dfrac{U_1 H}{\nu} = 12800$, where ν is the kinematic viscosity, evolving in a channel of length $X_{max} = 5$. For the finite reaction rate cases the normalized activation temperature, frequency factor, enthalpy of reaction and mass stoichiometry ratio are $T_a = \dfrac{E_a}{RT_o} = 10$, $A_f = \dfrac{A_f H}{U_1} = 640$, $Q_o = \dfrac{\Delta h_f}{c_p T_o} = 6$ and $\phi = 1$ respectively. The Damkohler number, $Da = \dfrac{\tau_{dif}}{\tau_{che}}$, where $\tau_{dif} = \dfrac{H^2}{\alpha}$ is the diffusion time scale and $\tau_{che} = \dfrac{T_f}{A_f} \exp(\dfrac{T_a}{T_f})$ the

12

chemical reaction time scale, and the Karlovitz number, $Ka = \frac{\tau_{che}}{\tau_{flw}}$ where $\tau_{flw} = \frac{H}{U_1}$ is the flow time scale, are $Da \approx 168100$ and $Ka_d \approx 0.08$, respectively.

In the simulations the spatial resolution specified via h, δ, the number of layers and the parameters of the injection-combination scheme was kept invariant. The temporal resolution was increasingly refined to test the convergence of the solution in time. This was carried out for the more general, finite reaction rate case. The time steps considered were $\Delta t = 0.2, 0.1, 0.05, 0.025$. Figures 4 and 5 present results from this study. In both figures the $\Delta t = 0.025$ solution is used as the base-comparison case.

Figure 4 presents the average pointwise error (w.r.t the $\Delta t = 0.025$ solution) of the velocity, β S-Z variable and product mass fraction fields, i.e. the three variables related to the integration of the transport equations, for the three different time-step cases considered, i.e. $\Delta t = 0.2, 0.1$ and 0.05. In all cases only the $0 < x < 4$ section of the computational domain was considered as explained earlier. The solution used in the calculation of the error is obtained on a 9x51 mesh, as the average of fifty instantaneous solutions obtained at the same times for all numerical solutions. The figure clearly shows that the solution converges in time and that this convergence is approximately linear.

More detail is offered by Fig.5, where the profiles for the velocity (top), the β S-Z variable (middle) and the product mass fraction (bottom) of the solution obtained as described in the previous paragraph, are presented at the same streamwise location $x=2$. Pictures present the comparison of the $\Delta t = 0.2$ solutions, with the base, $\Delta t = 0.025$, solution. The figure confirms the result of the previous figure. We found that the $\Delta t = 0.1$ timestep yields solutions which essentially capture most of the features of the more temporally refined solution. As a result, in what follows, $\Delta t = 0.1$ simulations will be used in the further analysis of the flow.

Figure 6, displays two dimensional visualizations of the instantaneous vorticity ((a)-top) and temperature[12] ((b)-top) for the finite reaction rate flow. These are contrasted to corresponding visualizations of the infinite reaction rate flow (bottom of (a) and (b)).

Substantial similarity is observed between the finite and infinite reaction rate results. The finite reaction rate results suggest that the parameters chosen for the simulations are such that reacting field corresponds to fast (as compared to the flow) reaction, i.e. low Karlovitz number combustion. The infinite reaction rate model describes the extreme of this case, i.e. zero Karlovitz number combustion in which the flame is infinitely thin and

---

[12] Under the assumptions of the physical model used here the temperature fields are equivalent to those of the product mass fraction.

cannot be quenched. Thus, under the conditions assumed in the simulations the infinite reaction rate model offers a good approximation of the finite reaction rate flow.

In the context of this discussion the similarity of the finite and infinite reaction rate results is most important in that it offers further validation of the numerical methodology. From a numerical standpoint there are fundamental differences between the finite and infinite reaction rate numerical models (Section III). Most importantly are all parts related to the integration of the product mass fraction equation. This equation is absent in the infinite reaction rate model. Thus, by the simple fact of the similarity of the finite and infinite reaction results a qualitative validation is offered for the numerical integration of the product mass fraction equation, the success of the implementation of the concept of product particles, the new version of the core expansion scheme which includes the inversion of discretization-interpolation function, etc.

A more severe test is demonstrated in figure 7 where the instantaneous contribution of the baroclinic torque, $\dot{\omega}_B = \frac{du}{dt} \times \frac{\nabla \rho}{\rho}$ is plotted for both the finite (top) and infinite (bottom) reaction rate cases. The $0 < x < 3$ part of the domain is shown. As can be seen from the figure, the characteristics of the field contribution of the baroclinic term of the vorticity equation (Eq.(12)) are quite complicated. This should be expected as this quantity represents the rate of change of a gradient field. Satisfactory explanations for it, however, were proposed [20]. Our interest here is the similarity between the finite and infinite reaction rate results. The level of detail in the similarity of such a complicated field substantially increases the confidence in the obtained solution.

More specifically, the density gradient, required in the calculation of $\dot{\omega}_B$, is related to the product mass fraction gradient field via the equation of state and the γ S-Z variable. As was described in Section III the product mass fraction gradient field is obtained using different numerical formulas. The fact that the final result for $\dot{\omega}_B$ is similar even to the smallest scale, offers a good consistency check between the two approaches.

VI. CONCLUSIONS

The two-dimensional Lagrangian Transport Element Method, an extension of the Vortex Element Method able to resolve reacting scalar transport, has been presented and implemented in the simulation of the non-premixed shear layer flow. The method is able to resolve both the variable density flow and the associated exothermic reacting field.

Results indicate that the method is able to accurately reproduce the essential features of the flow. Convergence of the solution in time is presented and is found to be

14

approximately linear. It is shown that the finite reaction rate solutions obtained correspond to those at low Karlovitz number and bear significant similarity to those of the infinite reaction rate model. This similarity offers validation for the part of the numerical methodology related to the integration of the product mass-fraction equation since this part is not common to the finite and infinite reaction rate models of the reacting field. Examples of this are the utilization of product particles versus product elements for the reaction, the use of alternative formulas for calculating the product mass-fraction gradient and the introduction of a novel version of the core-expansion scheme which does not suffer from the problems associated with earlier versions.

REFERENCES
1. Chorin, A.J., "Numerical Study of Slightly Viscous Flow," *J. Fluid Mech.*, **57**, pp.785-796, 1973. 2. Ghoniem, A.F., Chorin, A.J. and Oppenheim, A.K., "Numerical Modelling of Turbulent Flow in a Combustion Tunnel," *Philosophical Transactions of the Royal Society of London*, **304**, 303-325 (1982).
3. Ghoniem, A.F. and Givi, P., "Lagrangian Simulation of a Reacting Mixing Layer at Low Heat Release," *AIAA Journal,* **26**, pp.690-697,1988 .
4. Krishnan, A. and Ghoniem, A.F., "Simulation of Rollup and Mixing in Rayleigh-Taylor Flow Using the Transport Element Method," *J. Comp. Phys.*, **99**, pp.1-27, 1992.
5. Knio, O.M. and Ghoniem, A.F., "The Three-Dimensional Structure of Periodic Vorticity Layers Under Non-Symmetric Conditions," *J. Fluid Mech.*, **243**, pp.353-392, 1992.
6. Soteriou, M.C. and Ghoniem, A.F., "Effects of the Free-stream Density Ratio on Free and Forced Spatially Developing Shear Layers," *Physics of Fluids*, **7** (**8**), pp.2036-2051, 1995.
7. Ghoniem, A.F., and Krishnan, A., "Origin and Manifestation of Flow-Combustion Interactions in a Premixed Shear Layer," *22nd Symposium (International) on Combustion*, The Combustion Institute, Pittsburgh PA, pp. 665-675, 1988.
8. Knio, O.M. and Ghoniem, A.F., "Vortex Simulation of a Three-Dimensional Reacting Shear Layer with Infinite-Rate Kinetics," *AIAA Journal*, **30 1**, pp.105-116, 1992.
9. Chua, K., Boschitsch, A.H., Koumoutsakos, P., Winckelmans, G. and Leonard, A.,"Numerical Simulation of Chemically-Reacting Shear-Layers via Three-Dimensional Fast Particle Methods," AIAA -94-0675 paper, 1994.
10. Corcos, G.M., and Sherman, F.S., "The Mixing Layer: Deterministic Models of a Turbulent Flow. Part 1. Introduction and the Two-Dimensional flow," *J. Fluid Mech.*, **139**, pp.29-65, 1984.
11. Lakkis, I., Soteriou, M. and Ghoniem, A.F., "Vortex Simulation of Non-reacting and Reacting Buoyant Plumes," to be submitted for publication.
12. Hald, O.H. and Del-Prete, V.M., "Convergence of Vortex Methods for Euler's Equations," *Math.Comp.*, **32**, pp.791-809, 1978.
13. Leonard, A., "Review: Vortex Methods for Flow Simulation," *Journal of Computational Physics*, **37**, 289-335,1980.
14. Beale, J.T. and Majda A., "Rates of Convergence for Viscous Splitting of the Navier-Stokes Equations," *Math. Comp.,* **37**, pp.243-259, 1981.
15. Kempka, S.N. and Strickland, J.H., "A Method to Simulate Viscous Diffusion of Vorticity by Convective Transport of Vortices at a Non-Solenoidal Velocity," Sandia Laboratory Report SAND93-1763, December 1993

16. Greengard, C., "The Core Spreading Vortex Method Approximates the Wrong Equation," *Journal of Computational Physics*, **61**, pp.345-348, 1985.
17. Degond, P. and Mas-Gallic, S., "The Weighted Particle Method for Convection-Diffusion Equations. Part 1: The Case of Isotropic Viscosity," *Mathematics of Computation*, **53 188**, pp.485-507, 1989.
18. Anderson, C.R., "A Vortex Method for Flows With Slight Density Variations," *J. Comp. Phys.*, **61**, pp.417-444, 1985.
19. Ghoniem, A.F., Heidarinejad, G. and Krishnan, A., "Numerical Simulation of a Thermally Stratified Shear Layer Using the Vortex Element Method," *J. Comp. Phys.*, **79**, pp.135-166, 1988.
20. Soteriou, M.C. and Ghoniem, A.F., "The Vorticity Dynamics of an Exothermic Spatially Developing, Forced, Reacting Shear Layer," *25th Symposium (International) on Combustion*, The Combustion Institute, pp.1265-1272, 1994.
21. Soteriou, M.C. and **Ghoniem**, A.F. "Dynamics of Reacting Shear Flows; Effects of Exothermicity and Forcing," AIAA-94-0777 paper, 1994.
22. Soteriou, M.C. and **Ghoniem**, A.F., "On the Application of the Infinite Reaction Rate Model in the Simulation of the Dynamics of Exothermic Mixing Layers," *Comb. Sci. and Tech.*, **105**, pp.377-397, 1995.
23. Soteriou, M.C. and **Ghoniem**, A.F., "The Effect of the Inlet Boundary Condition on the Mixing and Burning in an Exothermic Shear Flow," AIAA-95-0807 paper, 1995.
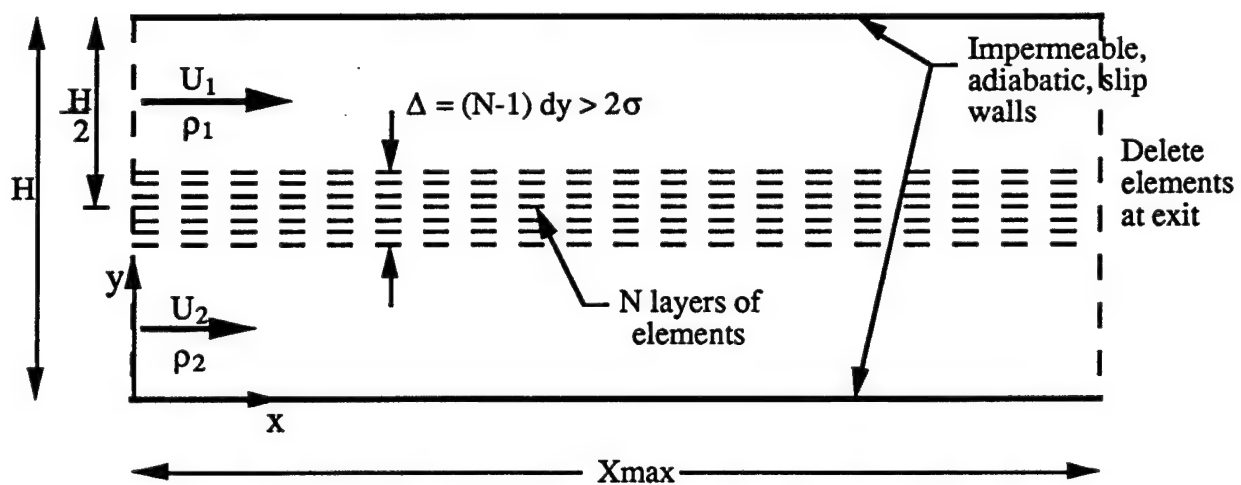
Figure 1   The geometry of the computational domain together with the initial element configuration and some of the boundary conditions .
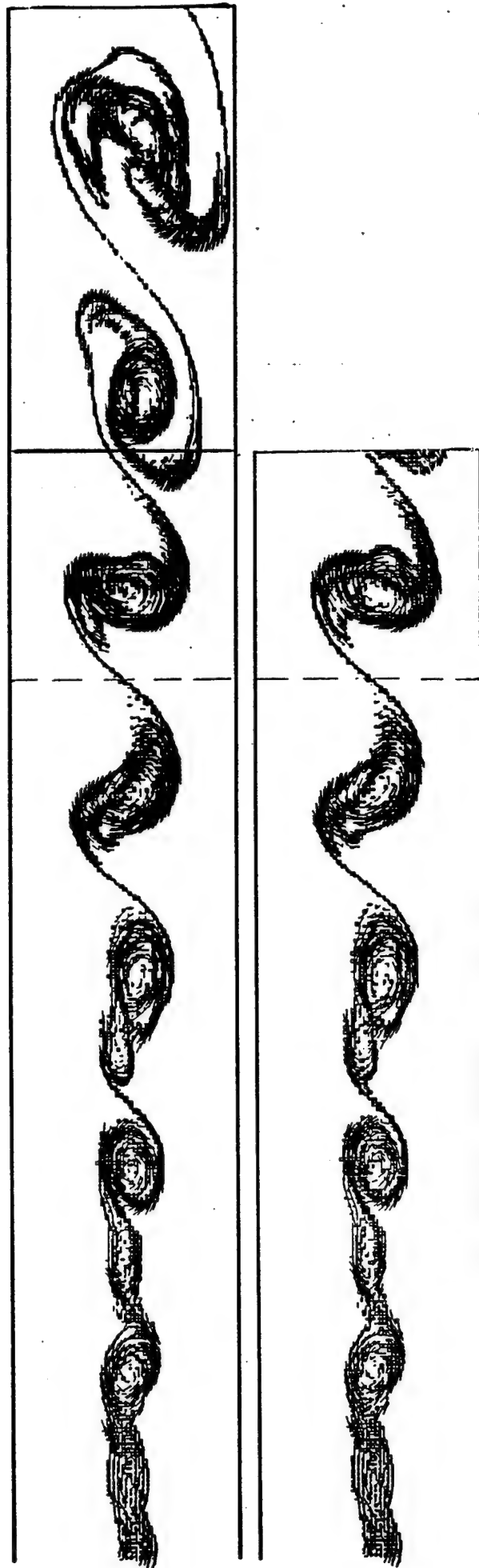
17

Figure 2   Assessment of the effect of the exit boundary condition by considering increasingly longer computational domains. The shear layer is depicted by plotting the transport elements and their local velocity vectors relative to the average flow. In both simulations the flow is forced, non-exothermic and at $t = 10$. The length of the domain is $X_{max} = 7$ for the top, and $X_{max} = 5$. for the bottom. The dashed lines are at $x = 4$.
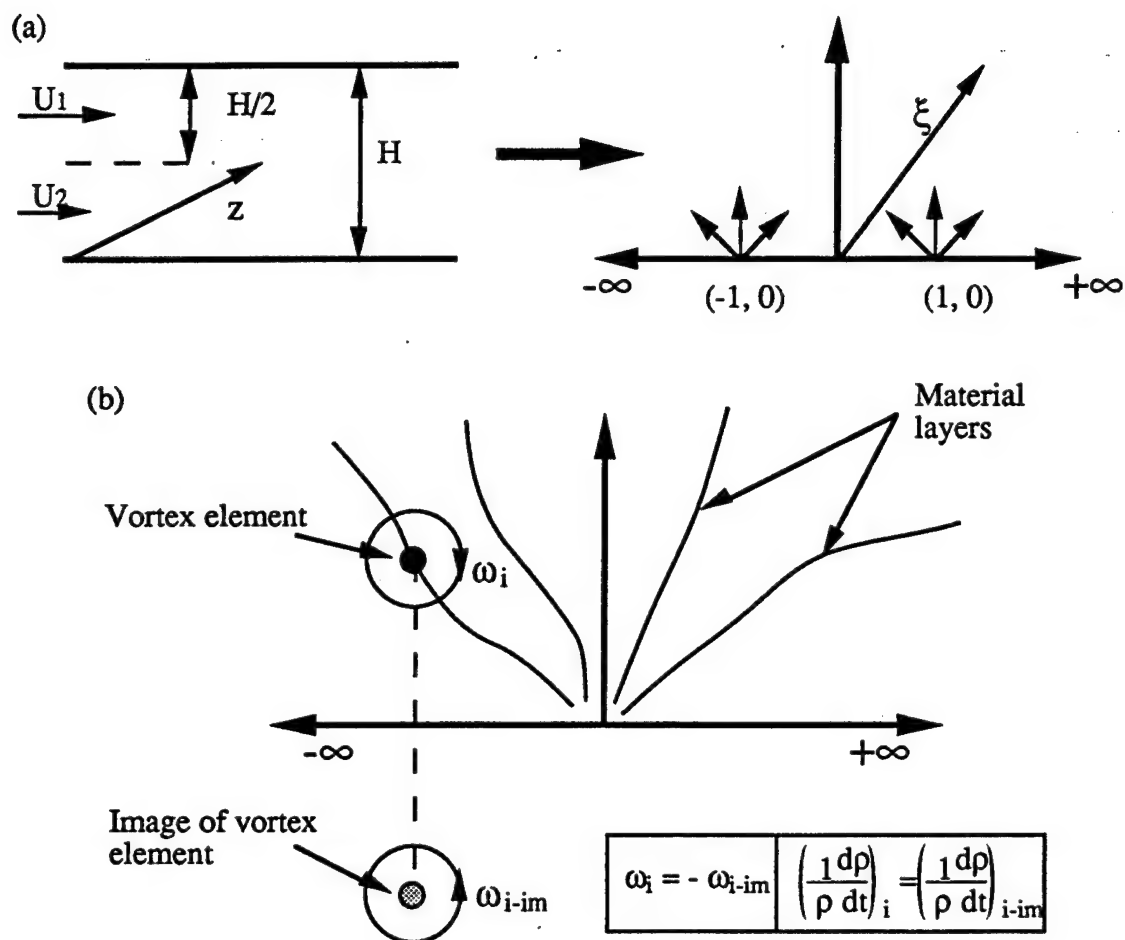
Figure 3. Illustration of the basic features of the Schwarz-Christoffel conformal mapping.
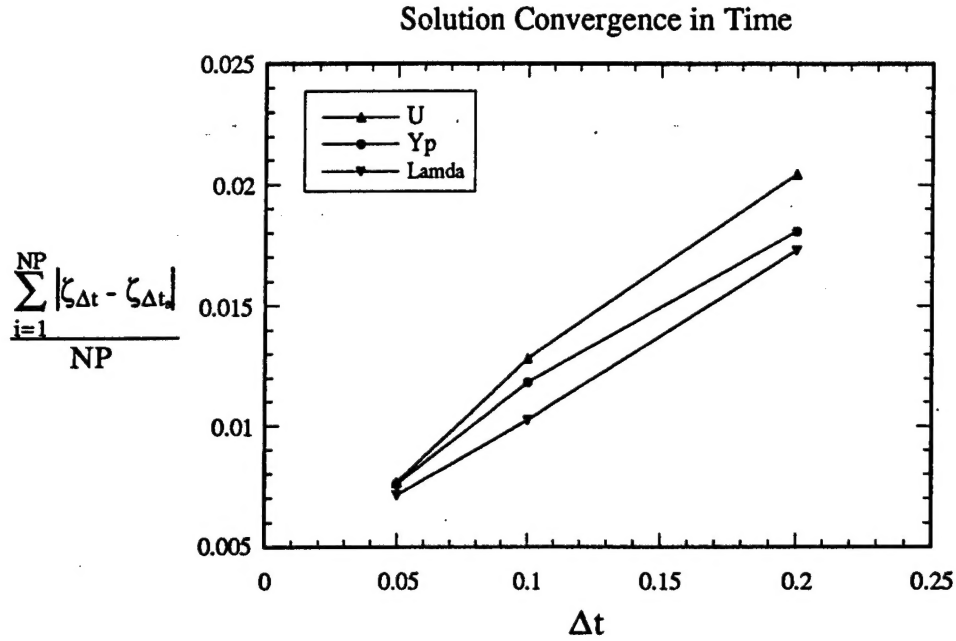
Figure 4. Temporal convergence of solution for the forced, finite reaction rate case with $X_{max} = 5$. Convergence checked by comparing solution with the base $\Delta t_s = 0.025$ case. The streamwise velocity, β (or λ) S-Z variable and product mass fraction field distributions are investigated, i.e. $\zeta = u, \beta, Y_p$. Each solution is established as the average of 50 instantaneous solutions obtained at the same times for all cases, over a 9x51 rectangular mesh, i.e. NP = 459, covering the $0 < x < 4$, $0 < y < 1$ section of the computational domain.
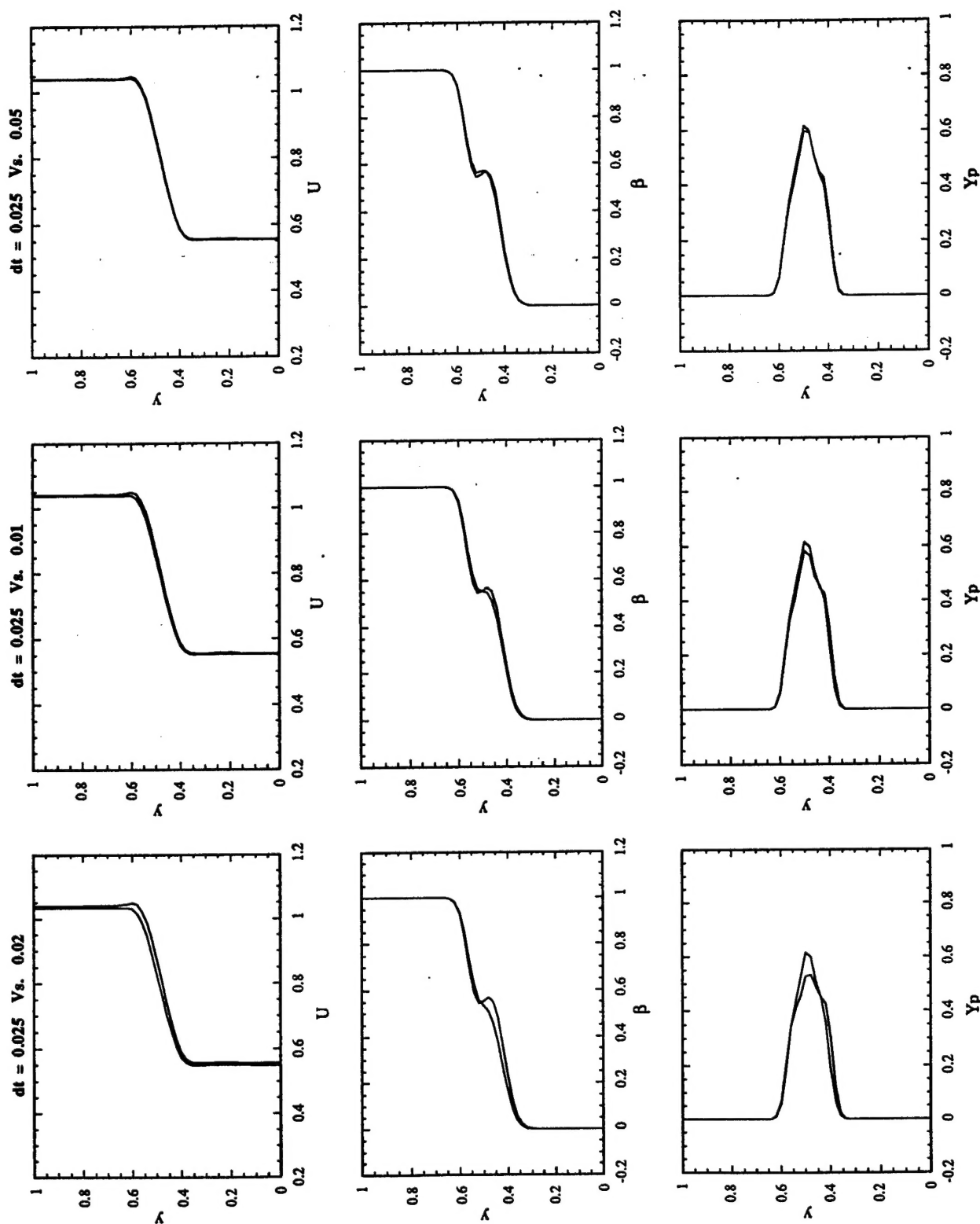
20

Figure 5. The profiles at x=2 of the velocity (top), β Shvab-Zeldovich variable (middle) and product mass-fraction (bottom) for field solutions obtained in the manner described in Fig.4. The timestep of the solutions decreases from 0.2 to 0.1 to 0.05 from left to right. In each picture the profile is plotted against that of the base $\Delta t = 0.025$ solution.

21

(a)

Comparison of the vorticity fields of forced, variable density shear layers with finite (top) and infinite (bottom) reaction rate. Domain shown is $0 < x < 5$ and $t=10$.
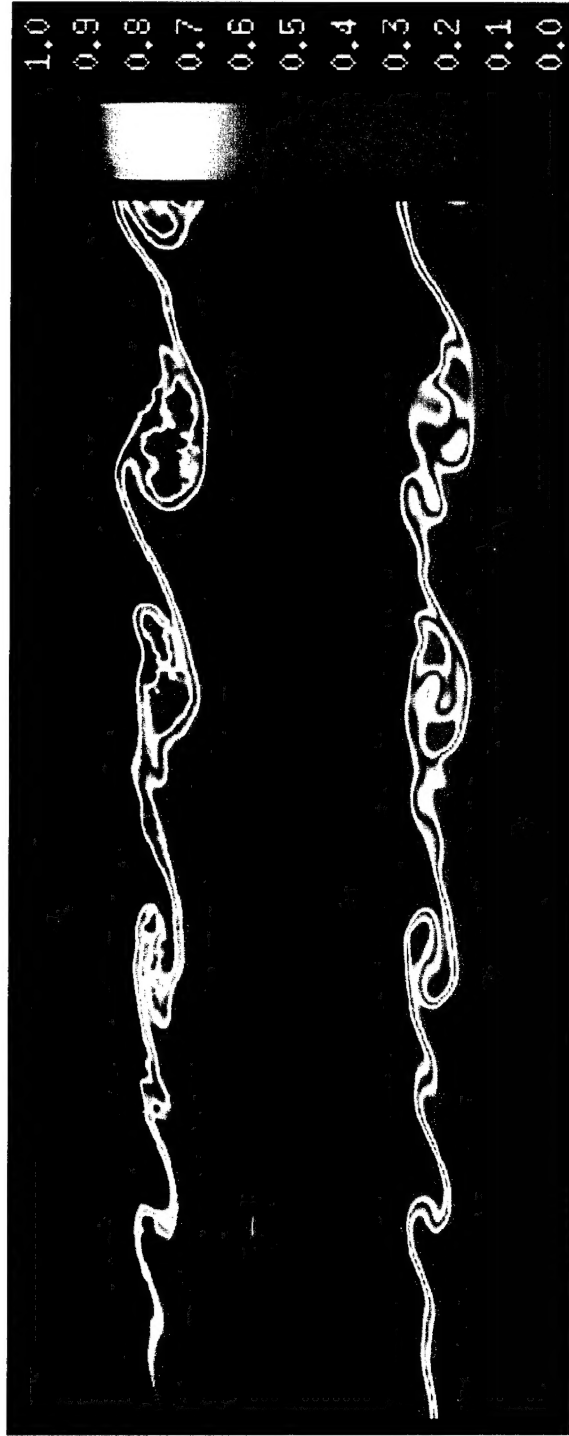
(b)

The product mass-fraction (or temperature) fields corresponding to the vorticity fields above.
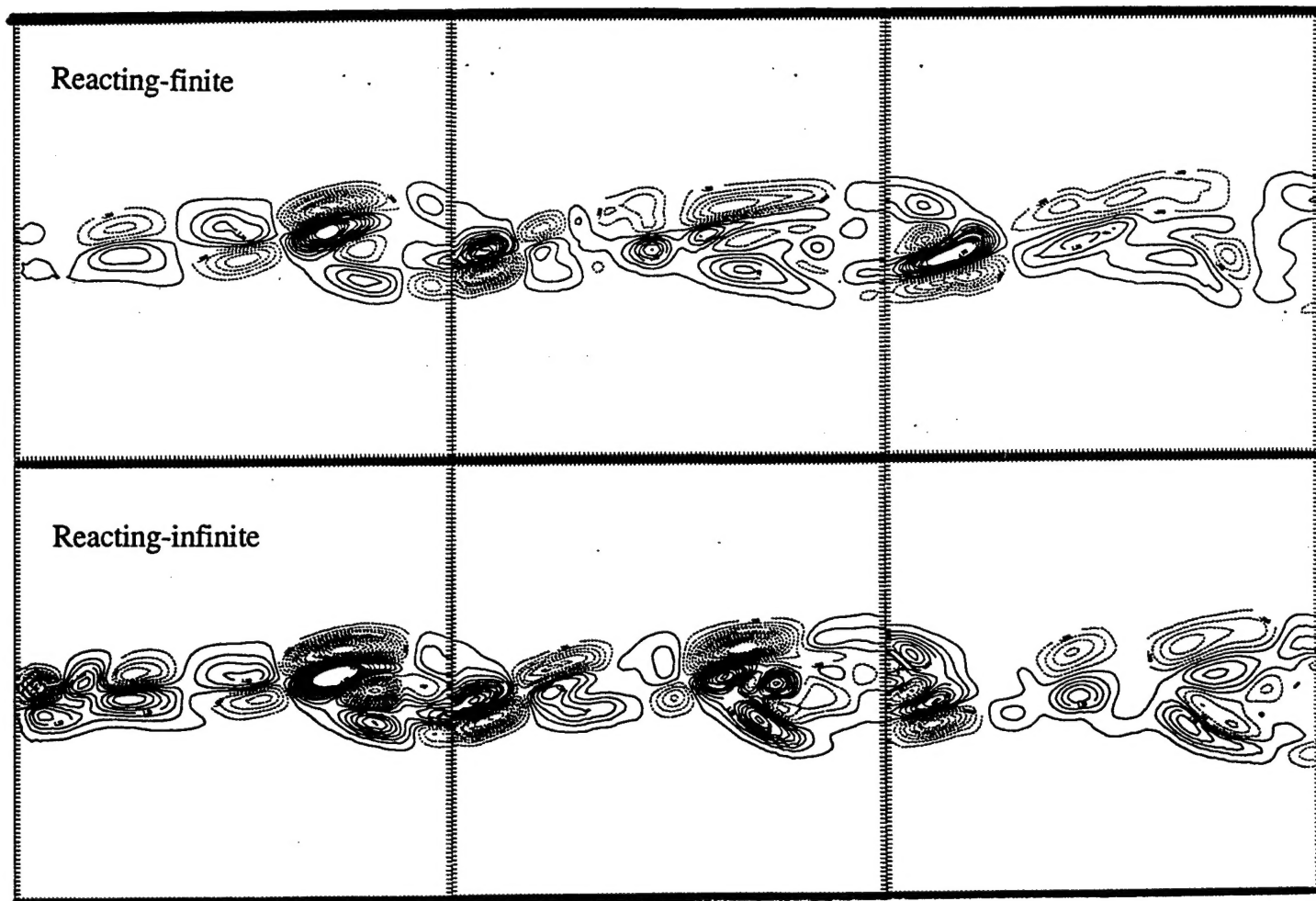
Figure 6

Figure 7. The baroclinic vorticity generation rate of the reacting at finite (top) and infinite (bottom) reaction rate shear layers at time t = 10. The 0 < x < 3 part of the computational domain is shown. Solid/dashed contours indicate negative/positive vorticity at an increment of 0.4.